

Dissertation zur Erlangung des Doktorgrades
der Fakultät für Chemie und Pharmazie
der Ludwig-Maximilians-Universität München

**High-Temperature Superconductivity
in Doped BaFe₂As₂**

Marianne Martin geb. Rotter

aus

Fort Sill (USA)

2010

Erklärung:

Diese Dissertation wurde im Sinne von § 13 Abs. 3 bzw. 4 der Promotionsordnung vom 29. Januar 1998 von Herrn Prof. Dr. D. Johrendt betreut.

Ehrenwörtliche Versicherung:

Diese Dissertation wurde selbständig, ohne unerlaubte Hilfe erarbeitet.

München, am 10. Dezember 2010

Marianne Martin

Dissertation eingereicht am 10. Dezember 2010

1. Gutachter: Prof. Dr. D. Johrendt

2. Gutachter: Prof. Dr. B. Lotsch

Mündliche Prüfung am: 26.01.2011

Acknowledgements

First and foremost, I am especially grateful to Prof. Dr. D. Johrendt, who offered me this very interesting and promising research project and gave me the opportunity to work in his extraordinary working group. Furthermore, I would like to express my gratefulness for his confidence and his continuous support paired with stimulating enthusiasm, which helped this work become what it is.

I am indebted to Prof. Dr. B. Lotsch for being available as co-referee of this thesis.

I am thankful to PD Dr. H.-C. Böttcher, Prof. Dr. K. Karaghiosoff, PD Dr. O. Oeckler and Prof. Dr. C. Scheu for being available as examiners in my *vivavoce*.

For carrying out a countless number of measurements, even on Sundays or holidays if time was pressing, and also for the following data process and fruitful discussions, I would especially like to thank Dr. D. Bichler, Dr. J. Deisenhofer, A. Günther, Dr. W. Hermes, C. Löhnert, A. Loidl, F. A. Martin, Dr. P. Mayer, T. Miller, C. Minke, PD Dr. O. Oeckler, Prof. Dr. R. Pöttgen, Dr. F. M. Schappacher, I. Schellenberg, F. Schrettle, M. Tegel, Dr. Y. Su and V. Zinth.

In detail, I would like to thank

- my bachelor and research students F. Corral Bautista, K. Förg, C. Hieke, M. Pangerl and T. Wirth for their great work and their enthusiasm,
- T. Miller for lots of interesting conversations and also for his support concerning technical problems with powder diffractometers,
- our daily “Kreuzwortsrätselrunde” as well as the weekly “Kochgruppe“ for loads of fun during lunch time,
- W. Wunschheim for his technical support whenever hard or software, printer or something else suddenly quit the service,

- C. Minke for several hours of measuring EDX, even if the supposedly nice crystals turned out to be only “Bräsal”,
- C. Löhnert for her continuous support and great helpfulness in many respects,
- C. Höller (“da simma dabei”) for his friendship and his unshakeable cheerfulness, always ready for a spontaneous caravan and an exhilarating cup of coffee and last but not least for our collaboration in the entertainment committee,
- my colleague and friend C. Hecht, for green tea parties, nocturnal beer sessions, (japanese) culinary highlights and her support in all walks of life,
- my dear lab and office mates R. Frankovsky and M. Tegel simply for everything (including “I hope you like pain”, Elleberger, Rumba, Singstar-parties, “Frülein”, FSK 25 and so on). I hope we will never lose contact and meet for many funny activities again....,
- V. Zinth for her enthusiasm in building our great handicrafts and several interesting and funny gatherings
- F. A. Martin and V. Zinth for proof-reading this thesis and last but not least
- my whole (ex-) working group Dr. D. Bichler, R. Frankovsky, G. Friederichs, K. Förg, F. Hummel, Dr. S. Jakob, Dr. P. Jakubcová, C. Löhnert, Dr. H. Müller, E. Wiesenmayer and V. Zinth for a very amicable and constructive cooperation and loads of fun also with “The Finger”.

Thank you a lot!

For providing a perfect working atmosphere during the last years and for every scientific, technical and also personal support I would like express my thankfulness to all present and past colleagues of the working groups Schnick, Müller-Buschbaum, Oeckler, Lotsch and Schmedt a. d. Günne.

Above all, I am deeply indebted to my family and to my partner Franz who never stopped encouraging and believing in me and supported me with all their patience and love at all levels, in every way. Thanks a million!

*Science is wonderfully equipped to answer the question “How?”
but it gets terribly confused when you ask the question “Why?”*

(Erwin Chargaff)

Contents

1	Introduction.....	1
2	Preparative Methods	5
2.1	Starting Materials	5
2.2	Vacuum and Inert Gas Line	5
2.3	Synthesis of polycrystalline samples	6
2.4	Single crystal growth	7
2.4.1	Sn-Flux	7
2.4.2	Self flux method	7
3	Analytical Methods.....	9
3.1	X-Ray Diffraction Methods	9
3.1.1	Powder Diffractometric Methods	9
3.1.2	Single Crystal X-Ray Diffraction.....	10
3.2	Spectroscopic Methods	11
3.2.1	Mössbauer Spectroscopy	11
3.2.2	Scanning Electron Microscopy (SEM) and Energy Dispersive X-Ray Analysis (EDX).....	11
3.2.3	Angle-Resolved Photoemission Spectroscopy (ARPES).....	12
3.3	Specific Heat Measurements.....	12
3.4	Magnetic Investigations	13
3.5	Electrical Resistivity Measurements.....	14
4	BaFe₂As₂	15
4.1	Motivation	15
4.2	Sample Preparation	18

4.3	Crystal Structure Investigations.....	18
4.4	Specific Heat Measurements	24
4.5	Electrical Resistance of BaFe ₂ As ₂	25
4.6	Magnetic Susceptibility	26
4.7	⁵⁷ Fe Mössbauer Spectroscopy.....	27
4.8	Magnetic Structure.....	29
4.9	Single Crystal Growth of BaFe ₂ As ₂	31
4.9.1	Synthesis.....	31
4.9.2	Crystal Structure Analysis.....	32
4.9.3	Crystal Structure Description	36
4.9.4	Alternative Methods	37
4.10	Discussion	39
5	Doping of BaFe₂As₂	41
5.1	Synthesis	42
5.2	Crystal Structure of (Ba _{0.6} K _{0.4})Fe ₂ As ₂	42
5.3	Electrical Resistance Measurements.....	46
5.4	Magnetic Investigations.....	47
6	(Ba_{1-x}K_x)Fe₂As₂ (x = 0 – 1)	49
6.1	Crystal Structures.....	50
6.2	Electrical Resistance Measurements.....	53
6.3	Discussion	55
7	Underdoped (Ba_{1-x}K_x)Fe₂As₂ (x = 0 – 0.3).....	57
7.1	Crystal Structures and Phase Transition	59
7.2	Electric Resistivity	63
7.3	Magnetic Susceptibility	64

7.4	Specific Heat	65
7.5	Mössbauer Spectroscopy.....	73
7.6	Summary	77
8	Isoelectronic Doping of BaFe₂As₂.....	79
8.1	(Ba _{1-x} Sr _x)Fe ₂ As ₂	80
8.1.1	Synthesis	80
8.1.2	Characterization.....	81
8.1.3	Electrical Resistance of (Ba _{0.5} Sr _{0.5})Fe ₂ As ₂	86
8.1.4	Properties of (Ba _{1-x} Sr _x)Fe ₂ As ₂ ($x = 0 - 1$).....	87
8.2	BaFe(As _{1-x} P _x) ₂	89
8.2.1	Synthesis	89
8.2.2	Crystal Structures.....	91
8.2.3	Electrical Resistance Measurements	96
8.3	Conclusion	99
8.4	Structural Subtleties	101
8.4.1	Single Crystal Investigations of BaFe ₂ (As _{1-x} P _x) ₂	101
8.4.2	Crystal Structure Properties.....	101
8.4.3	Conclusion	106
9	ARPES Measurements	107
9.1	Theoretical Aspects.....	107
9.2	ARPES Experiment.....	110
10	Summary and Outlook	115
11	Appendix.....	123
12	Curriculum vitae.....	133
13	Bibliography	134

1 Introduction

During the last century, pioneering developments in the field of electrical engineering revolutionized nearly all aspects of our daily life. Today, in the age of technology, electronic components are getting more and more compact and increasingly powerful. In Shanghai, e.g., the world's fastest commercial train (Shanghai Transrapid) transports people with more than 400 km/h from the outskirts to the Airport of Shanghai and only recently the Chinese broke the world record in creating the world's fastest supercomputer (Tianhe-1A). This reflects clearly the actual technological trends that set new challenges to material science. In particular, replacing conventional metallic conductors by superconducting materials, and magnetic levitation enabled by superconducting magnets are topics of great interest in current research.

When current flows through conventional metallic conductors, current-dependent heat is generated and energy is lost. Therefore metallic conductors are the less applicable for technologies, the higher current strengths are required. Superconductors, however, conduct electricity without resistance below a critical temperature T_C . Because of their extraordinary properties, superconductors are already used in numerous electronical devices. Some examples for their applications are MRI (magnetic resonance imaging) magnets, chemical analytical tools such as NMR (nuclear magnetic resonance) spectroscopy or SQUID (Superconducting Quantum Interference Device) magnetometers, motors, ship propulsion, transformers, cryomagnets and offshore wind energy generators.

Mostly, critical temperatures of superconductors are below 30 K which makes cooling by the very expensive liquid helium inevitable. For commercial applications, however, superconductors with T_C 's higher than 77 K are desired, as these could be cooled by relatively cheap liquid nitrogen. Today, the only

class of superconductors that show sufficiently high critical temperatures are the cuprates. However, their processing to flexible materials such as wires or coils remains difficult due to their brittle, salt-like structure. Furthermore, the pronounced anisotropy of the superconducting properties causes problems. Therefore, technologists are still hoping for materials, which have high superconducting transition temperatures and show preferably isotropic behavior.

Since superconductivity was discovered in mercury in 1911 by Heike Kamerlingh Onnes, many other superconducting materials, in particular metals and alloys such as the A15 compounds (Nb_3Ge , $T_C = 23 \text{ K}$)^[1] were explored. A genuine breakthrough was achieved in superconductivity research when high-temperature superconductivity was discovered in the cuprates in 1986.^[2] These ceramic superconductors show critical temperatures higher than 77 K, such as 93 K in $\text{YBa}_2\text{Cu}_3\text{O}_7$ ^[3] or 133 K in $\text{HgBa}_2\text{CaCu}_2\text{O}_{6+x}$ ^[4] which is the highest confirmed critical temperature at ambient pressure so far. As mentioned above, the ceramics are difficult in processing, thus currently most helium-cooled low-temperature superconductors like NbTi or Nb₃Sn are used for applications.

According to the BCS theory developed by the physicists J. Bardeen, L. N. Cooper and J. R. Schrieffer, superconductivity in metals arises from the coupling of conduction electrons into Cooper pairs, which is mediated by vibrations of the crystal lattice (phonons). In its original form, the BCS theory is limited to superconducting transition temperatures below $\approx 30 \text{ K}$. Indeed, no metallic compounds with critical temperatures higher than 30 K were known for a long time. In this context, the most important low-temperature superconductors are the metallic A15 compounds (Nb_3Ge , $T_C = 23 \text{ K}$)^[1] and the Chevrel phases (PbMo_6Se_8 , $T_C = 18 \text{ K}$).^[5] Another class of superconductors followed in 1994 when the rare-earth borocarbides ($\text{YPd}_2\text{B}_2\text{C}$, $T_C = 23 \text{ K}$)^[6] have been discovered. The highest critical temperature for metallic compounds, however, was detected at 39 K for MgB_2 , whose superconducting properties were discovered in 2001.^[7] 39 K is clearly above the limit of classical BCS superconductors, but in the

meantime, it is accepted that the formation of Cooper pairs in MgB_2 is also phonon-mediated and can be well explained by an expanded BCS theory.^[8]

Finally, in March 2008, the discovery of high- T_C superconductivity in the iron arsenide oxides^[9] has heralded a new era in superconductivity research. After the first report on $\text{LaFeAs}(\text{O}_{1-x}\text{F}_x)$ with a critical temperature T_C of 26 K, even higher transition temperatures up to 55 K in fluoride doped $\text{SmFeAs}(\text{O}_{1-x}\text{F}_x)$ followed quickly.^[10] These materials, which are based on two-dimensional iron arsenide layers separated by rare earth oxide layers, represent the second class of high- T_C superconductors after the discovery of the cuprates more than 20 years ago.^[2] This is especially surprising, since historically the antagonistic relationship between superconductivity and magnetism has led researchers to avoid the use of magnetic elements, while these new superconductors contain high concentrations of the ferromagnetic metal iron. Therefore, few would have anticipated that an iron-containing material could show such an extraordinary T_C . In the meantime, the maximum T_C for the iron arsenides in general is 56.3 K ($\text{Gd}_{1-x}\text{Th}_x\text{FeAsO}$ with $x \approx 0.2$).^[11]

In the iron arsenide oxides, superconductivity emerges from two-dimensional FeAs layers similar to the cuprates with their two-dimensional copper oxide planes. The formation of Cooper pairs seems to be of an unconventional nature as in the cuprates, and superconductivity is also assumed to be mediated by magnetic fluctuations rather than by phonons. But there is an important difference between the iron arsenides and the cuprates: while there are no direct interactions between two copper atoms in the cuprates, the Fe 3d orbitals of the iron atoms in the iron arsenides overlap due to their short interatomic distances of about 285 pm which is approximately by only 10 % larger than in the pure Fe metal. Therefore, the iron arsenides are poor metals at room temperature, whereas the undoped cuprates are Mott insulators at ambient temperature.

The non superconducting parent compound LaFeAsO , which crystallizes tetragonal in the ZrCuSiAs -type structure^[12] undergoes a structural phase

Introduction

transition at about 150 K associated with a reduction of the lattice symmetry from tetragonal to orthorhombic. This leads to anomalies in electrical resistance, specific heat and the magnetic susceptibility and antiferromagnetic ordering is observed below $T_N = 134$ K. This structural and magnetic phase transition is suppressed by electron doping with fluoride or oxygen deficiency, as well as by hole doping with strontium, and the tetragonal phase becomes superconducting at critical temperatures between 25 K and 41 K.^[9,13,14]

Another well-known structure type which shows very similar structural conditions is the ThCr_2Si_2 -type structure that comprises about 600 compounds.^[15] One representative of this structure type is BaFe_2As_2 ^[16] which also crystallizes in a tetragonal structure (space group $I4/mmm$) and is built up by layers of edge-sharing $\text{FeAs}_{4/4}$ tetrahedra simply alternating with barium atoms instead of LaO sheets in contrast to LaFeAsO . The synthesis of BaFe_2As_2 was already reported in 1980 but except for the crystal structure and some indeterminate magnetic data,^[17] no physical properties were known.

In the scope of this thesis the physical properties of BaFe_2As_2 are intensively investigated and, based on a comparison with the properties of LaFeAsO , examined in terms of its suitability as a parent compound of a new structural family of the new high- T_C compounds. Further, different approaches of doping are presented and the effect of doping on its crystal structure and its physical properties is studied. Last but not least, this thesis provides a brief insight into theoretical aspects concerning high-temperature superconductivity discussed currently and finally presents a short summary and future prospects.

2 Preparative Methods

2.1 Starting Materials

The sources of supply as well as the purity of the commercially available chemicals used in this work are listed in Table 2.1.

Table 2.1: Source of supply and purity of the chemicals used in this work.

Name	Formula	Supplier	Purity [%]
Arsenic	As	Alfa Aesar	99.999
Barium	Ba	Sigma-Aldrich	99.99
Iron	Fe	Chempur	99.9
Phosphorus	P	Chempur	99.999
Potassium	K	Sigma-Aldrich	99.95
Strontium	Sr	Sigma-Aldrich	99.99
Tin	Sn	Alfa Aesar	99.99

2.2 Vacuum and Inert Gas Line

As some of the used elements and also some reaction products are sensitive to air and moisture, all manipulations and reactions have been carried out under an inert atmosphere of dry argon (purity grade 4.8, Messer). For storage and handling of the samples a glove-box (MB150-GI, O₂ < 1 ppm, H₂O < 1 ppm, MBraun) was used. For reactions, the reaction vessels were connected to a vacuum line and dried under vacuum using a heat gun. Evacuation was achieved by using a rotary vane pump (RZ5, suction capacity 5.6 m³ / h, Vacuubrand).

Purification and drying of inert gas was carried out by successively passing argon through columns filled with BTS-catalyst (copper dispersed on a ceramic carrier matrix, Fluka) maintained at a temperature of 393 K, molecular sieve (porewidth 0.4 nm, Merck), and phosphorus pentoxide (Merck).

2.3 Synthesis of polycrystalline samples

Polycrystalline samples of the solid solutions and the undoped 122 compounds were synthesized by heating mixtures of the elements, stoichiometric or with an excess of 5 % of alkaline or alkaline-earth metal, respectively. Therefore, the elements were weighed into alumina crucibles, which were placed in pre-dried silica ampoules (HSQ300, length \approx 50 cm, \varnothing_{ext} = 14 mm, wall thickness 1.2 mm, Vogelsberger Quarzglasstechnik) and afterwards sealed under argon atmosphere using an oxyhydrogen burner. In case of the barium-potassium solid solution the gas volume was reduced by alumina inlays in the crucibles to minimize the loss of potassium by evaporation. For the synthesis of the binary arsenide FeAs, the silica tubes were filled directly with the reaction mixture of stoichiometric amounts of iron and arsenic powders without using crucibles. Then the reaction mixtures were placed into tubular furnaces with electric resistance heating equipped with programmable controllers (Eurotherm). The temperature was measured by Pt/PtRh thermocouples. To avoid burst of silica ampoules due to possible exothermal reactions a heating rate of 50 K/h has been chosen. The reaction temperatures ranged from 873 K to 1173 K. After cooling, the samples have been homogenized and annealed at temperatures between 973 K and 1323 K several times. All products were black metallic powders which are stable in air for weeks except of KFe_2As_2 and mixed crystals of $(\text{Ba}_{1-x}\text{Sr}_x)\text{Fe}_2\text{As}_2$, which were therefore handled under argon atmosphere.

2.4 Single crystal growth

2.4.1 Sn-Flux

For the single crystal synthesis in a Sn melt distilled barium metal, iron powder, and sublimed arsenic at a ratio of 1.05 : 2 : 2 were mixed with four times the amount of tin granules. The element mixture was transferred into an alumina crucible and sealed in a silica tube under an atmosphere of purified argon. Then the sample was heated to 573 K at a rate of 100 K/h and afterwards the temperature was elevated to 873 K at a rate of 20 K/h. It was kept at this temperature for three hours and heated again to 1123 K at a rate of 50 K/h. After keeping the sample at this temperature for another 36 h it was cooled down to room temperature by shutting down the furnace. Subsequently the alumina crucible was wrecked and the metal ingot put into half concentrated hydrochloric acid to remove the tin flux from the silver shiny plate like crystals.

2.4.2 Self flux method

Single crystals of BaFe_2As_2 grown by the self flux method have been synthesized by heating distilled barium metal and the binary arsenide FeAs in a molar ratio of 1 : 4 in an alumina crucible. The sample was heated to 1323 K with a heating rate of 50 K/h. This temperature was held for two hours and afterwards cooled down to 1023 K with a rate of 6 K/h before the furnace was turned off. After wrecking the alumina crucible, the metal ingot was carefully crushed using an agate mortar and so excess FeAs removed from the crystals.

3 Analytical Methods

3.1 X-Ray Diffraction Methods

3.1.1 Powder Diffractometric Methods

For X-ray photographic investigations a STOE Stadi P diffractometer (STOE & Cie, Darmstadt, Germany) in focusing geometry using Ge(111)-monochromated Mo-K_{α1} radiation ($\lambda = 71.073$ pm) and a Huber G670 Guinier imaging plate (Cu-K_{α1} radiation ($\lambda = 154.051$ pm), Ge(111) monochromator) were available. The former one is operable in transmission as well as in Debye-Scherrer (capillary) geometry. Temperature dependent X-ray powder diffraction data between 300 K and 10 K were collected using the Huber G670 diffractometer equipped with a closed-cycle He-cryostat (Cold Head, CTI CRYOGENICS, Model 22 CP). Temperature measurement and control was performed by a temperature controller (LAKESHORE, Model 331) with a silicon diode temperature sensor. For identification and phase purity check of the synthesized samples the program package WINXPOW^[18] was used. Huber data were pre-processed with the program HConvert.^[19] Theoretical powder diffraction patterns were simulated by means of THEO^[20] included in the program package WINXPOW. Further, the integrated search routine “search-match”, which referred to the JCPDS-database,^[21] was used for phase analysis. The crystal structures were refined by the Rietveld method using first the GSAS^[22] software package using Thompson-Cox-Hastings functions with asymmetry corrections as reflection profiles^[22] and later the TOPAS package^[23] using the fundamental parameters approach as reflection profiles. Due to a better description of small peak half width and shape anisotropy, a modified approach of *Le Bail* and *Jouanneaux*^[24] was implemented in the TOPAS^[24] program. For details about the implementation, see literature.^[19] Giving consideration to possible texture effects,

the March-Dollase function was used for description of a preferred orientation of the crystallites. All diffractograms were plotted using the program package ORIGIN.^[25]

3.1.2 Single Crystal X-Ray Diffraction

For single crystal determination, small single crystals were selected utilizing a stereo microscope and fixed on thin glass fibers with some superglue. The quality of the crystals was checked by Laue photographs using a Buerger precession camera on Laue mode (Buerger Precession Camera 205, Huber) operating with white Mo radiation (Röntgengenerator Kristalloflex 760, Siemens). The Laue diagrams were recorded by imaging plates,^[26] for the readout a laser scanner (BAS 2500 Bio Imaging Analyser, Fuji Photo Film Corporation) was employed. The programs BASREADER^[27] and TINA^[28] were used for evaluating the diagrams.

Single crystal data were measured on an IPDS single-crystal X-ray diffractometer equipped with an area detector (STOE & Cie GmbH) or an Oxford Xcalibur3 four-circle κ -diffractometer equipped with a CCD detector, respectively. Both diffractometers act with graphite-monochromized Mo- K_{α} radiation ($\lambda = 71.073$ pm). Data reduction and absorption correction were performed with the programs X-PREP,^[29] X-RED^[30] and X-SHAPE.^[31] Crystal structures were solved by direct methods^[32,33] applying the program SHELXS-97^[34] and refined on F^2 by applying full-matrix least square method implemented in SHELXL-97.^[35,36] The visualization of crystal structures was accomplished by the program DIAMOND.^[37]

3.2 Spectroscopic Methods

3.2.1 Mössbauer Spectroscopy

For ^{57}Fe Mössbauer spectroscopy investigations, a $^{57}\text{Co/Rh}$ source was available. The powder samples were placed in thin-walled PVC container at a thickness between 4 and 10 mg Fe / cm². The measurements were run in the usual transmission geometry in the temperature range from room temperature to 4.2 K. The source was kept at room temperature.

3.2.2 Scanning Electron Microscopy (SEM) and Energy Dispersive X-Ray Analysis (EDX)

Scanning electron microscopy (SEM) was conducted on a JSM-6500F electron microscope (JEOL). The microscope was equipped with a model 7418 EDX detector (Oxford Instruments) allowing qualitative and semi-quantitative analysis of chemical compositions on the basis of characteristic X-Ray emissions of elements. Crystals were placed on a brass sample carrier fixed with self-adhesive carbon plates (Plano, Wetzlar, Germany). As the samples were already conductive, sputtering with carbon prior to use wasn't necessary. Data collection and evaluation was carried out with aid of the INCA^[38] program package.

3.2.3 Angle-Resolved Photoemission Spectroscopy (ARPES)

The ARPES experiments were carried out at the BESSY synchrotron radiation facility using the U125/1-PGM beamline and the “1³-ARPES” end station provided with a SCI-ENTA R4000 analyzer. Spectra were taken with various photon energies ranging between $h\nu = 30$ eV and 175 eV. The total energy resolution ranged from 10 meV (full width at half maximum (FWHM)) at photon energies $h\nu = 30$ eV to 20 meV at $h\nu = 175$ eV. The angular resolution was 0.2° along the slit of the analyzer and 0.3° perpendicular to it. For a detailed description of the experimental geometry please refer to the literature.^[39,40]

3.3 Specific Heat Measurements

Specific Heat measurements were carried out at the Universität Augsburg by the group of Dr. J. Deisenhofer and at the Institut für Anorganische und Analytische Chemie, Universität Münster by the group of Prof. Dr. R. Pöttgen. The heat capacity was measured for temperatures between 2 K and 300 K by a relaxation-time method in a physical properties measurement system (PPMS, Quantum Design, Inc.).

At constant pressure and external magnetic field the specific heat at low temperatures ($T \ll T_D$) of a solid is given by the Debye T^3 law:

$$C_p = \frac{12\pi^4 N_A k_B}{5T_D^3} \cdot T^3 = \beta T^3 \quad (3.1)$$

As the conduction electrons in metals give a contribution to the heat capacity as well, the Debye T^3 law has to be expanded by the electronic heat capacity:

$$C_p = \frac{\pi^2 N_A k_B^2}{2E_F} \cdot T + \frac{12\pi^4 N_A k_B}{5T_D^3} \cdot T^3 = \gamma T + \beta T^3 \quad (3.2)$$

The electronic contribution is linearly dependent on T . In a diagram where C_p/T is a function of T^2 the experimental values of C_p should show a linear dependence at very low temperatures. The value of the Sommerfeld coefficient γ can be deduced from the intersection of the straight line with the ordinate, whereas β is given by the gradient of the line.

3.4 Magnetic Investigations

Magnetic measurements of polycrystalline samples were either performed with a commercial SQUID magnetometer (MPMS-XL5, Quantum Design, Inc.) or a self-manufactured *ac* susceptometer.^[19]

The SQUID magnetometer operates in a temperature range from 1.8 K to 400 K with external fields up to 50 kOe. The fully automated differential dual-coil *ac* susceptometer operates in the temperature range from 3.4 K to 320 K with alternating magnetic fields up to 8 Oe and frequencies between 100 Hz and 10 kHz. For a detailed description of the *ac* susceptometer construction please refer to the literature.^[19] Sample masses of about 20 mg to 50 mg were loaded into gelatine capsules and fixed in a straw as sample holder. The output data files were processed directly in ORIGIN.^[25] Corrections for the sample holder and the core diamagnetism were applied to the data.

3.5 Electrical Resistivity Measurements

Electrical resistances were measured by the four probe method. For this purpose the samples were cold pressed into pellets ($\varnothing = 6$ mm, thickness 1 mm) and sintered for several hours at temperatures from 873 K to 1123 K. Then the pellets were fixed on the brass sample carrier using the epoxy resin StycastTM 2850FT (EMERSON & CUMING, catalyst Tetraethylenepentamine) and copper wires (LAKESHORE, Quad-TwistT-Cryogenic wire 36 AWG) were fixed to the surface of the sample by silver conduction paint. Temperature dependent measurements of the *dc* resistivity between 10 K and 300 K were carried out using a closed-cycle He-cryostat (Cold Head, CTI CRYOGENICS, Model 22 CP) connected to a temperature controller (LAKESHORE, Model 331) with a silicon diode temperature sensor. Data logging was performed by using the program LEITMESS.^[41] All data were interpreted and visualized with ORIGIN.^[25]

4 BaFe₂As₂

4.1 Motivation

The discovery of superconductivity in doped iron arsenide oxides^[9] in 2008 with superconducting transition temperatures up to $T_C = 26$ K in LaFeAs(O_{1-x}F_x) ($x \approx 0.11$) captured the imaginations of physicists and chemists worldwide. In these systems the isotypic phosphides LaNiPO and LaFePO had been already known to show superconductivity, although only at low temperatures between 4 K and 7 K.^[42-44] After the report of the fluoride doped iron arsenide oxide LaFeAs(O_{1-x}F_x) with $T_C = 26$ K new results on higher critical temperatures have been posted almost daily on the pre-print server of the Cornell University Library (arXiv.org). Within a couple of days the transition temperature was increased from 26 K in LaFeAs(O_{1-x}F_x) to 55 K in SmFeAs(O_{1-x}F_x).^[10] Beside the substitution with fluoride, either the replacement of lanthanum with divalent strontium (La_{1-x}Sr_xFeAsO, $T_C = 25$ K)^[14] or a lower oxygen content like in SmFeAsO_{1-x}^[45] ($T_C = 55$ K) can be used to induce superconductivity in the parent compounds. Since the discovery of the cuprate superconductors in 1986,^[2,3] no other material has reached superconducting transition temperatures as high as 55 K. These iron based superconductors represent the second class of high T_C superconductors after the discovery of the cuprates more than 20 years ago.

The non-superconducting parent compound LaFeAsO and other so called 1111 pnictide oxide superconductors crystallize in the tetragonal ZrCuSiAs-type structure (space group $P4/nmm$).^[12] In this filled variant of the PbFCl type, two-dimensional layers of edge-sharing FeAs_{4/4} tetrahedra alternate with sheets of edge-sharing OLa_{4/4} tetrahedra along the c -axis as shown on the left side in Figure 4.1. This two-dimensional character of LaFeAsO involves different types of chemical bonding, which is strongly ionic in the LaO layers and rather

covalent in the FeAs layers, respectively. The metallic and superconducting properties of LaFeAsO emerge from the FeAs layers.

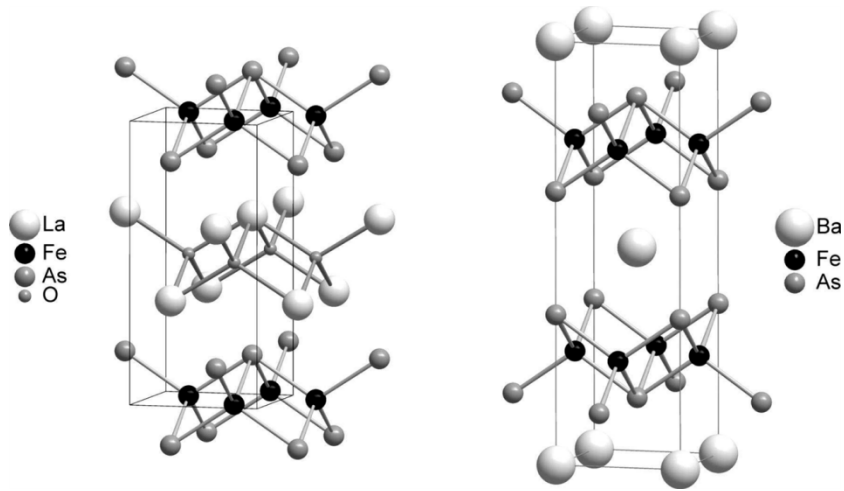


Figure 4.1: Crystal structures of LaFeAsO (left, ZrCuSiAs-type) and BaFe₂As₂ (right, ThCr₂Si₂-type).

The observation of superconductivity in doped LaFeAsO is believed to be intimately connected with magnetic fluctuations and a spin density wave (SDW) anomaly within the FeAs layers.^[46,47] A spin density wave is an antiferromagnetic ground state of metals where the density of the conduction electron spins is modulated in a periodic way. One of the most studied systems in this context is the element chromium, which is the archetypal itinerant antiferromagnet and undergoes a transition from a paramagnetic to SDW state at a Néel temperature of 311 K.^[48]

Undoped LaFeAsO undergoes a SDW-driven structural phase transition at about 150 K, associated with a reduction of the tetragonal to orthorhombic symmetry and anomalies in electrical resistance, specific heat and the magnetic susceptibility. Neutron scattering experiments show an antiferromagnetic ordering of the magnetic moments ($0.36 \mu_B / \text{Fe}$) below $T_N = 134$ K. This phase transition and magnetic ordering is suppressed by electron doping with fluoride or oxygen deficiency, as well as by hole doping with strontium. The tetragonal

phase becomes superconducting at critical temperatures between 25 and 41 K.^[9,13,14] Thus, there is an evidence that superconductivity emerges from specific structural and electronic conditions of the iron arsenide layers. However, if only the FeAs layer is essential, other structure types could serve as parent compounds as well.

Another well-known structure type which shows very similar structural conditions is the ThCr₂Si₂-type structure that comprises about 600 compounds.^[15] Although this is one of the largest families of compounds, superconductivity among these materials is extremely rare.^[49] LaIr₂Ge₂, LaRu₂P₂, YIr_{2-x}Si_{2+x} and BaNi₂P₂ are examples, but in these materials superconductivity occurs at very low temperatures (below 5 K).^[50-53] Another representative of the ThCr₂Si₂-type structure compounds is BaFe₂As₂.^[16] In this tetragonal structure (space group *I4/mmm*) layers of edge-sharing FeAs_{4/4} tetrahedra, like in LaFeAsO, alternate simply with barium atoms instead of LaO sheets in contrast to the 1111 compound. As the FeAs layers are two-dimensional and do not have contact to the neighboring FeAs layers, BaFe₂As₂ is strictly speaking a member of the BaZn₂P₂-type structure, which is one variant of the ThCr₂Si₂-type. The synthesis of BaFe₂As₂ was already reported in 1980, but except for the crystal structure and some indeterminate magnetic data,^[17] no physical properties were known.

Apart from the closely related geometry of the crystal structures, the electron counts of the FeAs layers in LaFeAsO and BaFe₂As₂ are identical as in both cases one electron is transferred to the FeAs sheets according to (LaO)⁺(FeAs)⁻ and Ba_{0.5}²⁺(FeAs)⁻, respectively.

With regard to the previously described structural and electronic properties of LaFeAsO the ThCr₂Si₂-type compound BaFe₂As₂ looks like a very promising candidate to show similar behavior like the 1111 compound for both, electronic and structural reasons. But does BaFe₂As₂ really exhibit the same SDW anomaly as LaFeAsO and could this oxygen-free variant of iron arsenides serve as a parent compound for the new high-*T_C* superconductors?

4.2 Sample Preparation

BaFe₂As₂ was synthesized by heating a mixture of distilled barium metal, iron powder and sublimed arsenic at a ratio of 1.05 : 2 : 2 in an alumina crucible, which was sealed in a silica tube under an atmosphere of purified argon. The mixture was heated to 1123 K at a rate of 50 K / h. It was kept at this temperature for 10 h and cooled down to room temperature. The reaction product was homogenized directly in the crucible using an awl, sealed again in a silica ampoule under argon atmosphere and annealed at 1173 K for 25 h. The obtained black crystalline powder of BaFe₂As₂ is stable in air.

To obtain pellets for electric resistance measurements the sample was homogenized in an agate mortar, pressed into a pellet ($\varnothing = 5$ mm, thickness 1 mm), and sintered at 973 K for 12 hours.

4.3 Crystal Structure Investigations

Phase purity was checked by X-ray powder diffraction using a Huber G670 Guinier imaging plate diffractometer. The Rietveld refinements of BaFe₂As₂ were performed with the GSAS package.^[22] Figure 4.2 shows the pattern of BaFe₂As₂ at room temperature, which could be completely fitted with a single phase.

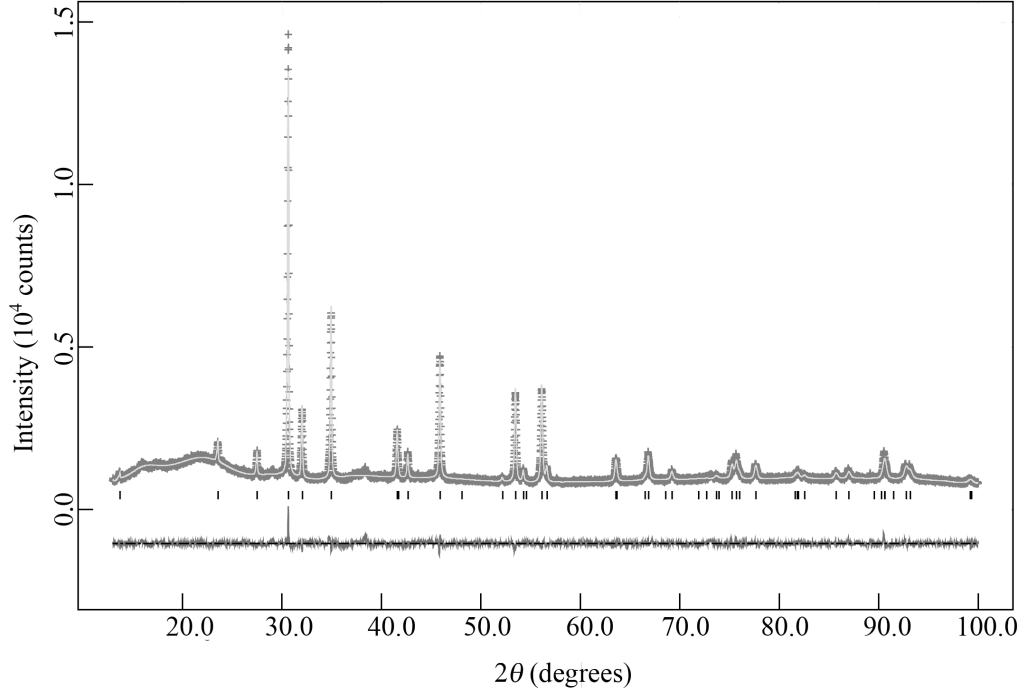


Figure 4.2: X-ray powder pattern (+) and Rietveld fit (–) of BaFe₂As₂ at 297 K (space group *I4/mmm*).

In order to check for a structural phase transition as it was known from LaFeAsO, temperature dependent X-ray powder diffraction data between 297 K and 20 K were collected. Below approximately 140 K a broadening of several reflections and with further decreasing temperature the splitting of these reflections was clearly observed (see Figure 4.3). The reflections of the powder diagrams below 136 K could be indexed with an orthorhombic *F*-centered unit cell and refined in the space group *Fmmm*. The orthorhombic lattice parameters are given by:

$$a_{\text{ortho}} = a_{\text{tetra}} \cdot \sqrt{2} + \delta$$

$$b_{\text{ortho}} = b_{\text{tetra}} \cdot \sqrt{2} - \delta \quad \text{with } \delta \approx 5 \text{ pm}$$

$$c_{\text{ortho}} \approx c_{\text{tetra}}$$

Figure 4.3 shows the Rietveld fit of the data at 20 K. The continuous transition of the pattern between 150 and 40 K, as well as the changing of lattice parameters, is depicted in the inset in Figure 4.3. The values for the lattice parameters of the tetragonal phase above 140 K are multiplied by a factor of $\sqrt{2}$ for comparability.

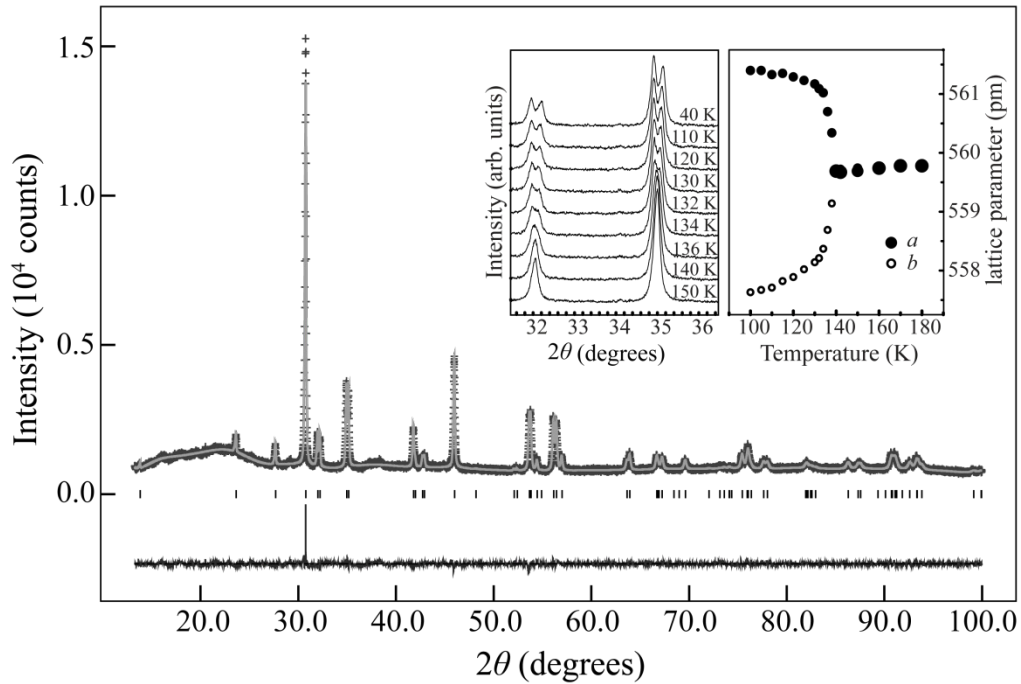


Figure 4.3: X-ray powder pattern (+) and Rietveld fit (–) of BaFe₂As₂ at 20 K (space group *Fmmm*). Inset: Splitting of the 110 and 112 reflections and variations of lattice parameters with temperature.

The *a* and *b* lattice parameters change continuously during the orthorhombic distortion with decreasing temperature and saturate at a certain temperature (≈ 120 K). This stepless variation hints at a second order phase transition from the tetragonal to the orthorhombic phase which is allowed by symmetry, since the orthorhombic space group is a subgroup of the tetragonal space group.

In terms of group theory the structural transition from *I4/mmm* to *Fmmm* is *translationgleich* with index two. A symmetry reduction scheme is depicted in Figure 4.4 and shows the basis transformation as well as the coordinate transformations.

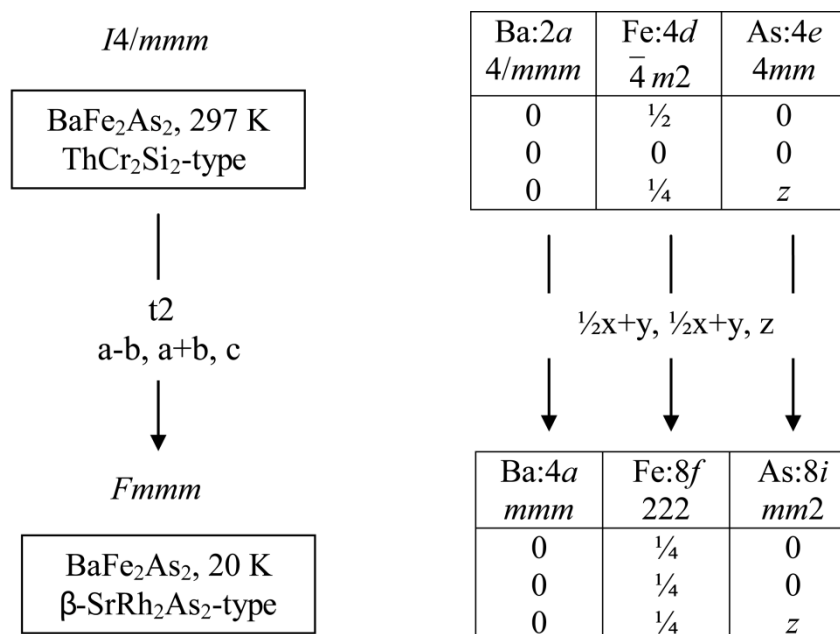


Figure 4.4: Symmetry reduction of the tetragonal space group *I4/mmm* to its subgroup *Fmmm*.

The crystallographic data of the measurements at 297 K and 20 K are summarized in Table 4.1.

Table 4.1: Crystallographic data of BaFe₂As₂.

Temperature (K)	297	20
Space group	<i>I4/mmm</i>	<i>Fmmm</i>
<i>a</i> (pm)	396.25(1)	561.46(1)
<i>b</i> (pm)	= <i>a</i>	557.42(1)
<i>c</i> (pm)	1301.68(3)	1294.53(3)
<i>V</i> (nm ³)	0.20438(1)	0.40514(2)
<i>Z</i>	2	4
Data points	8700	8675
Reflections	50	74
Atomic parameters	4	4
Profile Parameters	4	4
<i>d</i> range	0.979-6.508	0.981-6.473
<i>R_p</i> , <i>wR_p</i>	0.0273, 0.0358	0.0283, 0.0365
<i>R</i> (<i>F</i> ²), χ^2	0.0522, 1.431	0.0576, 1.392
Atomic parameters		
Ba	2 <i>a</i> (0,0,0) <i>U</i> _{iso} = 95(5)	4 <i>a</i> (0,0,0) <i>U</i> _{iso} = 69(5)
Fe	4 <i>d</i> (½,0,¼) <i>U</i> _{iso} = 57(6)	8 <i>f</i> (¼,¼,¼) <i>U</i> _{iso} = 64(4)
As	4 <i>e</i> (0,0, <i>z</i>) <i>z</i> = 0.3545(1) <i>U</i> _{iso} = 99(5)	8 <i>i</i> (0,0, <i>z</i>) <i>z</i> = 0.3538(1) <i>U</i> _{iso} = 65(5)
Bond lengths (pm)		
Ba–As	338.2(1) x 8	336.9(1) x 4 338.5(1) x 4
Fe–As	240.3(1) x 4	239.2(1) x 4
Fe–Fe	280.2(1) x 4	280.7(1) x 2 278.7(1) x 2
Bond angles (deg)		
As–Fe–As	111.1(1) x 2 108.7(1) x 4	111.6(1) x 2 108.7(1) x 2 108.1(1) x 2

In the orthorhombic structure the Fe–As bond length shorten by approximately 1 pm and the FeAs-tetrahedra get slightly distorted which results in three, instead of two different As–Fe–As bond angles compared to the tetragonal phase. The main structural effect of the phase transition, however, appears in the Fe–Fe distances, where four equal bonds of 280.2 pm lengths split into two pairs of 280.8 pm and 278.7 pm. The *ab*-planes of the tetragonal and orthorhombic phases are depicted in Figure 4.5. The cell edges are highlighted in green color. In the tetragonal cell (left-hand side, Fig. 4.5) the four equal Fe–Fe bonds are illustrated as dotted lines, whereas in the orthorhombic structure the Fe–Fe atomic distances shorten and the bonds are therefore depicted as solid lines. This supports the idea, that the Fe–Fe interactions are strongly correlated with the SDW anomaly and may play a certain role concerning the physical properties of BaFe₂As₂.

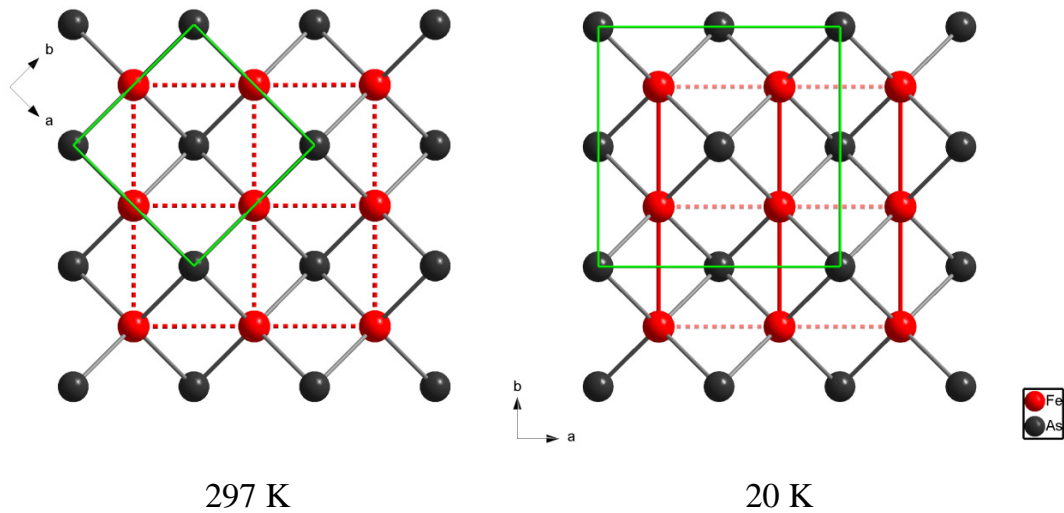


Figure 4.5: High temperature tetragonal (left) and low temperature orthorhombic structure (right). Cell edges are highlighted by green lines. For clarity, only the iron and arsenic atoms parallel to the *ab*-plane are depicted. The basal plane parameters are related to each other by $a_{\text{tetra}} = b_{\text{tetra}}$ (left hand side) and $a_{\text{ortho}} = \sqrt{2} \cdot a_{\text{tetra}} + \delta$, $b_{\text{ortho}} = \sqrt{2} \cdot b_{\text{tetra}} - \delta$, $c_{\text{ortho}} \approx c_{\text{tetra}}$, $\delta \approx 5\text{pm}$ (right hand side).

4.4 Specific Heat Measurements

As the lattice parameters seem to vary second-order-like during cooling, specific heat measurements were carried out in order to get more detailed information on the nature of the phase transition. The specific heat data were collected between 3 K and 200 K by relaxation time method in a PPMS (Quantum Design, Inc.) at the Universität Münster in the group of Prof. Dr. Pöttgen. In Figure 4.6 an anomaly in the specific heat at about 140 K can be seen clearly. This characteristic λ -like shape of the peak points to a second-order transition, as it is typical for magnetic ordering or displacive structural change. The transition temperature of 139.9 ± 0.5 K can be extracted from the inflection point of the λ anomaly. Analysis of the heat capacity yields a Debye temperature of $\Theta_D = 134(1)$ K and a Sommerfeld coefficient γ of $16(2)$ mJ / (K² mol). The Sommerfeld coefficient γ of BaFe₂As₂ is significantly bigger than, e.g. the Sommerfeld coefficient of good metals like Cu (0.67 mJ / (K² mol))^[54] but much smaller than in the so-called heavy-fermion-systems like CeCu₂Si₂ ($\gamma \approx 1050$ mJ / (K² mol)).^[54]

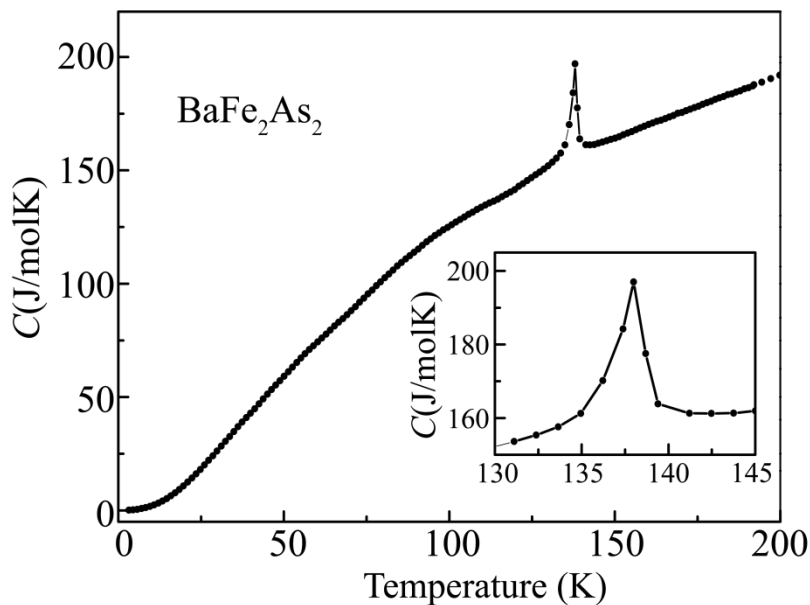


Figure 4.6: Specific heat of BaFe₂As₂ versus temperature.

There have been many debates whether this transition is continuous, first-order or weakly first-order. This subject has also been discussed at length by Wilson *et al.*^[55] They studied the magnetic and structural phase transitions within large, high quality single crystals of BaFe₂As₂ by neutron diffraction and concluded, that in strain-free crystals, the transition is essentially continuous, which confirms the results discussed above.

4.5 Electrical Resistance of BaFe₂As₂

As mentioned above, the SDW driven transition of LaFeAsO from the tetragonal space group $P4/nmm$ to the orthorhombic space group $Cmme$ leads to anomalies in the electrical resistivity as well. To check for such an anomaly in BaFe₂As₂, temperature dependent measurements of the *dc* electrical resistance were performed. The result is shown in Figure 4.7.

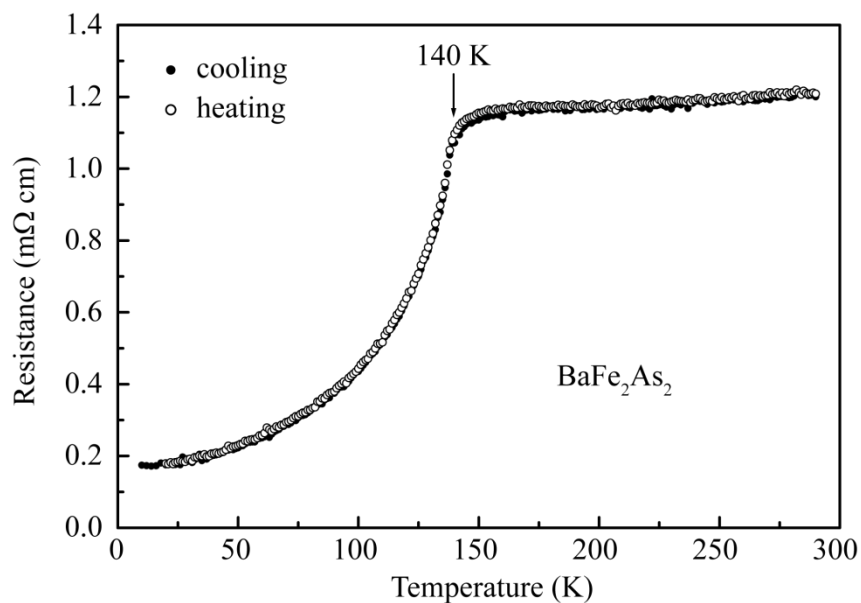


Figure 4.7: *dc* electrical resistance of BaFe₂As₂ ($I = 100 \mu\text{A}$).

BaFe₂As₂ is a poor metal with a relatively high specific resistance of $1.2 \cdot 10^{-5} \Omega\text{m}$ at room temperature which decreases only slightly on cooling. For comparison, the resistivity of copper metal at room temperature is about $1.6 \cdot 10^{-8} \Omega\text{m}$.^[56] At 140 K, the resistance drops abruptly at first but then decreases monotonically to $0.2 \cdot 10^{-5} \Omega\text{m}$ at 10K, according to a relative resistance ratio (*RRR*) of 6. This behavior corresponds to undoped LaFeAsO, where the resistance is of the same magnitude at room temperature and drops in similar fashion.^[46]

4.6 Magnetic Susceptibility

Next, the general magnetic properties and the specific magnetic behavior at the phase transition were investigated. The magnetic susceptibility was measured with a SQUID magnetometer (MPMS-XL5, Quantum Design, Inc.) at 0.5 T (Figure 4.8).

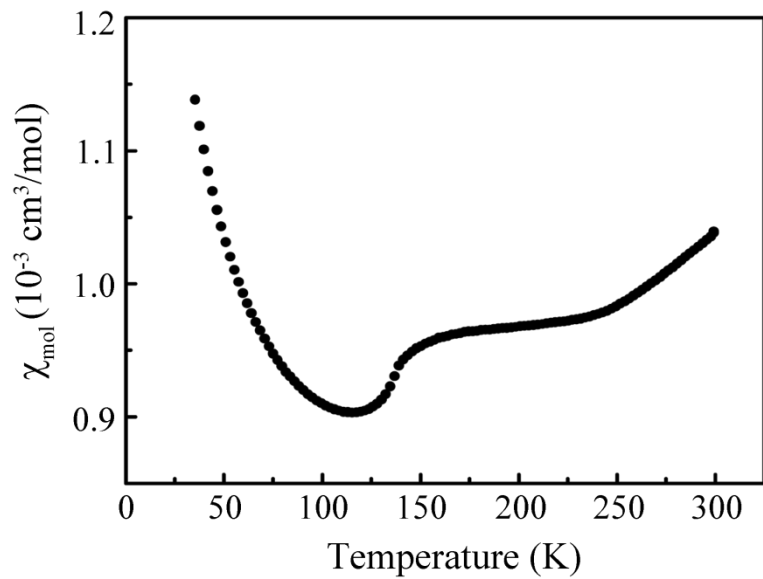


Figure 4.8: Magnetic susceptibility of BaFe₂As₂ at 0.5 T.

BaFe₂As₂ shows a weak and only slightly temperature-dependent paramagnetism. Below 140 K the magnetic susceptibility χ drops at first but

increases again below 100 K. The latter fact may be attributed to traces of ferromagnetic impurities, which were not detectable by X-ray powder diffraction method.

Later, further magnetic measurements at temperatures up to 700 K, performed by Wang *et al.*,^[57] revealed a linear increase of the susceptibility with increasing temperatures above the SDW transition. This increase has been attributed to itinerant electron antiferromagnetic spin fluctuations and is interestingly also found for other spin density wave systems such as chromium above T_{SDW} .^[48]

4.7 ⁵⁷Fe Mössbauer Spectroscopy

For ⁵⁷Fe Mössbauer spectroscopy investigations a ⁵⁷Co/Rh source was available at the Universität Münster in the group of Prof. Dr. Pöttgen. The BaFe₂As₂ sample was placed in a thin-walled PVC container at a thickness of about 10 mg Fe / cm². The measurements were performed in the usual transmission geometry in the temperature range from room temperature to 4.2 K. The source was kept at room temperature.

The ⁵⁷Fe Mössbauer spectra at different temperatures are depicted in Figure 4.9 together with the transmission integral fits. The corresponding fitting parameters are listed in Table 11.1 in the appendix. At room temperature, the spectrum consists of a single Lorentzian line with an isomer shift of $\delta = 0.31(1)$ mm / s. The observed isomer shift is slightly smaller than in LaFeAsO (0.44 mm / s).^[58,59] At 298 K the experimental line width amounts to 0.32 mm / s which significantly broadens to 0.46 mm / s at 155 K. That hints at magnetic fluctuations that lead to some extent to short-range magnetic ordering (nematic order) well above the structural distortion taking place at 140 K. Hence, magnetic ordering is most likely already present when the structural distortion occurs. When lowering the temperature below the SDW transition temperature of 138 K, a strong increase of the internal hyperfine field with a saturation value of

5.47(1) T at 4.2 K is observed. This corresponds to a magnetic moment of approximately $0.4 - 0.5 \mu_B$ per iron atom. The temperature-dependent development of the magnetic hyperfine field is illustrated in Figure 4.10.

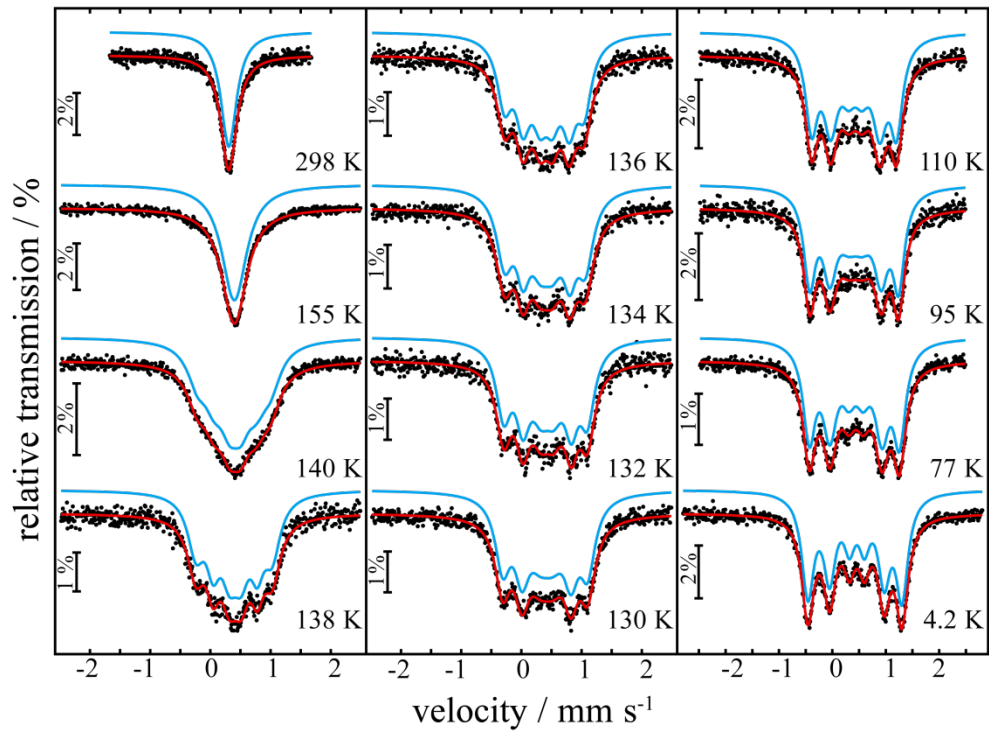


Figure 4.9: ⁵⁷Fe Mössbauer spectra of BaFe₂As₂.

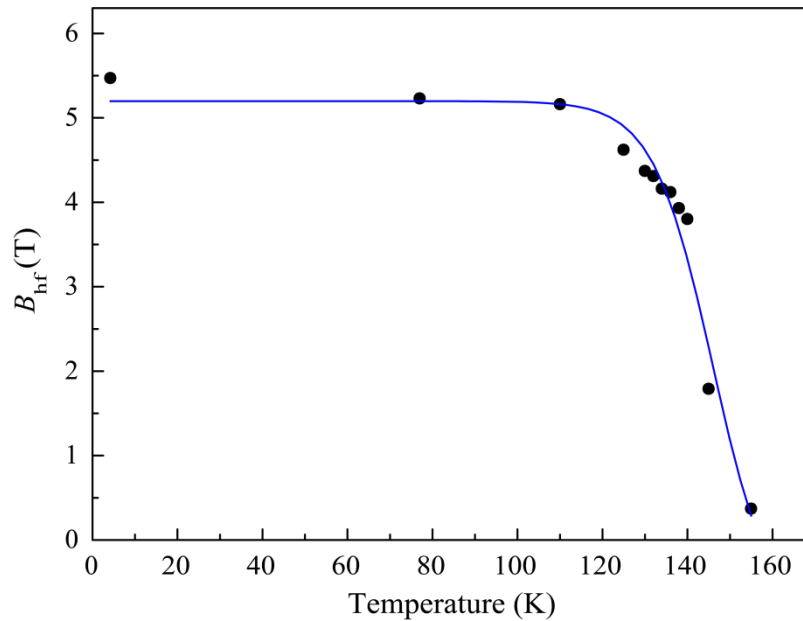


Figure 4.10: Temperature-dependent development of the magnetic hyperfine field in BaFe₂As₂. The blue line is a guide for the eye.

A similar behavior has been observed for the SDW system LaFeAsO below the transition temperature,^[58-61] where the saturation hyperfine field accounts 5.3 T. The magnetically split spectra can be well reproduced by one spectral component with the typical sextet of lines with a very small quadrupole splitting parameter of $-0.04(1)$ mm / s at 4.2 K. This is in contrast to the ZrCuSiAs-type compound LaFeAsO^[58] which shows distributions of moments in the magnetically ordered states, indicating that some spin disorder still remains.

4.8 Magnetic Structure

The magnetic nature of the structural phase transition in BaFe₂As₂ has been demonstrated by the Mössbauer spectra at low temperatures discussed above. With respect to the susceptibility data, antiferromagnetic order was expected. Neutron diffraction experiments with polycrystalline BaFe₂As₂ by Huang *et al.*^[62] clarified the complete spin structure, which is illustrated in Figure 4.11.

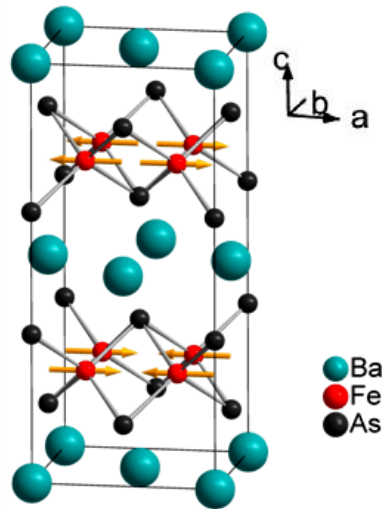


Figure 4.11: Magnetic structure of BaFe₂As₂. The magnetic moment is $0.83(3) \mu_B / \text{Fe}$.^[62]

The fundamental magnetic wave vector is $q = (101)_o$, thus the magnetic moments are anti-parallel aligned to the longer orthorhombic a -axis and also antiferromagnetically along the c -axis. Along b (longer Fe–Fe distance in rectangular Fe nets) the moments form ferromagnetic chains. Thus, BaFe₂As₂ shows a stripe-type antiferromagnetic order at low temperatures.

About the same time neutron diffraction experiments were carried out using single crystals of BaFe₂As₂ which were grown from a tin flux.^[63] Due to approximately five percent tin incorporation, these specimens showed substantially different phase transition and magnetic ordering temperatures of about 90 K. The determined magnetic structure, however, agrees with the powder results of Huang *et al.*,^[62] which show the magnetic transition at $T_N \approx 143$ K. Later, the experiments were conducted with tin-free crystals.^[64] The results confirmed the spin structure again and proved that the tin incorporation affected the transition temperatures, but not the magnetic structure.

4.9 Single Crystal Growth of BaFe₂As₂

4.9.1 Synthesis

As already mentioned in connection with neutron diffraction, one convincing advantage of the oxygen-free iron arsenide BaFe₂As₂ is single crystals growth. First attempts to obtain single crystals have been made by growing them out of a tin-flux. A mixture of distilled barium metal, iron powder and sublimed arsenic at a ratio of 1.05 : 2 : 2 were mixed with four times the amount of tin granules in an alumina crucible, which was sealed in a silica tube under an atmosphere of purified argon. The mixture was heated to 573 K at a rate of 100 K / h and afterwards the temperature was elevated to 873 K at a rate of 20 K / h. It was kept at this temperature for three hours and heated again to 1123 K at a rate of 50 K / h. After keeping the sample at this temperature for another 36 h and cooling down to room temperature by shutting down the furnace, the tin flux was removed by using half concentrated hydrochloric acid to finally obtain the silver shiny, plate-like crystals. The recorded powder diffraction data show a pattern very similar to BaFe₂As₂ but with slightly shifted reflections. Figure 4.12 shows an excerpt of the powder diagram of the Sn flux grown BaFe₂As₂ compared to the powder sample.

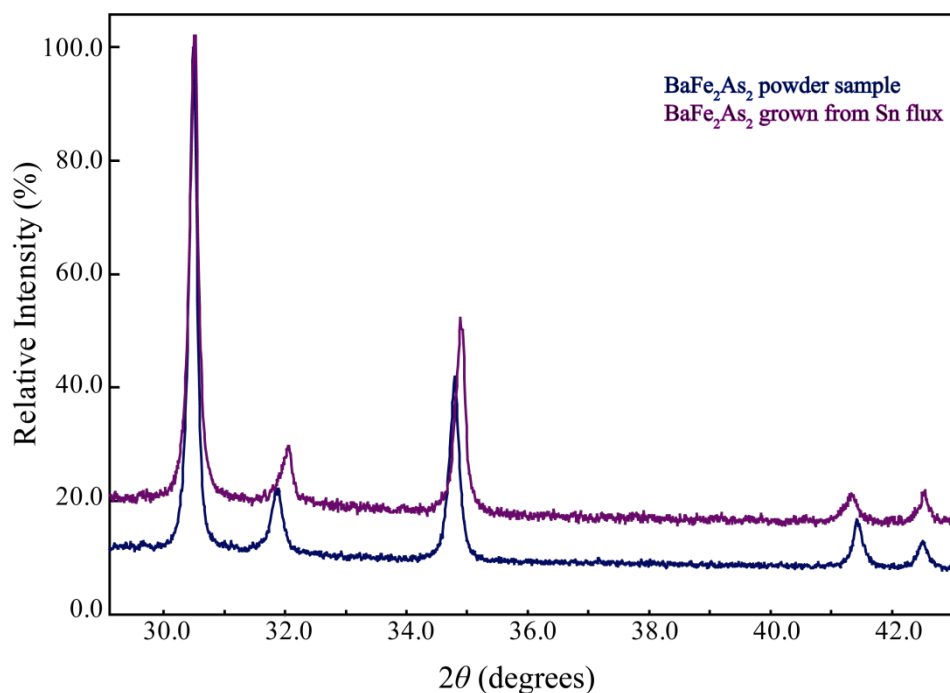


Figure 4.12: Excerpt of the powder diagram of Sn flux grown BaFe₂As₂ compared to the powder sample.

4.9.2 Crystal Structure Analysis

A single crystal was isolated and examined by means of Laue photographs in order to check for suitability for an intensity data collection. The single crystal data were collected at room temperature by an IPDS diffractometer (STOE & Cie GmbH). A numerical absorption correction was applied. All relevant details of the data collection and evaluation are listed in Table 4.2.

The atomic parameters of BaFe₂As₂ were taken as starting values and the structure was refined using SHELXL-97 (full matrix least squares on F^2)^[35,36] with anisotropic atomic displacement parameters for all atoms. After several cycles of refinement a residual electron density peak of 4.79 e/Å³ was detected in the Fourier difference map, which was close to, but displaced from the Ba site. A detailed Fourier difference map is depicted in Figure 4.13.

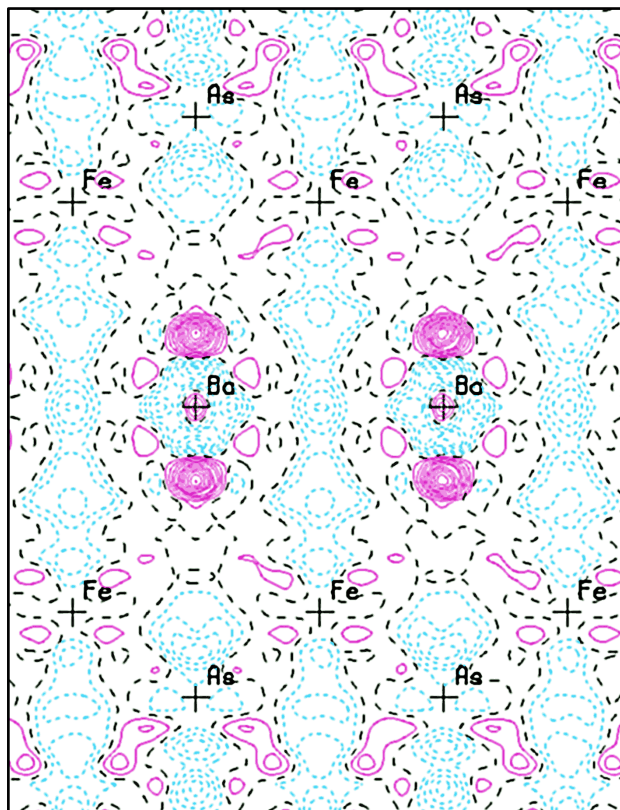


Figure 4.13: Fourier difference map showing a cut through the *ac* plane. Violet color indicates residual electron density peaks. Furthermore, the electron holes (blue) and isolines (black) are illustrated.

As the single crystals were grown out of a tin flux, a possible incorporation of Sn-atoms in the structure was considered. Further refinements were therefore performed with Sn located in the position of the residual peak, and the occupation parameter of Sn refined. Inserting Sn decreased the Goodness-of-Fit of the refinement considerably from 2.29 to 1.19. Table 4.3 and 4.4 show selected positional parameters of the refinement, displacement parameters, interatomic distances and angles.

Table 4.2: Crystal data and structure refinement of (Ba_{0.95}Sn_{0.05})Fe₂As₂ (standard deviations in parantheses).

Formula	(Ba _{0.95} Sn _{0.05})Fe ₂ As ₂
Molar mass (g/mol)	517.57
Crystal system	Tetragonal
Space group	<i>I4/mmm</i>
Diffractometer	STOE IPDS
Radiation	Mo-K α ($\lambda = 71.073$ pm)
<i>a</i> (pm)	394.84(7)
<i>c</i> (pm)	1308.5(4)
<i>V</i> (nm ³)	0.20399(8)
<i>Z</i>	2
Temperature (K)	293
Calculated density (g/cm ³)	8.421
Absorption coefficient (mm ⁻¹)	38.41
<i>h</i>	-6 \rightarrow 5
<i>k</i>	-6 \rightarrow 5
<i>l</i>	-19 \rightarrow 19
Total no. reflections	1378
Independent reflections	142
Reflections $I > 2\sigma(I)$	129
Refined parameters	13
R_1 with $I > 2\sigma(I)$ / all reflections	0.018 / 0.021
wR_2 with $I > 2\sigma(I)$ / all reflections	0.037 / 0.037
Goodness-of-fit (F^2)	1.195
Largest residual peak, hole (e/ \AA^3)	0.81 / -1.40

Table 4.3: Atomic coordinates, equivalent isotropic displacement parameters $U_{eq}/\text{\AA}^2$, and anisotropic displacement parameters / \AA^2 of (Ba_{0.95}Sn_{0.05})Fe₂As₂ (space group *I4/mmm*).

(Ba _{0.95} Sn _{0.05})Fe ₂ As ₂	Wyck.	x	y	z	sof	U_{eq}	
Ba	$2a$	0	0	0	0.954(3)	0.0129(2)	
Sn	$4e$	0	0	0.093(2)	0.046(3)	0.048(7)	
Fe	$4d$	1/2	0	1/4	1	0.0095(2)	
As	$4e$	0	0	0.35433	1	0.0093(3)	
		U_{11}	U_{22}	U_{33}	U_{23}	U_{13}	U_{12}
Ba		0.0130(2)	0.0130(2)	0.0127(4)	0	0	0
Sn		0.0252(52)	0.0252(52)	0.0942(187)	0	0	0
Fe		0.0091(2)	0.0091(2)	0.0104(4)	0	0	0
As		0.0081(3)	0.0081(3)	0.0118(5)	0	0	0

Table 4.4: Interatomic distances / pm and bond angles / ° in (Ba_{0.95}Sn_{0.05})Fe₂As₂.

(Ba _{0.95} Sn _{0.05})Fe ₂ As ₂	
Distances (pm)	
Ba–As	338.05(6) (8×)
Fe–As	240.03(5) (4×)
Fe–Fe	279.19(5) (4×)
Sn–As	287.5(7) (4×)
Angles (°)	
As–Fe–As	108.87(2) (4 ×)
	110.67(3) (2 ×)
As–Ba–As	71.46(1) (8 ×)
As–Sn–As	86.7(3) (4 ×)

4.9.3 Crystal Structure Description

Compared to the structure of BaFe₂As₂, the *a*-lattice parameter in (Ba_{0.95}Sn_{0.05})Fe₂As₂ slightly shortens from 396.25 pm in BaFe₂As₂ to 394.84 pm whereas the *c*-lattice parameter is extended from 1301.68^[65] to 1308.5 pm. Only 95 % of the 2*a* site is occupied by Ba-atoms whereas the missing 5 % are found to be substituted by Sn-atoms which occupy the 4*e* site (00*z* with *z* = 0.093). This displacement is accounted to the stereochemical active lone pair of the formal divalent tin atom. The shifting of 0.093 in *z*-direction results in a change of the coordination sphere which is then a Sn²⁺-typical square pyramidal coordination by four As atoms. The Ba atoms by contrast are coordinated by eight As atoms in a distorted cubic environment. The crystal structure is illustrated in Figure 4.14.

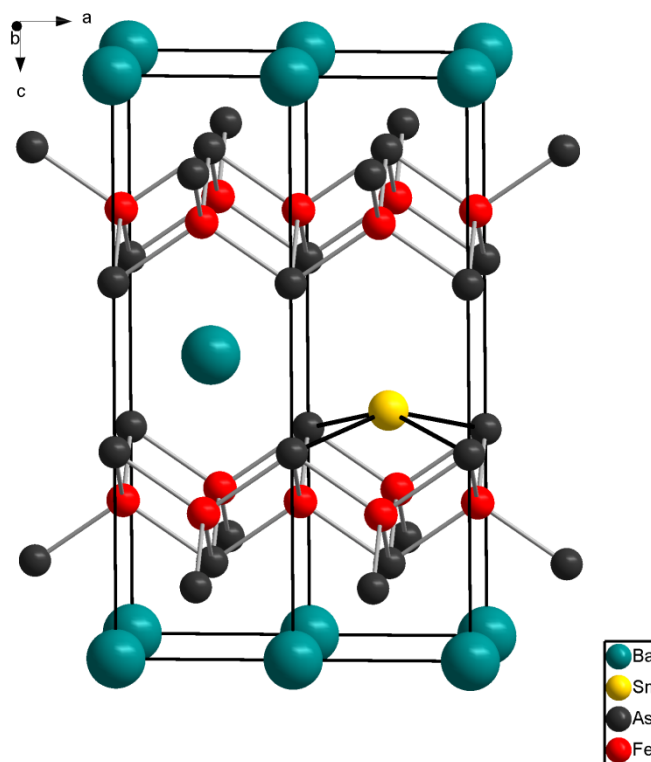


Figure 4.14: Crystal structure of (Ba_{0.95}Sn_{0.05})Fe₂As₂.

The metal-arsenic distance amounts to 338.05 pm for the Ba–As bond length, whereas the Sn–As bond length is 287.5 pm. Compared to other compounds

where tin is tetrahedrally coordinated by four arsenic atoms, 287.5 pm is too long as the interatomic distances for Sn–As bonds should range between 257.2 pm, like in Ca₅Sn₂As₆,^[66] and 275.2 pm, like in Ba₃Sn₄As₆.^[67] In contrast to (Ba_{0.95}Sn_{0.05})Fe₂As₂, however, the Sn atoms are of valence Sn⁴⁺ instead of divalent, which leads in turn to shorter interatomic distances. Examination of the bond lengths in compounds with an octahedral coordination sphere of Sn by As atoms shows that the Sn–As distances vary from 275.3 pm to 301.8 pm (Sn_{3.6}As₃).^[68] This is comparable to the value of 287.5 pm, although there is no divalency of the Sn atom as well. A simple calculation of the Sn–As bond length by adding the ionic radii of Sn²⁺ (93 pm)^[69] and As³⁻ (195.05 pm) lead to a value of 289.05 pm. The ionic radius of As³⁻ was estimated from the difference of the interatomic distance of Ba–As (338.05 pm) and the ionic radius of Ba²⁺ (142 pm)^[69] which results in 196.05 pm for As³⁻. The estimated theoretical interatomic distance is only slightly larger and matches well with the value of 287.5 pm found by the crystal structure determination.

As a consequence of the shorter distance of Sn to the As atoms the As–Sn–As angle widens to 86.7 °, compared to As–Ba–As with 71.5 °. The Fe–As and Fe–Fe bond length (240.0 pm and 279.2 pm), however, remain almost constant compared to BaFe₂As₂ (240.3 pm and 280.2 pm).^[65] The tin incorporation was also revealed by EDX measurements which resulted in the composition (Ba_{0.945}Sn_{0.055})Fe₂As₂.

4.9.4 Alternative Methods

Single crystal growth of BaFe₂As₂ from a Sn flux produces crystals with a few percent Sn incorporated into the crystal structure. This leads to a lower tetragonal-to-orthorhombic structural phase transition temperature, Néel temperature and changes in the temperature dependencies of the electrical resistivity and susceptibility.^[63,70,71] Therefore, other possibilities had to be found to grow higher quality crystals without impurities. The FeAs self flux method^[57]

is currently the best way to obtain such crystals, which allows typical sizes of $2 \times 2 \times 0.10 \text{ mm}^3$. It has been suggested that BaFe₂As₂ melts congruently above 1443 K, and the Bridgman technique has been used as well to grow the ternary compound with a crystal size of $10 \times 4 \times 2 \text{ mm}^3$.^[72] An example of a BaFe₂As₂ crystal grown by using the self flux method is shown in Figure 4.15.



Figure 4.15: Photograph of a single crystal of BaFe₂As₂ grown by the self flux method on a 2 mm grid.^[57]

Single crystals of BaFe₂As₂ grown by the self flux method during this work have been synthesized by heating Ba and FeAs in a molar ratio of 1 : 4 in an alumina crucible. The sample was heated with a heating rate of 50 K / h to 1323 K. This temperature was held for two hours and afterwards cooled down with a rate of 6 K / h to 1023 K before the furnace was turned off. After wrecking the alumina crucible, the metal ingot was carefully crushed using an agate mortar and so excess FeAs was removed from the silver shiny, plate-like crystals. Normal crystal sizes reached in these experiments were approximately $0.18 \times 0.17 \times 0.05 \text{ mm}^3$.

4.10 Discussion

The properties of the ternary iron arsenide BaFe₂As₂ with the ThCr₂Si₂-type structure have been proved to be remarkably similar to those of LaFeAsO, which is the first parent compound of the new class of high- T_C superconductors. Both materials are poor metals at room temperature and undergo second-order structural and magnetic phase transitions. The ⁵⁷Fe Mössbauer data of BaFe₂As₂ show hyperfine field splitting below 140 K, which hints at antiferromagnetic ordering. Neutron diffraction experiments revealed the magnetic structure, which is largely the same as in LaFeAsO. BaFe₂As₂ differs most significantly from LaFeAsO in the structural and magnetic phase transition temperatures. While the antiferromagnetic transition seemingly occurs at the same temperature as the structural transition in BaFe₂As₂, in all previously measured 1111-type compounds the structural and magnetic phase transitions are separated.^[73-75] Nevertheless, a broadening of the experimental line width in the ⁵⁷Fe Mössbauer spectra of BaFe₂As₂ at 155 K hints already at short range or nematic order well above 140 K. Most likely, long-range antiferromagnetic ordering occurs right before the structural distortion emerges. Therefore, magnetic fluctuations that lead to magnetic ordering are presumably the driving force for the structural phase transition. As a consequence, also the resistivity drops sharply at 140 K, because scattering of the conduction electrons due to magnetic fluctuations is strongly reduced and the electrical resistance is therefore decreasing.

Thus, BaFe₂As₂ exhibits the same SDW anomaly at 140 K as LaFeAsO at 150 K. Since the SDW instability is an important prerequisite for high- T_C superconductivity in iron arsenides, the results discussed above strongly suggest that BaFe₂As₂ can serve as a parent compound for another, oxygen-free class of iron arsenide superconductors with ThCr₂Si₂-type structure. There is everything to suggest that superconductivity can be induced either by electron or hole doping. If the latter is the case it would conclusively prove that superconductivity originates from the FeAs layers, regardless of the separating sheets.

5 Doping of BaFe₂As₂

Similar to the cuprates, superconductivity in iron arsenides emerges from two-dimensional, magnetically ordered layers. The parent compound LaFeAsO crystallizes in the ZrCuSiAs-type structure,^[12] composed by alternating (LaO)⁺ and (FeAs)⁻ layers, as described in chapter 4. The magnetic and structural phase transitions of the parent compound are suppressed by partial oxidation (hole doping) or reduction (electron doping) of the iron arsenide layers and superconductivity appears at certain doping levels. In this context, the term “doping” is commonly used by the physical community rather than by the chemical society, who would use the term “substitution” instead of “doping”. However, both terms express changes in the electron count in superconductors like YBa₂Cu₃O_{7-x} and also in other materials. The “doping levels” are arbitrary and mostly much larger than in doped semiconductors, where the term doping has its seeds. Electron doping has been highly successful by substitution of oxide for fluoride or by oxide vacancies, whereas the only case of superconductivity by hole doping is (La_{1-x}Sr_x)FeAsO ($T_C = 25$ K) so far.^[14]

In the last section the ThCr₂Si₂-type structure compound BaFe₂As₂ was proposed as a potential new parent compound due to its strikingly similar properties in comparison to the iron arsenide oxides.^[65] First attempts to realize electron doping by lanthanum substitution for barium failed, because the required doping level could not be achieved as a higher lanthanum content leads always to the formation of LaAs.

One of the most straightforward ways for hole doping of BaFe₂As₂ is the substitution of the Ba²⁺ cations for K⁺, because isostructural KFe₂As₂ had already been known to exist.^[76] Therefore, K-doping of BaFe₂As₂ should be possible, as additionally both cations have similar ionic radii (Ba²⁺: 142 pm, K⁺: 151 pm).^[69] In the iron arsenide oxides like e.g. SmFeAs(O_{1-x}F_x), highest T_C 's were reached

by doping levels of 0.15 – 0.2 electrons per (FeAs) unit.^[77] As there are two (FeAs) units on each Ba, the doping concentration should have to be doubled to create similar conditions. Thus, for BaFe₂As₂ 30 – 40 % substitution of the barium for potassium ions would be necessary.

5.1 Synthesis

(Ba_{1-x}K_x)Fe₂As₂ ($x = 0.3, 0.4$) was prepared by heating stoichiometric mixtures of the elements in alumina crucibles, welded in silica tubes under an argon atmosphere. In order to minimize the loss of potassium by evaporation, the gas volume was reduced by alumina inlays in the crucibles. The samples were heated slowly (50 K/h) to 873 K, kept at this temperature for 15 hours and cooled down to room temperature by switching off the furnace. After homogenization in the crucible with an awl in an argon-filled glove-box, the products were annealed at 925 K for 15 hours, again homogenized in an agate mortar, cold pressed into pellets, and sintered at 1023 K for 12 hours. The resulting material is black and stable in air. The same method can also be used to synthesize KFe₂As₂ which, in contrast to mixed crystals of (Ba_{1-x}K_x)Fe₂As₂, is not stable in air, and therefore handled in an argon filled glove box.

5.2 Crystal Structure of (Ba_{0.6}K_{0.4})Fe₂As₂

Phase purity was checked by X-ray powder diffraction with Cu-K _{α 1} radiation ($\lambda = 154.051$ pm) or Mo-K _{α 1} radiation ($\lambda = 71.073$ pm), respectively. Rietveld refinements of the data were performed with the GSAS package.^[22,78] The atomic parameters of BaFe₂As₂ were taken as starting values for the refinement. The refinement of the site occupation parameters in the Rietveld fit of (Ba_{0.6}K_{0.4})Fe₂As₂ proves clearly the substitution of 40 % barium for potassium. A

small impurity phase of FeAs (Westerveldite^[79]) was detected and quantified to $6 \pm 1 \%$.

As mentioned above, a crucial aspect of the LaFeAsO superconductors is the suppression of the SDW anomaly associated with the structural distortion by doping. Therefore, temperature dependent X-ray powder diffraction data of $(\text{Ba}_{0.6}\text{K}_{0.4})\text{Fe}_2\text{As}_2$ were collected between 297 K and 20 K. Figure 5.1 shows the Rietveld fit of $(\text{Ba}_{0.6}\text{K}_{0.4})\text{Fe}_2\text{As}_2$ at room temperature. The inset in Figure 5.1 depicts the temperature dependency of the (110) reflections of BaFe_2As_2 and $(\text{Ba}_{0.6}\text{K}_{0.4})\text{Fe}_2\text{As}_2$ for comparison. No broadening or splitting of the diffraction peaks was detected any more as it is found in BaFe_2As_2 below 140 K.

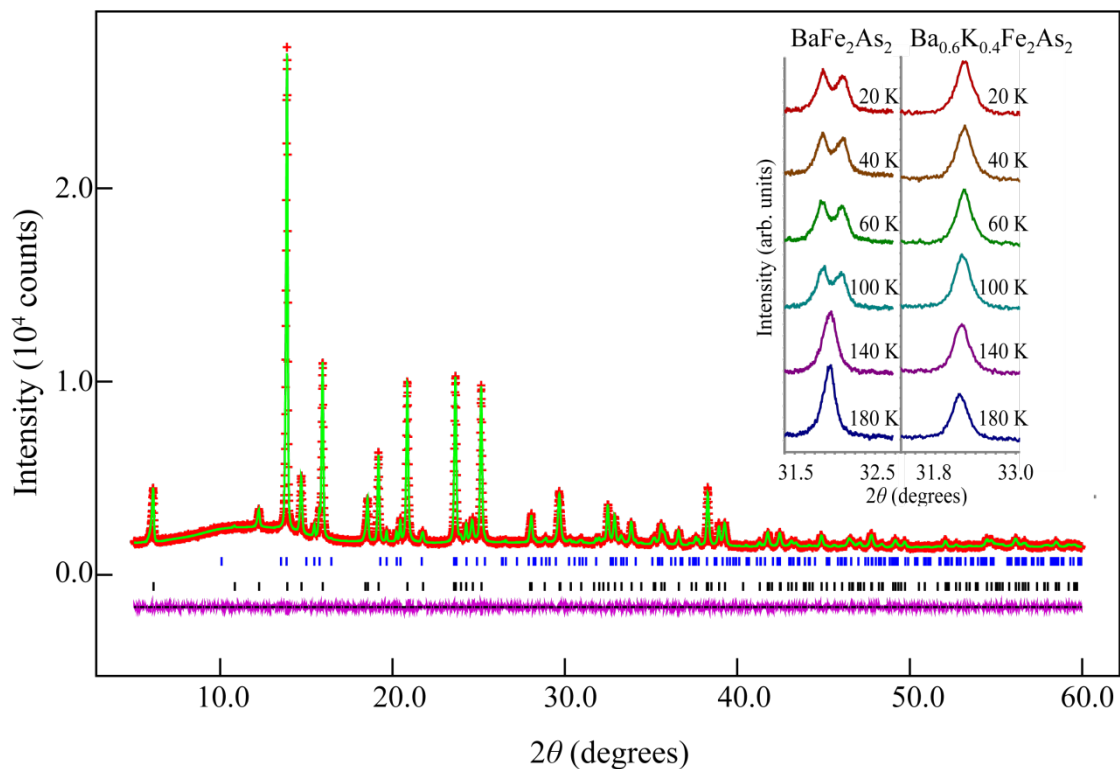


Figure 5.1: X-ray powder pattern (+) and Rietveld fit (–) of $(\text{Ba}_{0.6}\text{K}_{0.4})\text{Fe}_2\text{As}_2$ at 297 K (space group $I4/mmm$). Reflection markers are blue (upper row) for FeAs and black (lower row) for $(\text{Ba}_{0.6}\text{K}_{0.4})\text{Fe}_2\text{As}_2$. The inset shows the temperature dependency of the (110) reflections of BaFe_2As_2 and $(\text{Ba}_{0.6}\text{K}_{0.4})\text{Fe}_2\text{As}_2$.

Doping of BaFe₂As₂

The powder pattern of (Ba_{0.6}K_{0.4})Fe₂As₂ measured at 20 K has been successfully refined by using the parameters of the undistorted tetragonal structure (space group *I4/mmm*). Table 5.1 shows the almost identical crystallographic data of (Ba_{0.6}K_{0.4})Fe₂As₂ at 297 K and 20 K, respectively. Thus it is evident, that the potassium doping has suppressed the structural transition of BaFe₂As₂.

Table 5.1: Crystallographic data of (Ba_{0.6}K_{0.4})Fe₂As₂ at 297 K and 20 K.

Temperature (K)	297	20
Diffractometer	STOE	Huber G670
Radiation	Mo-K _{α1}	Cu-K _{α1}
Space group	<i>I4/mmm</i>	<i>I4/mmm</i>
<i>a</i> (pm)	391.70(1)	390.90(1)
<i>b</i> (pm)	= <i>a</i>	= <i>a</i>
<i>c</i> (pm)	1329.68(1)	1321.22(4)
<i>V</i> (nm ³)	0.20401(1)	0.20189(1)
<i>Z</i>	2	2
Data points	5499	8790
Reflections	405	127
Atomic parameters	4	4
Profile Parameters	10	10
<i>d</i> range	0.639-6.648	0.971-6.606
<i>R</i> _p , <i>wR</i> _p	0.0202, 0.0258	0.0214, 0.0283
<i>R</i> (<i>F</i> ²), χ^2	0.026, 1.347	0.093, 1.816
Atomic parameters		
Ba, K	2 <i>a</i> (0,0,0) <i>U</i> _{iso} = 130(8)	2 <i>a</i> (0,0,0) <i>U</i> _{iso} = 89(8)
Fe	4 <i>d</i> (½,0,¼) <i>U</i> _{iso} = 47(4)	4 <i>d</i> (½,0,¼) <i>U</i> _{iso} = 84(7)
As	4 <i>e</i> (0,0, <i>z</i>) <i>z</i> = 0.3538(1) <i>U</i> _{iso} = 70(3)	4 <i>e</i> (0,0, <i>z</i>) <i>z</i> = 0.3538(1) <i>U</i> _{iso} = 76(7)
K : Ba ratio	42(1) : 58(1)	38(1) : 62(1)
Bond lengths (pm)		
Ba-As	338.4(1) x 8	337.2(1) x 8
Fe-As	239.6(1) x 4	238.8(1) x 4
Fe-Fe	277.0(1) x 4	276.4(1) x 4
Bond angles (deg)		
As-Fe-As	109.7(1) x 2 109.4(1) x 4	109.9(1) x 2 109.3(1) x 4

5.3 Electrical Resistance Measurements

Electrical resistance measurements were carried out by applying the four probe method. For this purpose the samples were cold pressed into pellets ($\varnothing = 6$ mm, thickness 1 mm) and sintered 10 hours at 873 K. As depicted on the left hand side in Figure 5.2, BaFe₂As₂ has the highest resistance and shows a decrease at 140 K, which is linked to the SDW anomaly.^[65] In contrast to this, the resistance of KFe₂As₂ is considerably smaller and decreases smoothly, as it is typical for normal metals. The resistance of K-doped (Ba_{0.6}K_{0.4})Fe₂As₂ is similar to KFe₂As₂ and does not show any anomaly at about 140 K, in agreement with the structural data. But the resistance drops abruptly to zero at ≈ 38 K, which clearly indicates superconductivity. On the right hand side in Figure 5.2 details of the transition are shown. By using the 90 / 10 criterion, the midpoint of the resistive transition is at 38.1 K and has a transition width of 1.5 K. The first deviation from the extrapolated resistance is at ≈ 39 K, and zero resistance is achieved at 37.2 K. Consequently, this oxygen-free compound with ThCr₂Si₂-type structure shows superconductivity analogue to the LaFeAsO materials. To this day, the T_C of 38 K is the highest critical temperature observed in hole doped iron arsenide superconductors.

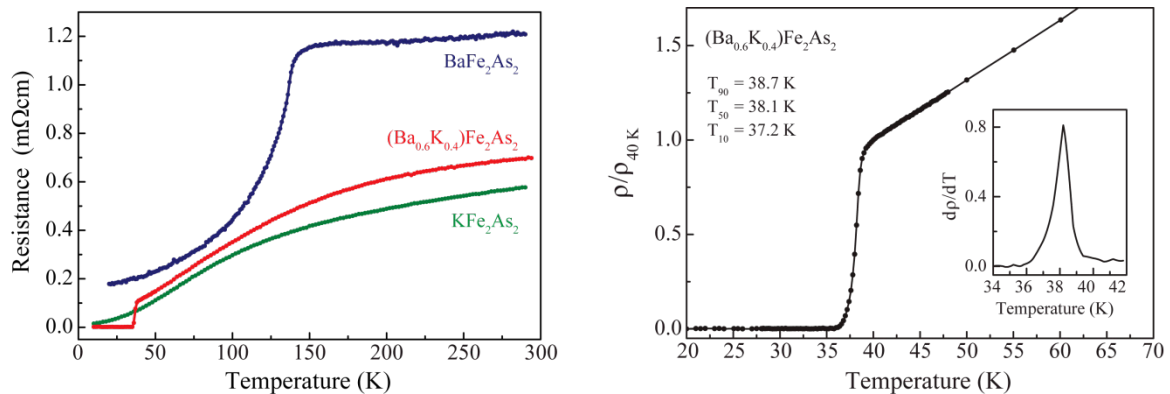


Figure 5.2: Left: Electrical resistance of BaFe₂As₂, KFe₂As₂ and (Ba_{0.6}K_{0.4})Fe₂As₂. Right: Resistivity transition of (Ba_{0.6}K_{0.4})Fe₂As₂.

5.4 Magnetic Investigations

In order to confirm superconductivity, magnetic investigations were performed using a SQUID magnetometer (MPMS-XL5, Quantum Design, Inc.). Zero-field cooled (shielding) and field cooled (Meissner) cycles measured at 1 and 0.5 mT are shown in Figure 5.3. The sample becomes diamagnetic at 38.3 K and shows 10 % of the maximum shielding at 37.2 K. The zero-field cooled branches of the susceptibilities measured at 1 and 0.5 mT are almost identical and amount to -0.94 at 1.8 K, which is close to ideal diamagnetism ($4\pi\chi = -1$). The Meissner effect depends on the applied field and the measured susceptibilities at 1.8 K are -0.64 at 0.5 mT and -0.3 at 1 mT. These values of the shielding and Meissner fractions should be considered as estimates due to uncertainties regarding the density of the compacted powder, demagnetization and flux pinning effects. However, the susceptibility data unambiguously prove bulk superconductivity of the $(\text{Ba}_{0.6}\text{K}_{0.4})\text{Fe}_2\text{As}_2$ sample.

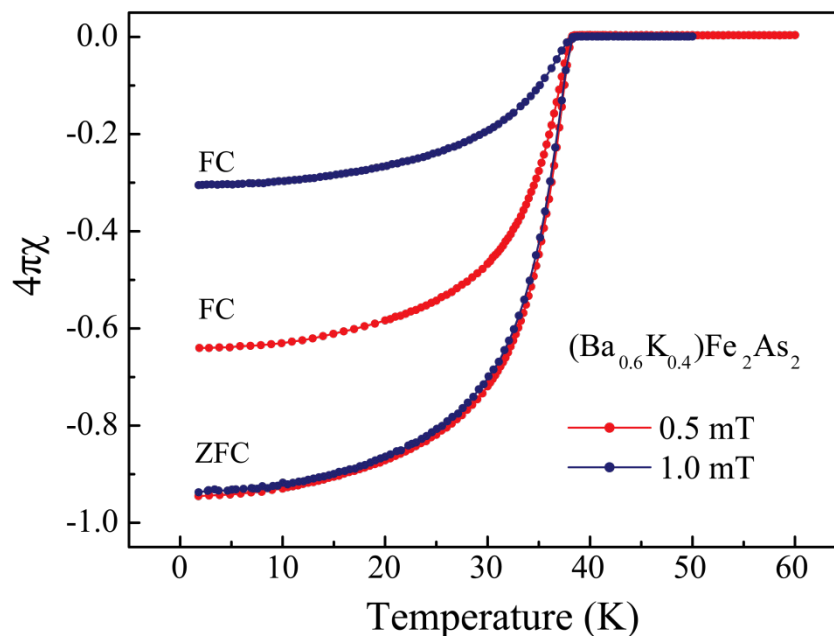


Figure 5.3: Magnetic susceptibility of the $(\text{Ba}_{0.6}\text{K}_{0.4})\text{Fe}_2\text{As}_2$ sample at 0.5 mT and 1 mT. FC is field cooled; ZFC is zero-field cooled.

6 $(\text{Ba}_{1-x}\text{K}_x)\text{Fe}_2\text{As}_2$ ($x = 0 - 1$)

The discovery of superconductivity in $(\text{Ba}_{0.6}\text{K}_{0.4})\text{Fe}_2\text{As}_2$ ^[80] was followed by reports on isotypic compounds with strontium ($T_C \approx 37$ K),^[81,82] calcium ($T_C \approx 20$ K),^[83] and europium ($T_C \approx 32$ K)^[84] within weeks. Since then, a large part of the research on superconducting iron arsenides has been focused on these ternary compounds rather than the arsenide oxides, because phase pure samples and also large single crystals are much easier to access. However, several investigations are focusing on the doping dependency of the structure and superconductivity on LaFeAsO-type compounds. In electron doped $RE\text{FeAsO}_{1-x}$ ($RE = \text{La} - \text{Sm}$),^[45] T_C increases with higher doping levels and with decreasing lattice parameters. On the other hand, the hole doped system $(\text{La}_{1-x}\text{Sr}_x)\text{FeAsO}$ ^[85] shows also increasing T_C with higher doping levels, but with increasing lattice parameters. This indicates that the doping level is the determining parameter for T_C in LaFeAsO compounds. However, these results are problematic about the fact, that the exact doping levels are unknown in most cases and the doping concentrations in these systems are limited to $x \approx 0.2$. Furthermore, the changes in the lattice parameters are very small and their significance is often doubtful.

So far, only the occurrence of superconductivity in $(\text{Ba}_{0.6}\text{K}_{0.4})\text{Fe}_2\text{As}_2$ was reported. The following chapter will provide an overview of the dependence of the occurrence of superconductivity, the transition temperature T_C and crystal structures on the potassium content in the solid solution $(\text{Ba}_{1-x}\text{K}_x)\text{Fe}_2\text{As}_2$ with $x = 0 - 1$.

6.1 Crystal Structures

The synthesis of the polycrystalline samples of $(\text{Ba}_{1-x}\text{K}_x)\text{Fe}_2\text{As}_2$ with $x = 0 - 1$ were performed by heating the elements as described in chapters 4 and 5. Crystal structures of the compounds $(\text{Ba}_{1-x}\text{K}_x)\text{Fe}_2\text{As}_2$ were determined by Rietveld refinements of X-ray powder patterns as shown exemplary in Figure 6.1.

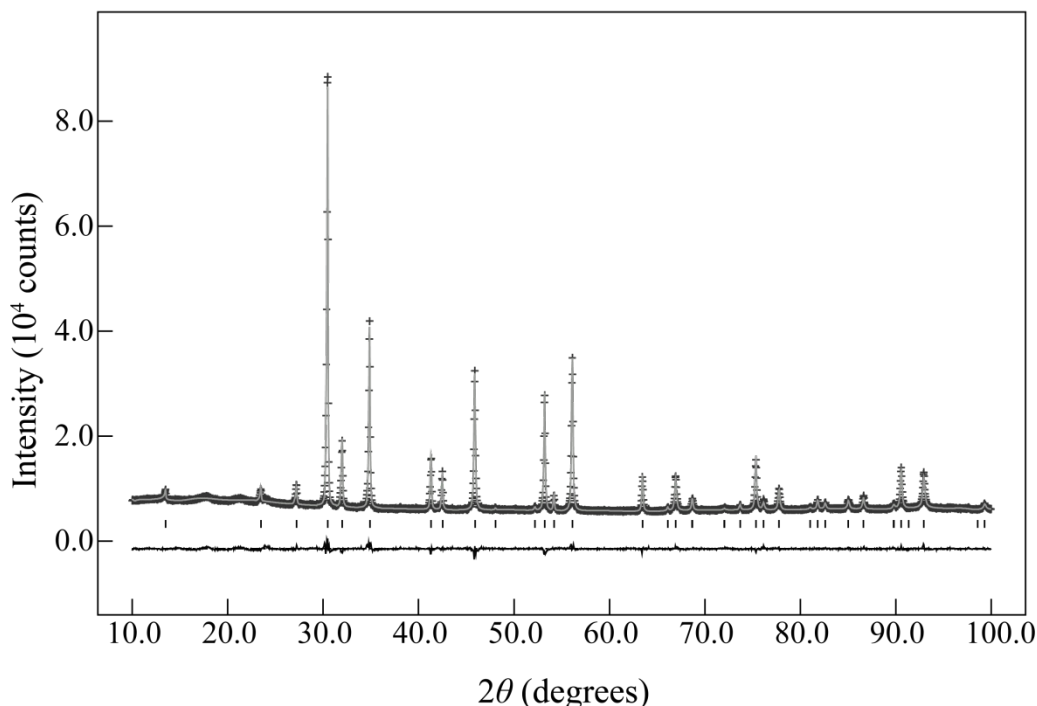


Figure 6.1: Measured (+) and calculated (–) X-ray powder pattern of $(\text{Ba}_{0.9}\text{K}_{0.1})\text{Fe}_2\text{As}_2$.

The X-ray powder diffraction patterns were recorded between 10 K and 300 K using a Huber G670 diffractometer equipped with a closed-cycle He-cryostat. Patterns at room temperature were indexed with tetragonal body-centered unit cells according to the ThCr_2Si_2 -type ($I4/mmm$) or with orthorhombic face-centered unit cells at low temperatures. Small amounts of FeAs were detected as impurity phase in some samples. The crystal structures were refined by the Rietveld method using the GSAS^[22] software package. All structure parameters determined by these Rietveld refinements were processed with ORIGIN.^[25]

Figure 6.2 shows the changes of the structure by doping. The lattice parameters a and c vary linearly with the potassium content over the whole range. The unit cell volume is constant within the experimental error, because the strong elongation of c is almost compensated by the decrease of a . Also the Fe–As and Ba(K)–As bond lengths remain unchanged. Both parameters vary by less than 0.4 % and are therefore not shown. Apart from the lattice parameters, only the Fe–Fe bond length and the As–Fe–As bond angle ε changes significantly (by 3 – 4 %) on doping.

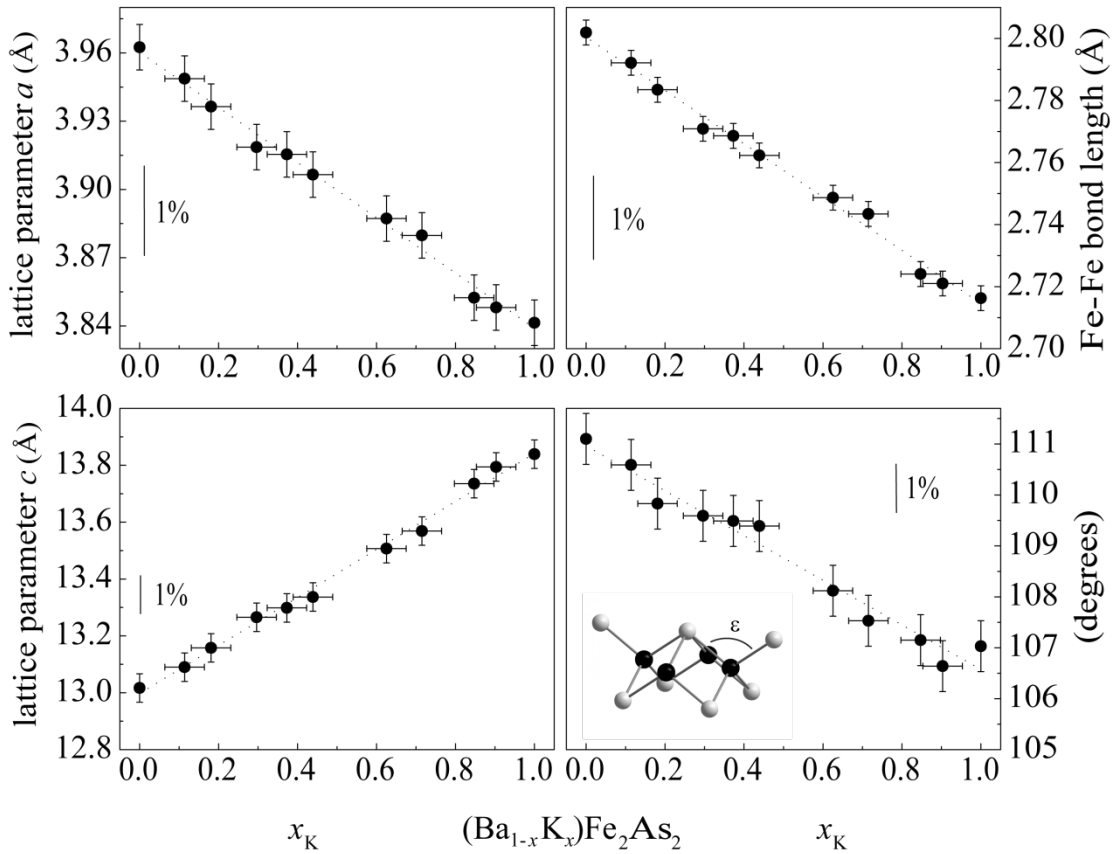


Figure 6.2: Variation of structural parameters in $(\text{Ba}_{1-x}\text{K}_x)\text{Fe}_2\text{As}_2$.

Both decrease linearly with increasing potassium content, which means that the FeAs_4 tetrahedra get more elongated along c and the iron atoms within the layers move together. Interestingly, ε becomes the ideal tetrahedral angle of 109.5° at

$x \approx 0.4$. The insert in Figure 6.2 depicts the ε angle in the FeAs layer. Thus, the main implication of doping on the crystal structure of (Ba_{1-x}K_x)Fe₂As₂ is a decreasing As–Fe–As bond angle and a shortening of the distances between the iron atoms at the same time.

Chemical bonding in ThCr₂Si₂-type compounds has been intensively studied.^[86] These results show that the properties of these compounds depend on a subtle balance between different bonding interactions, especially on the interplay between metal-ligand (Fe–As) and metal-metal (Fe–Fe) bonding within the layers.^[87] In the case of BaFe₂As₂, it is accepted that the Fe 3d_{x²-y²}-orbitals close the Fermi level play a key role for magnetism and superconductivity.

The angle ε determines the overlap between Fe 3d_{x²-y²} and As 3sp orbitals, thus these results suggest a strong coupling of structural and electronic degrees of freedom by doping.

It is disputed if the structural phase transition in the iron arsenides has to be completely suppressed before superconductivity emerges. Some results suggest that the structural distortion of LaFeAsO disappears by doping exactly at the border to the superconducting state.^[88] In the case of BaFe₂As₂, the tetragonal to orthorhombic phase transition is suppressed in (Ba_{0.6}K_{0.4})Fe₂As₂ as shown in chapter 5. In order to delimit the composition range of the transition, X-ray powder diffraction patterns of (Ba_{1-x}K_x)Fe₂As₂ with $x = 0 – 0.3$ have been measured between 300 K and 10 K. Figure 6.3 shows the temperature dependencies of the (110)-reflections. The reduction of the lattice symmetry is visible by peak splitting or broadening up to $x = 0.2$, but absent at $x = 0.3$. The transition temperatures (T_{tr}) decrease strongly with higher potassium content from 140 K to ≈ 90 K at $x = 0.2$, where the transition proceeds over a wide temperature range. These results indicate, that the orthorhombic phase (space group *Fmmm*) exists at low temperatures up to $x = 0.2$. At higher doping levels with $x > 0.2$ the lattice stays tetragonal even at low temperatures.

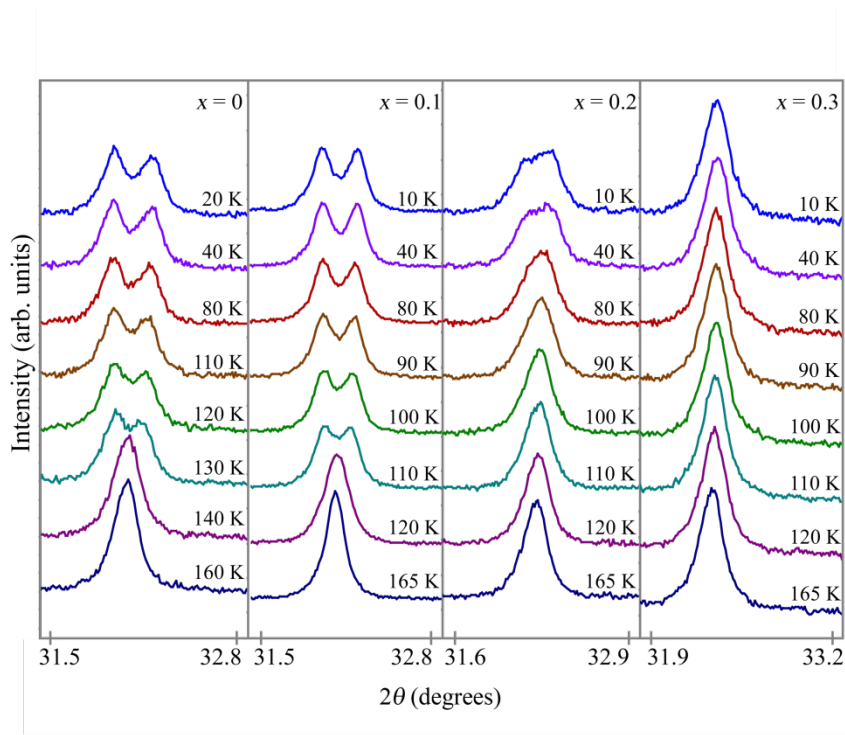


Figure 6.3: Temperature dependencies of the (110) reflection in $(\text{Ba}_{1-x}\text{K}_x)\text{Fe}_2\text{As}_2$ ($x = 0 - 0.3$).

6.2 Electrical Resistance Measurements

In order to investigate the doping effect on the superconducting transition temperatures electrical resistances were measured by the four probe method on cold pressed and sintered pellets using a He-closed-cycle refrigerator. The relative changes of the resistance with temperature ($R/R_{300\text{K}}$) of all samples are shown in Figure 6.4. Superconductivity was detected in all cases except for the undoped parent compound BaFe_2As_2 , but the transition temperatures vary strongly. BaFe_2As_2 is a poor metal with a specific resistivity around $1 \text{ m}\Omega\text{cm}$ at room temperature and exhibits the structural and magnetic phase transition at 140 K ,^[65] which is clearly visible in the resistance plot.

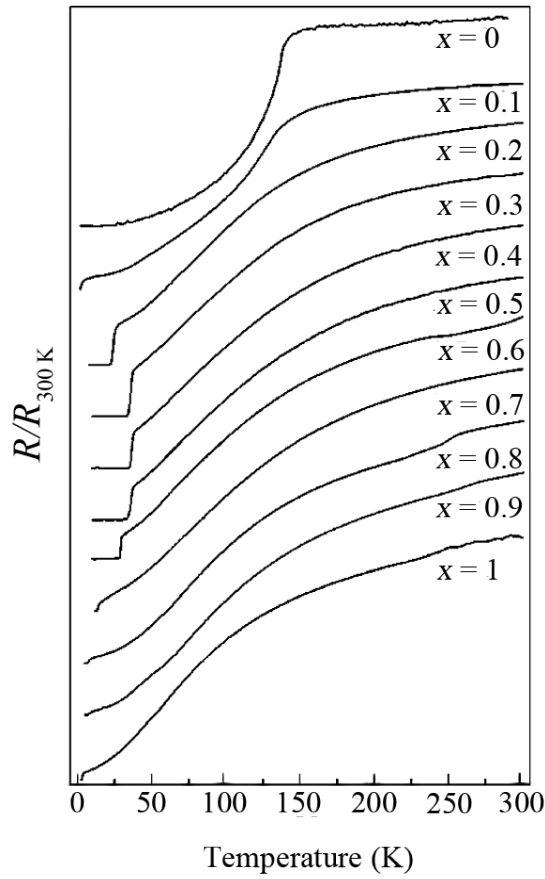


Figure 6.4: Relative electrical resistances of $(\text{Ba}_{1-x}\text{K}_x)\text{Fe}_2\text{As}_2$ samples (with $x = 0 - 1$).

At the smallest doping level of $x \approx 0.1$ the resistance anomaly is less pronounced but not completely suppressed. The resistance drops abruptly at ≈ 3 K, which is probably the onset of a superconducting transition. However, a zero resistance could not be achieved at 1.8 K, but superconductivity was proved by magnetic measurements. The anomaly in the resistance is completely suppressed when the doping level is at least 0.2. At this point, the compounds show the behavior of a normal metal and superconductivity at $T_C \approx 25$ K, which increases strongly to 36 K at $x = 0.3$ and to 38 K at $x = 0.4$. For doping levels higher than $x \approx 0.5$, T_C decreases continuously down to 3.8 K for KFe_2As_2 . Figure 6.5 shows the phase diagram of $(\text{Ba}_{1-x}\text{K}_x)\text{Fe}_2\text{As}_2$.

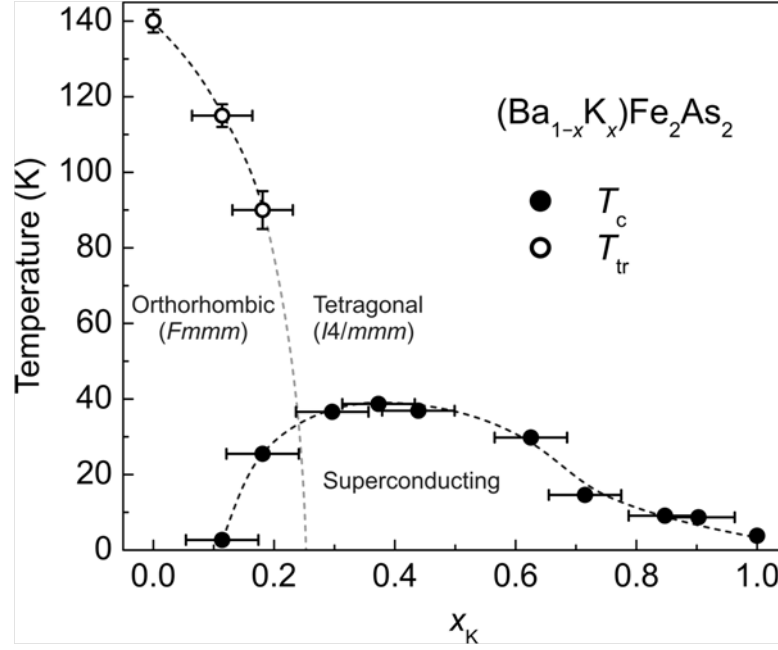


Figure 6.5: Phase diagram of $(\text{Ba}_{1-x}\text{K}_x)\text{Fe}_2\text{As}_2$ with the superconducting (T_c) and phase transition (T_{tr}) temperatures. T_c is defined as the temperature where the resistance is dropped to 90% of the extrapolated value. The dashed lines are guides for the eye.

6.3 Discussion

In this section the crystal structures and properties of the solid solution $(\text{Ba}_{1-x}\text{K}_x)\text{Fe}_2\text{As}_2$ were investigated. The substitution of barium for potassium in BaFe_2As_2 was considered to be a good approach to systematically oxidize the FeAs layers because of the very similar ionic radii of Ba^{2+} and K^+ (Ba^{2+} : 142 pm, K^+ : 151 pm).^[69] However, in spite of the much bigger difference in the ionic radii of Ba^{2+} and Na^+ (Ba^{2+} : 142 pm, Na^+ : 116 pm),^[69] Cortes-Gil *et al.*^[89] synthesized also $(\text{Ba}_{1-x}\text{Na}_x)\text{Fe}_2\text{As}_2$ over a wide doping range ($0 \leq x \leq 0.6$). Interestingly, the a lattice parameter decreases almost quantitatively similar to $(\text{Ba}_{1-x}\text{K}_x)\text{Fe}_2\text{As}_2$ with increasing doping concentrations. The c -axis increases with higher Na-content of the compound, which is also observed in $(\text{Ba}_{1-x}\text{K}_x)\text{Fe}_2\text{As}_2$. But in contrast to the K-doped compounds the increase in c in the mixed crystals of $(\text{Ba}_{1-x}\text{Na}_x)\text{Fe}_2\text{As}_2$

is less rapid and the c -axis begins to shrink again when the sodium concentration exceed $x = 0.5$. Therefore, the unit cell volume decreases overall by 4 % in (Ba_{1-x}Na_x)Fe₂As₂ whereas in (Ba_{1-x}K_x)Fe₂As₂ the cell volume is almost constant, because the shrinking of the a axis is compensated by the increasing c lattice parameter. In the solid solution (Ba_{1-x}K_x)Fe₂As₂, the main effect of doping on the crystal structure at room temperature is linear decreasing As–Fe–As bond angles ε and Fe–Fe distances. These structural changes are also found in the Na-doped compounds. Thus, the structural changes in the FeAs layers resulting from the decrease in electron counts by hole doping are obviously almost independent of the average radius of the alkaline metal cations.

Concerning the structural distortion at low temperatures, the tetragonal-to-orthorhombic phase transition ($I4/mmm \rightarrow Fmmm$) of potassium-doped BaFe₂As₂ occurs with decreasing transition temperatures up to a doping level of $x = 0.2$ and is completely suppressed at $x = 0.3$. Superconductivity emerges nearly over the whole doping range in (Ba_{1-x}K_x)Fe₂As₂ with a maximum T_C of 38 K at $x \approx 0.4$. Solely the parent compound BaFe₂As₂ is non-superconducting above 1.8 K. This suppression of the structural distortion is found for (Ba_{1-x}Na_x)Fe₂As₂ as well, which also shows its highest T_C of 34 K at $x \approx 0.4$, when the phase transition is completely suppressed. In this context, one of the most interesting facts among these mixed crystals is the underdoped region. Regarding the phase diagram of (Ba_{1-x}K_x)Fe₂As₂, there is an overlap of the superconducting dome with the orthorhombic distortion as the underdoped compounds (Ba_{0.9}K_{0.1})Fe₂As₂ ($T_C \approx 3$ K) and (Ba_{0.8}K_{0.2})Fe₂As₂ ($T_C \approx 25$ K) are distorted orthorhombically but also show superconducting transitions. This gives strong evidence for the co-existence of superconductivity with the structurally distorted and potentially magnetically ordered state in the BaFe₂As₂ family of iron arsenide superconductor.

7 Underdoped ($\text{Ba}_{1-x}\text{K}_x$) Fe_2As_2 ($x = 0 - 0.3$)

In both the LaFeAsO (1111) and BaFe_2As_2 (122) families, superconductivity evolves from poor metallic parent compounds with quasi two dimensional tetragonal crystal structures, which are subject to orthorhombic lattice distortions below certain temperatures T_o . Static long-range antiferromagnetic ordering emerges with Néel temperatures T_N well below T_o in LaFeAsO ,^[73] but very close to T_o in BaFe_2As_2 .^[65] The structural and magnetic transitions of the parent compounds are strongly affected by doping of the FeAs layers either with electrons or holes, and superconductivity appears at certain doping levels. For the underdoped phases in the transition zone several works have been published, presenting contradictory results concerning the presence of superconducting and antiferromagnetic ordered phases. Some results report on the phases to be separated and some other results indicate the co-existence of superconductivity and antiferromagnetism. The overlaps of the orthorhombic distortion with superconductivity and antiferromagnetic areas on the phase diagrams are still not clear, neither in the 1111 nor in the 122 systems.

The first phase diagram of $\text{LaFeAsO}_{1-x}\text{F}_x$, constructed by μSR data, showed a sharp-cut vertical border between the superconducting and the orthorhombic antiferromagnetic phases at $x = 0.045$.^[88] But neutron diffraction experiments showed, that although the magnetic ordering vanishes around $x \approx 0.04$, the orthorhombic lattice still exists at least to $x = 0.05$, where superconductivity has already emerged.^[90] This is in accordance with the neutron study of $\text{CeFeAsO}_{1-x}\text{F}_x$, where antiferromagnetic ordering disappears exactly before superconductivity emerges, but the orthorhombic lattice persists extensively into the superconducting dome up to $x \approx 0.1$.^[91] Similar results have been reported for $\text{SmFeAsO}_{1-x}\text{F}_x$ from μSR experiments^[92] and structural investigations using

synchrotron radiation.^[77] In the case of the 1111-family one can state at the moment, that static antiferromagnetic order is completely suppressed before superconductivity emerges, but the orthorhombic lattice co-exists with superconductivity and the temperature difference between T_o and T_N increases with the doping level.

This behavior of the 1111-superconductors is strongly reminiscent to the monolayer high- T_C cuprates. For instance in $\text{La}_{2-x}\text{Sr}_x\text{CuO}_4$, the antiferromagnetic order is well separated from the superconducting state, but the orthorhombic phase exists largely in the superconducting dome.^[93] In the 122-family, the co-existence of the orthorhombic structure with superconductivity has been shown in chapter 6 for $(\text{Ba}_{1-x}\text{K}_x)\text{Fe}_2\text{As}_2$ up to $x \approx 0.2$ ($T_C \approx 26$ K) using X-ray powder diffraction. Following neutron diffraction experiments performed by Chen *et al.*^[94] also showed orthorhombic symmetry and long-range AF ordering co-existing up to $x = 0.3$ ($T_C < 15$ K). The different shapes of the superconducting domes $T_C(x)$ of $(\text{Ba}_{1-x}\text{K}_x)\text{Fe}_2\text{As}_2$ may be due to different synthesis conditions. However, the potassium contents x in this thesis (chapter 6) were determined from X-ray data by Rietveld refinements, whereas only the nominal compositions are given by Chen *et al.*^[94] Since diffraction methods provide the mean structural information on a rather long spatial scale, short-range phase inhomogeneities are averaged. Thus one may understand the observed co-existence of superconductivity with antiferromagnetic ordering in $(\text{Ba}_{1-x}\text{K}_x)\text{Fe}_2\text{As}_2$ by phase-separation in magnetic non-superconducting and non-magnetic superconducting mesoscopic domains. Local probes like μSR and ^{57}Fe Mössbauer spectroscopy can provide more accurate information. Recently, three reports about μSR experiments, each conducted with almost optimally doped superconducting $(\text{Ba}_{1-x}\text{K}_x)\text{Fe}_2\text{As}_2$ single crystals, concluded consistently phase separations into superconducting and antiferromagnetic domains. The non-magnetic superconducting volume fractions were found to be $\approx 30\%$,^[95] 40% ,^[96] and 25% .^[97] However, the onsets of antiferromagnetic ordering in the

superconducting crystals were detected at $\approx 70 \text{ K} - 80 \text{ K}$ irrespective of different doping levels.

This chapter presents a detailed study of the structural and magnetic phase transitions of polycrystalline underdoped $(\text{Ba}_{1-x}\text{K}_x)\text{Fe}_2\text{As}_2$ ($x \leq 0.4$), where the samples were characterized by magnetic susceptibility and specific heat measurements. The crystal structures and chemical compositions were determined by Rietveld refinements of X-ray powder data. Detailed temperature-dependent ^{57}Fe -Mössbauer-spectroscopy was applied to detect the evolution of magnetic ordering on a local spatial scale.

7.1 Crystal Structures and Phase Transition

The underdoped compounds $(\text{Ba}_{1-x}\text{K}_x)\text{Fe}_2\text{As}_2$ ($x \leq 0.4$) were synthesized by heating the stoichiometric mixtures of the elements as described in sections 4 and 5. Phase purity was checked by X-ray powder diffraction using a Huber G670 Guinier imaging plate diffractometer equipped with a closed-cycle He-cryostat. Rietveld refinements of all diffractograms were performed with the TOPAS package.^[23] In order to obtain crystal structures inclusive of the Ba : K ratios, all profile contributions were refined freely, but in order to obtain accurate lattice parameter changes, all profile contributions were refined at room temperature and held constant for all other temperatures except for the lorentzian strain contribution. To verify the refined composition with regard to the Ba : K ratio, EDX and chemical analysis (ICP-AAS) were applied as well, which resulted within 5 % of the nominal and also the refined composition. Figure 7.1 shows the Rietveld fits of $(\text{Ba}_{1-x}\text{K}_x)\text{Fe}_2\text{As}_2$ ($x = 0.1 - 0.3$) at 300 K and the difference lines. Crystallographic data and selected bond lengths and angles at 300 K and 10 K, respectively, are listed in Table 7.1.

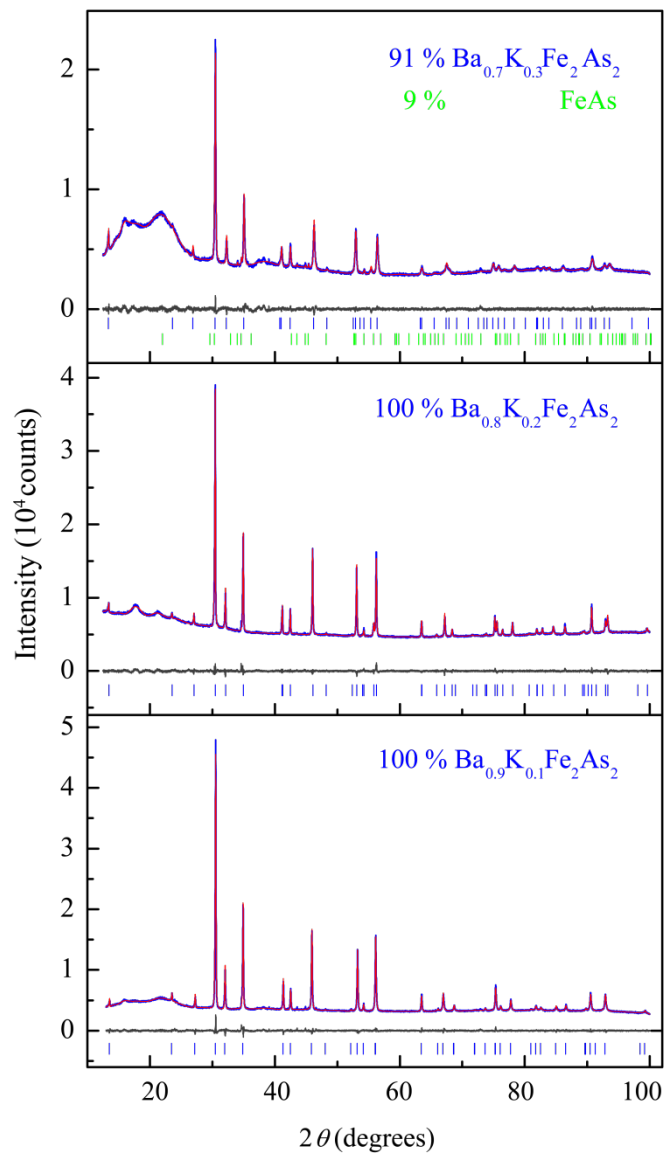


Figure 7.1: X-ray powder patterns of $(\text{Ba}_{1-x}\text{K}_x)\text{Fe}_2\text{As}_2$ ($x = 0.1 - 0.3$) with Rietveld profile fits and difference lines at 300 K.

Underdoped (Ba_{1-x}K_x)Fe₂As₂ ($x = 0 - 0.3$)

Table 7.1: Crystal structure data collected from Rietveld refinements of (Ba_{1-x}K_x)Fe₂As₂ at different temperatures.

(Ba _{1-x} K _x)Fe ₂ As ₂	$x = 0.1$		$x = 0.2$		$x = 0.3$
Temp. (K)	300	10	300	10	300
Space group	<i>I4/mmm</i>	<i>Fmmm</i>	<i>I4/mmm</i>	<i>Fmmm</i>	<i>I4/mmm</i>
<i>a</i> (pm)	395.37(1)	560.07(1)	393.95(1)	557.34(1)	392.57(1)
<i>b</i> (pm)	= <i>a</i>	556.20(1)	= <i>a</i>	554.64(1)	= <i>a</i>
<i>c</i> (pm)	1310.60(1)	1301.35(1)	1318.90(3)	1309.26(3)	1327.02(3)
<i>V</i> (nm ³)	0.20487(1)	0.40538(1)	0.20469(1)	0.40472(1)	0.20451(1)
<i>Z</i>	2	4	2	4	2
Data points	17401	17401	17401	17401	17501
Reflections	46	70	46	70	46
<i>d</i> range	1.012 – 6.553	1.006 – 6.507	1.009 – 6.595	1.005 – 6.546	1.007 – 6.635
<i>R</i> _p , <i>wR</i> _p	0.0153, 0.0211	0.0151, 0.0210	0.0158, 0.0217	0.0172, 0.0229	0.0146, 0.0192
<i>R</i> (<i>F</i> ²), χ^2	0.0121, 1.319	0.0132, 1.308	0.0123, 1.190	0.0117, 1.222	0.0076, 1.212
Ba, K	2 <i>a</i> (0,0,0) <i>U</i> _{iso} = 119(4)	4 <i>a</i> (0,0,0) <i>U</i> _{iso} = 45(4)	2 <i>a</i> (0,0,0) <i>U</i> _{iso} = 173(7)	4 <i>a</i> (0,0,0) <i>U</i> _{iso} = 117(8)	2 <i>a</i> (0,0,0) <i>U</i> _{iso} = 181(6)
Fe	4 <i>d</i> (½,0,¼) <i>U</i> _{iso} = 114(4)	8 <i>f</i> (¼,¼,¼) <i>U</i> _{iso} = 43(4)	4 <i>d</i> (½,0,¼) <i>U</i> _{iso} = 156(7)	8 <i>f</i> (¼,¼,¼) <i>U</i> _{iso} = 102(8)	4 <i>d</i> (½,0,¼) <i>U</i> _{iso} = 58(5)
As	4 <i>e</i> (0,0, <i>z</i>) <i>z</i> = 0.3547(1) <i>U</i> _{iso} = 147(4)	8 <i>i</i> (0,0, <i>z</i>) <i>z</i> = 0.3538(1) <i>U</i> _{iso} = 57(4)	4 <i>e</i> (0,0, <i>z</i>) <i>z</i> = 0.3545(1) <i>U</i> _{iso} = 129(7)	8 <i>i</i> (0,0, <i>z</i>) <i>z</i> = 0.3537(1) <i>U</i> _{iso} = 72(8)	4 <i>e</i> (0,0, <i>z</i>) <i>z</i> = 0.3545(1) <i>U</i> _{iso} = 79(5)
K : Ba ratio	14(1) : 86(1)	13(1) : 87(1)	20(1) : 80(1)	20(1) : 80(1)	24(1) : 76(1)
Lengths (pm)					
Ba–As	338.3(1) x 8	337.0(1) x 4 338.6(1) x 4	338.3(1) x 8	337.0(1) x 4 338.2(1) x 4	337.7(1) x 8
Fe–As	240.6(1) x 4	239.1(1) x 4	240.4(1) x 4	238.9(1) x 4	240.8(1) x 4
Fe–Fe	279.6(1) x 4	278.1(1) x 2 280.0(1) x 2	278.6(1) x 4	277.3(1) x 2 278.7(1) x 2	277.6(1) x 4
Angles (deg)					
As–Fe–As	110.5(1) x 2 109.0(1) x 4	111.2(1) x 2 108.9(1) x 2 108.3(1) x 2	110.1(1) x 2 109.2(1) x 4	110.7(1) x 2 109.0(1) x 2 108.6(1) x 2	109.2(1) x 2 109.6(1) x 4

These data are in line with the results described in chapter 6 where the lattice parameter a of the tetragonal phase decreases with the doping level x , while c increases. The temperature dependencies of the a and b lattice parameters are shown in Figure 7.2. For comparison, the lattice parameters of the tetragonal cells are multiplied by $\sqrt{2}$.

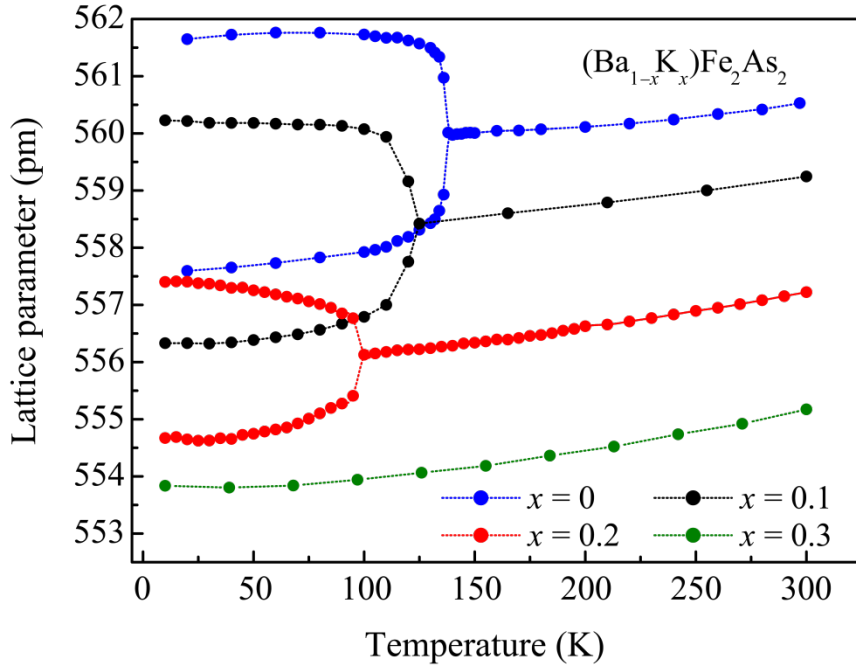


Figure 7.2: Lattice parameters of $(\text{Ba}_{1-x}\text{K}_x)\text{Fe}_2\text{As}_2$. The tetragonal parameters are multiplied by $\sqrt{2}$ for comparison.

The structural phase transition is strongly affected by the potassium content. The transition temperature decreases to ≈ 100 K at $x = 0.2$ and is no longer visible at $x = 0.3$. Also the magnitude of the distortion, expressed by the differences between the lattice parameters a and b at 10 K, decreases from 0.73 % ($x = 0$) to 0.70 % ($x = 0.1$) to 0.49 % ($x = 0.2$). Thus with increasing potassium doping levels, the structural transition of BaFe_2As_2 is shifted towards lower temperatures and also less pronounced. At a doping level of $x = 0.3$ the tetragonal-to-orthorhombic lattice distortion is no longer present.

7.2 Electric Resistivity

The *dc* resistivity of $(\text{Ba}_{1-x}\text{K}_x)\text{Fe}_2\text{As}_2$ is shown in Figure 7.3. At the lowest doping concentration ($x = 0.1$), the typical spin density wave anomaly is still visible but shifted towards lower temperatures and is also less pronounced than in undoped BaFe_2As_2 .^[65] At 3 K a drop of the resistance, associated with a superconducting transition is visible, even though zero resistance could not be reached at 1.8 K. The curve shape of the resistivity of $(\text{Ba}_{0.8}\text{K}_{0.2})\text{Fe}_2\text{As}_2$ still reminds of the SDW anomaly, but is smeared over a larger temperature range between ≈ 120 K and 70 K. The superconducting transition at 24 K is rather broad (≈ 4 K), but zero resistance is clearly observed at 23 K. At the higher doping level $x = 0.3$, the resistivity shows no more indications of the SDW anomaly and superconductivity emerges at $T_C = 33$ K.

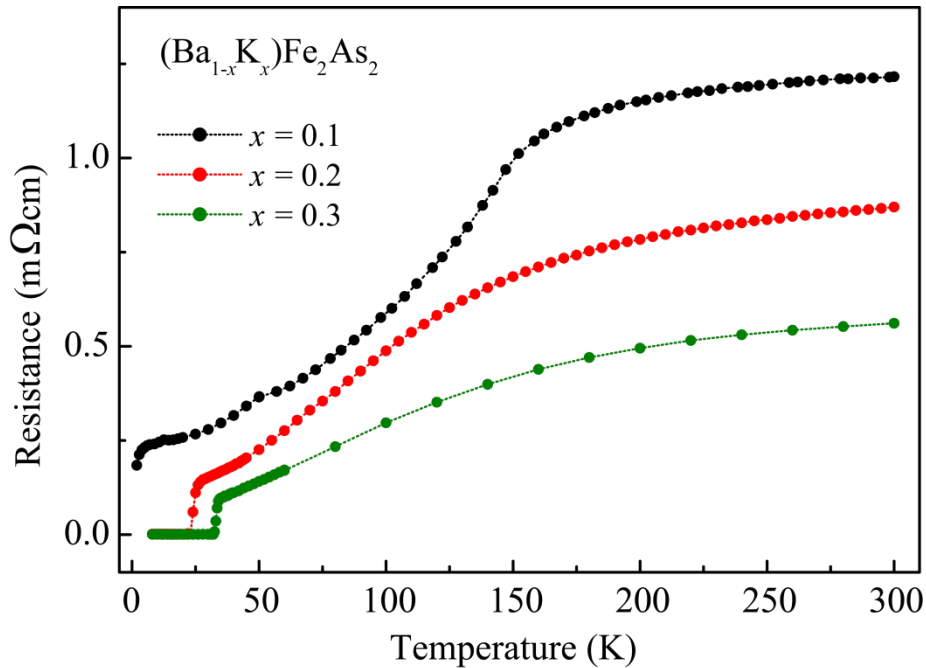


Figure 7.3: Temperature dependence of the *dc* resistivity of $(\text{Ba}_{1-x}\text{K}_x)\text{Fe}_2\text{As}_2$ ($x = 0.1, 0.2, 0.3$).

7.3 Magnetic Susceptibility

Magnetic properties were studied using a commercial SQUID magnetometer (Quantum Design MPMS-5) with external fields up to 50 kOe. The field-cooled (FC) and zero-field-cooled (ZFC) cycles of the static magnetic volume susceptibility are shown as a function of temperature in a magnetic field of 5 Oe in Figure 7.4. Estimating the superconducting volume fractions for $x = 0.2$ and $x = 0.4$ from the ZFC value at 1.8 K as 0.93 and 0.94, respectively, bulk superconductivity is evidently present. The FC values at 1.8 K amount to 1 % and 64 %, respectively. The corresponding temperatures, where 10 % of the maximum shielding is reached, are $T_C = 23.6$ K and 37.5 K for these two doping levels. These values of the shielding and Meissner fractions are only estimates due to uncertainties regarding the density of the compacted powder and demagnetization effects. However, for the sample with $x = 0.1$ bulk superconductivity cannot be established, but the sample becomes diamagnetic below 5 K in ZFC cycle as shown in Figure 7.4 (a). The positive contribution to the susceptibility may be due to ferromagnetic impurities.

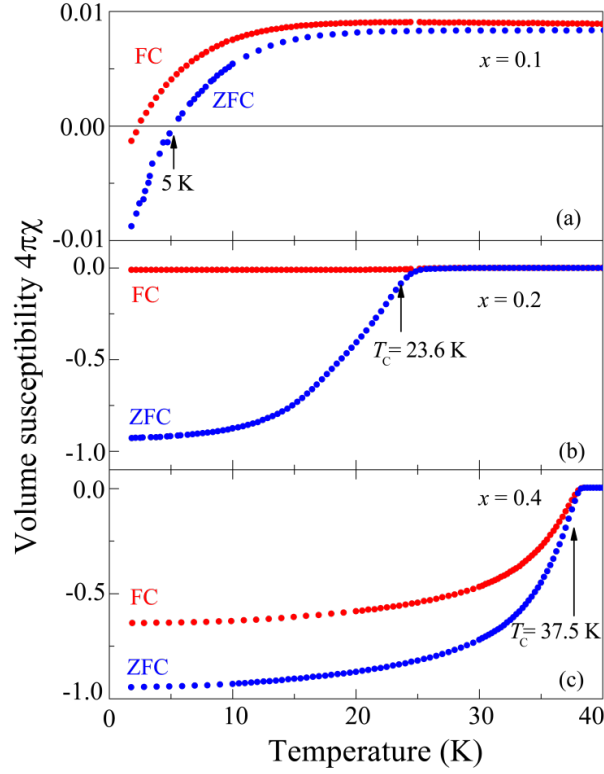


Figure 7.4: Static volume susceptibility $4\pi\chi = 4\pi M/H$ for $x = 0.1, 0.2$ and 0.4 in a magnetic field of 5 Oe for field-cooled (FC) and zero-field-cooled (ZFC) cycles.

7.4 Specific Heat

Specific heat was measured at the Universität Augsburg in the group of J. Deisenhofer in a Physical Properties Measurement System (PPMS, Quantum Design, Inc.) between 2 K and 300 K. Figure 7.5 shows the temperature dependence of the specific heat for the optimally doped sample with $x = 0.4$. In the inset C_p/T is plotted as a function of temperature for zero magnetic field and a field of 9 T. Both curves are on top of each other above and below the superconducting transition. To approximate the measured T_C of 37.3 K in zero field, an entropy conserving construction was used, as shown in the inset of Figure 7.5. The entropy conservation requires the triangular areas above and below measured traces being equal.^[98,99] The change of the specific heat at the transition is estimated as $\Delta C/T_c = 0.1 \text{ J/molK}$, which is in good agreement with

other reported values.^[100,101] The superconducting transition temperature T_C is shifted by only 1 K in a field of 9 T, reflecting the large upper critical fields which are estimated as 70 T or even higher.^[100,102,103] Concerning the coupling parameter $2\Delta_0/T_C$ of ($\text{Ba}_{0.6}\text{K}_{0.4}$) Fe_2As_2 a value of 4.14 was determined, which is enhanced compared to the BCS value of 3.53 signaling a stronger coupling.

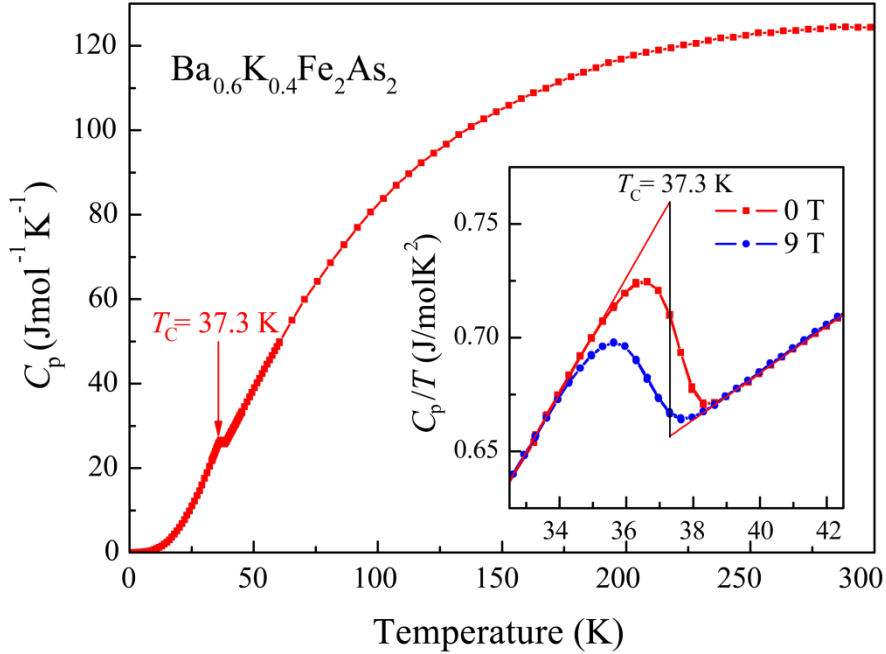


Figure 7.5: Specific heat of ($\text{Ba}_{0.6}\text{K}_{0.4}$) Fe_2As_2 . Inset: Comparison of C/T vs. temperature in magnetic fields of 0 T and 9 T. Lines are guide to the eyes.

The specific heat for the underdoped samples with $x = 0.1$ and $x = 0.2$ is plotted as a function of temperature in Figure 7.6. For $x = 0.1$ a broad peak with a maximum at $T_{\text{SDW}} = 132$ K is clearly visible, which is in agreement with the structural and magnetic transitions.

The low temperature C/T data for the sample with $x = 0.1$ reveals the onset of a phase transition at $T_{\text{ons}} = 4.4$ K (inset in Figure 7.6) which is completely suppressed in a magnetic field of 9 T. This temperature is in agreement with the appearance of diamagnetism as indicated in Figure 7.4 (a) and the appearance of

a resistivity drop and therefore can be ascribed to the onset of superconductivity. Hence, a superconducting and an antiferromagnetic transition are observable for $x = 0.1$, suggesting a strong competition for magnetic fluctuations and superconductivity. However, one must keep in mind that bulk superconductivity could not be established from susceptibility measurements and zero resistivity is not reached at 1.8 K.

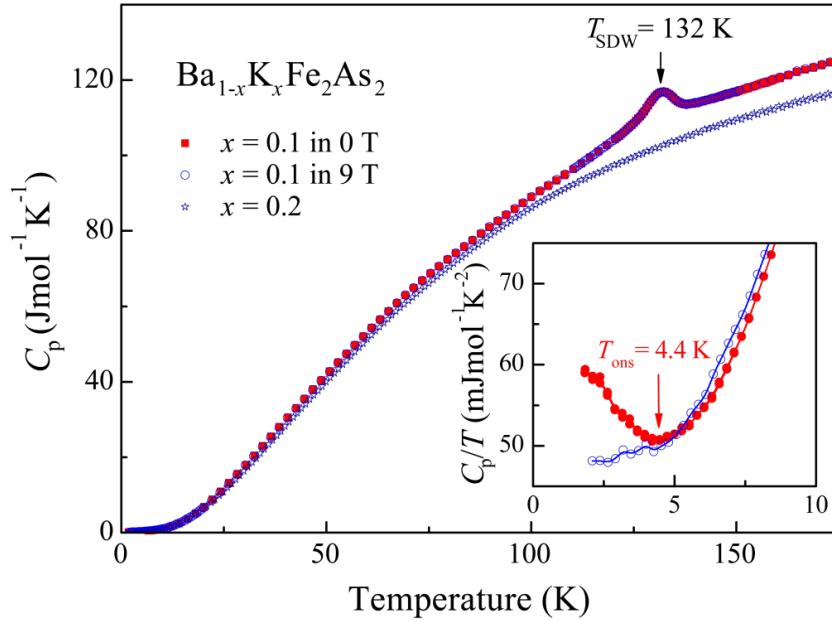


Figure 7.6: Comparison of C vs. T for $x = 0.1$ and $x = 0.2$. Inset: Comparison of C/T vs. temperature in magnetic fields of 0 T and 9 T for $x = 0.1$ to reveal the onset of superconducting transition and its suppression in a magnetic field of 9 T. Solid lines are guide to the eyes.

For the sample with $x = 0.2$ where bulk superconductivity below 23.6 K is proved by the susceptibility measurements (Figure 7.4 (b)), and the structural transition occurs at $T_0 = 105 \text{ K}$, no clearly visible anomaly in the specific heat is detectable, astonishingly. Figure 7.7 shows a comparison of C/T versus T for both concentrations, $x = 0.1$ and $x = 0.2$, respectively, and indicates the known transition for both compounds. At around $T_0 = 105 \text{ K}$, an extremely broadened transition region between about 80 K and 140 K may be visualized by guiding

Underdoped $(\text{Ba}_{1-x}\text{K}_x)\text{Fe}_2\text{As}_2$ ($x = 0 - 0.3$)

the eye with a linear extrapolation of the high-temperature behavior. A corresponding anomaly at the superconducting transition is not detectable in these data. The low temperature data for all three concentrations $x = 0.1$ (in 0 T and 9 T) and $x = 0.2, 0.4$ are plotted as C/T vs. T^2 . The data were fitted for $x = 0.1$ at 9 T and for $x = 0.2, 0.4$ in zero magnetic field with a linear behavior and the Sommerfeld coefficients γ and the Debye temperatures Θ_D extracted which are listed in Table 7.2.

Table 7.2: Sommerfeld coefficients γ and Debye temperatures Θ_D for $(\text{Ba}_{1-x}\text{K}_x)\text{Fe}_2\text{As}_2$ at different potassium concentrations ($x = 0.1, 0.2, 0.4$) extracted from the C/T vs. T^2 curve fits.

$(\text{Ba}_{1-x}\text{K}_x)\text{Fe}_2\text{As}_2$	γ (mJ/ (K ² mol))	Θ_D (K)
$x = 0.1$ @ 9 T	47	418
$x = 0.2$	5.6	238
$x = 0.4$	2.8	260

The values for γ and Θ_D for $x = 0.2$ and 0.4 are very close to each other and significantly lower than the values for $x = 0.1$. This reflects the superconducting low temperature state for $x = 0.2$ and 0.4 , which is fully suppressed at the doping level $x = 0.1$ in a magnetic field of 9 T. The values of $\gamma = 47$ mJ/ K² mol and $\Theta_D = 418$ K may contain a magnetic-field dependent contribution, because a linear fit (dashed line in the inset of Figure 7.7) of the data above 5 K in zero field yield somewhat lower values of $\gamma = 39$ mJ/ K² mol and $\Theta_D = 283$ K.

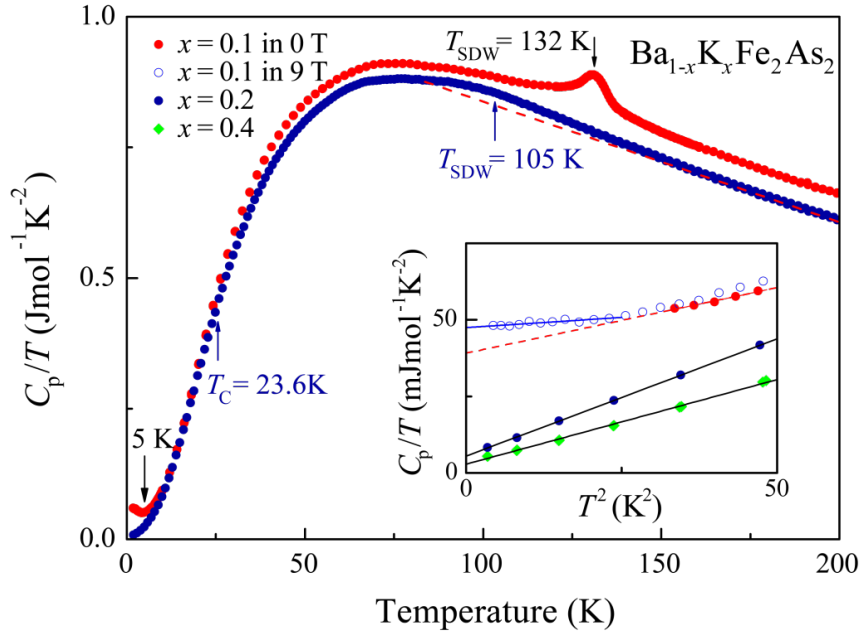


Figure 7.7: Comparison of C/T vs. T for $x = 0.1$ and $x = 0.2$. The dashed line is a guide for the eye. Inset: Comparison of C/T vs. T^2 for $x = 0.1$ (0 and 9 T) and $x = 0.2, 0.4$ at lowest temperatures. Solid and dashed lines are fits described in the text above.

Beside the results shown above, several specific heat studies of samples with a nominal composition near the optimal doping $x = 0.4$ have been reported^[70,100,101,104] and it turned out, that the major difficulties consist in modeling the normal state contribution to the specific heat. Hence, most studies have focused on the jump in C/T at the superconducting transition.^[70,100,104-106] Kant *et al.* from the Universität Augsburg modeled the normal state contribution of the specific heat to access the anomalies at the superconducting and magnetic phase transitions.^[107] Figure 7.8 shows the specific heat divided by the temperature C/T of the samples with $x \leq 0.2$. The anomalies caused by the SDW transitions can be clearly seen at 140 K and 134 K for the doping levels $x = 0$ and $x = 0.1$, respectively. As reported before, for ($\text{Ba}_{1-x}\text{K}_x$) Fe_2As_2 with $x = 0.2$ only an extremely broadened and weak feature at around 100 K can be presumed, although the tetragonal-to-orthorhombic structural phase transition was identified to occur in this temperature range.^[105] On the other hand, measurements of the

Underdoped ($\text{Ba}_{1-x}\text{K}_x$) Fe_2As_2 ($x = 0 - 0.3$)

susceptibility discussed in section 7.3 showed bulk superconductivity in this sample below 23 K, while no evident feature was discernible in C/T at this temperature (see Figure 7.7). To reveal the SDW and superconducting transition the specific heat of $(\text{Ba}_{0.7}\text{K}_{0.3})\text{Fe}_2\text{As}_2$ has been modeled at first like described by Kant *et al.*, because this compound doesn't show either a structural or a magnetic phase transition any more, as shown by X-ray diffraction methods earlier in this chapter. The parameters obtained for the $x = 0.3$ sample were slightly adapted to describe the specific heat in the tetragonal phase for the samples with lower potassium contents ($x \leq 0.2$). The resulting curves reproduce the data well in the tetragonal phase, as it can be seen from the solid lines at temperatures above the SDW transition temperature in Figure 7.8. For temperatures lower than T_{SDW} the data fits are illustrated as dashed lines.

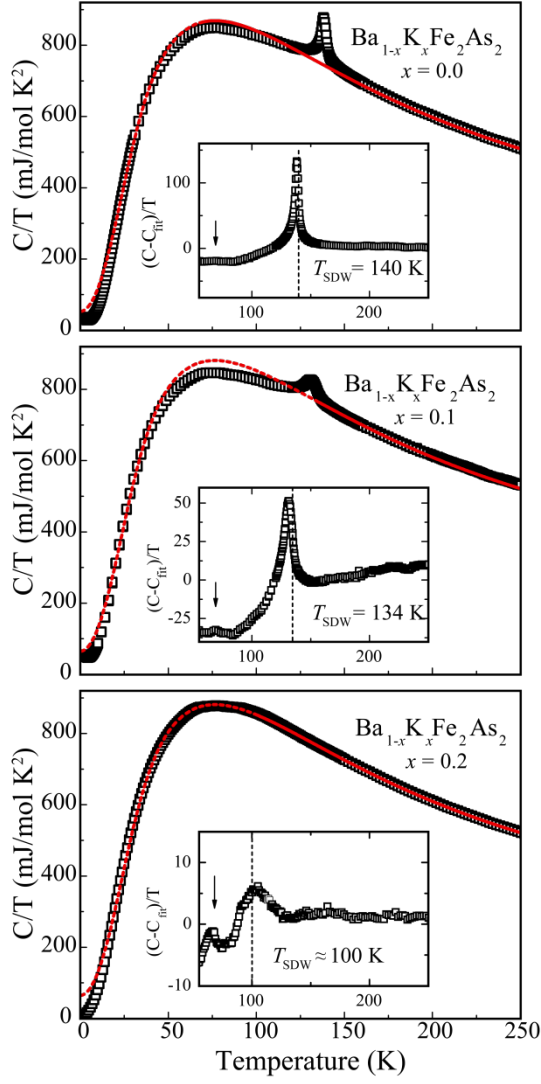


Figure 7.8: C/T vs. T for $(\text{Ba}_{1-x}\text{K}_x)\text{Fe}_2\text{As}_2$ ($x \leq 0.2$). The lines are fits to the data of the high temperature structure. Insets: Residual heat after subtracting the model from the experimental data. Arrows indicate contributions assigned to FeAs.^[107]

The modeled normal-state contribution $(C - C_{\text{fit}}) / T$ was then subtracted from the experimental data which is shown in the corresponding insets of Figure 7.8. Immediately, one recognizes the sharp SDW transitions at the appropriate temperatures for $x = 0.0$ and 0.1 . For $x = 0.2$ a strongly broadened anomaly of the specific heat data is now clearly visible at around 100 K and is in agreement with the observed anomalies in the electric resistance and the structural transition reported in chapter 7.1 and 7.2. The weak features visible at about 70 K present

in all three samples are probably traces of binary FeAs, which is reported to order helimagnetically in this temperature range.^[108]

Hence, the subtraction of the modeled normal-state contribution allows to reveal the SDW transition anomalies, but the validity of this model is naturally limited by the electronic reconstruction, the structural changes and the possible contributions of magnetic excitations occurring at the SDW transition. Therefore, Kant *et al.* chose another route to uncover the superconducting transition in $(\text{Ba}_{0.8}\text{K}_{0.2})\text{Fe}_2\text{As}_2$. They used the data for the undoped BaFe_2As_2 as a reference for a system with a SDW state but without superconductivity at low temperatures. Additionally, the normal-state parameters for both compounds are very similar. The low-temperature electronic specific heat is shown in Figure 7.9 where a clear anomaly with a midpoint of 22.9 K and a jump $\Delta C/T_C = 19.2 \text{ mJ}/\text{K}^2 \text{ mol}$ is in good agreement with the superconducting transition temperature determined from susceptibility measurements (see section 7.3).

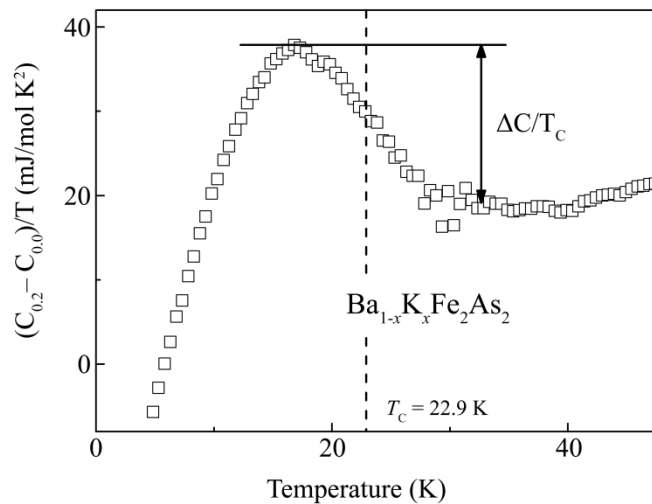


Figure 7.9: Difference of the specific heat for $x = 0.2$ and $x = 0$ divided by the temperature.^[107]

7.5 Mössbauer Spectroscopy

^{57}Fe Mössbauer spectroscopy is an excellent local probe for the determination of magnetic ordering in iron compounds. In comparison with other experimental methods, Mössbauer spectroscopic investigations on the new iron arsenide based superconductors are rather rare. In literature, Mössbauer studies on LaFePO ,^[109] REFeAsO ($\text{RE} = \text{La}, \text{Ce}, \text{Pr}, \text{Nd}$),^[58-61,110,111] SrFeAsF ,^[112] and AFe_2As_2 ($\text{A} = \text{Ba}, \text{Sr}, \text{Eu}$)^[65,113,114] have been already reported. Since the formation of binary iron phosphide or arsenide impurities can seriously affect the property measurements, ^{57}Fe Mössbauer spectroscopy can also be a useful analytical tool to detect iron impurity phases. The influence of Fe_2As , FeAs and FeAs_2 on the SDW transitions and the superconducting properties has systematically been studied.^[110]

For the ^{57}Fe Mössbauer spectroscopy investigations a $^{57}\text{Co}/\text{Rh}$ source was available at the Universität Münster in the group of Prof. Dr. Pöttgen. The samples were placed in a thin-walled PVC container at a thickness of about $10 \text{ mg Fe} / \text{cm}^2$. The measurements were performed in the usual transmission geometry in the temperature range between room temperature and 4.2 K. The source was kept at room temperature.

While the ^{57}Fe Mössbauer spectra of BaFe_2As_2 have been already discussed in chapter 4, this section deals with the Mössbauer data of the underdoped compounds of the solid solution $(\text{Ba}_{1-x}\text{K}_x)\text{Fe}_2\text{As}_2$ with $x = 0.1 - 0.4$ and KFe_2As_2 . The ^{57}Fe Mössbauer spectra of KFe_2As_2 is depicted in Figure 7.10 and shows a single absorption line with an isomer shift of $0.21 \text{ mm} / \text{s}$ from room temperature down to 4.2 K. A very small quadrupole splitting parameter of $-0.03 \text{ mm} / \text{s}$ was included into the fits at room temperature which increases to $-0.09 \text{ mm} / \text{s}$ at 4.2 K. As potassium transfers only one electron to the $[\text{Fe}_2\text{As}_2]$ layer, one expects a smaller electron density at the iron nuclei, which is consistent with the lower isomer shift of $0.21 \text{ mm} / \text{s}$ compared to the one of BaFe_2As_2 ($\delta = 0.31 \text{ mm} / \text{s}$ at

298 K) (see chapter 4). Thus, it is evident, that the doping with potassium affects the electronic situation of the iron atoms.

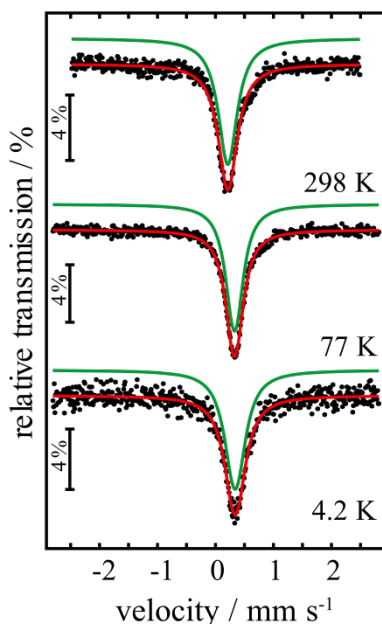


Figure 7.10: ^{57}Fe Mössbauer spectra of KFe_2As_2 .

The potassium-doped samples ($\text{Ba}_{1-x}\text{K}_x$) Fe_2As_2 with $x = 0.1$ and 0.2 show strikingly different temperature dependencies of the ^{57}Fe Mössbauer spectra, shown in Figure 7.11 and 7.12. In the temperature ranges 148 K – 136 K ($x = 0.1$) and 110 K – 96 K ($x = 0.2$), the spectra show temperature dependent superpositions of paramagnetic (green lines) and antiferromagnetically ordered domains (blue lines). However, with decreasing temperatures, the paramagnetic component rapidly diminishes within small temperature ranges, while the magnetically ordered fraction increases until the paramagnetic fractions are completely consumed. This may reflect a chemical inhomogeneity of the Ba / K distribution, where the un-split components represent domains with higher potassium contents and lower Néel temperatures and vice versa. Consistently, the smaller isomer shifts of the un-split signals indicate also higher potassium content. Thus, these findings indicate a certain distribution of potassium, but no distinct phase separation.

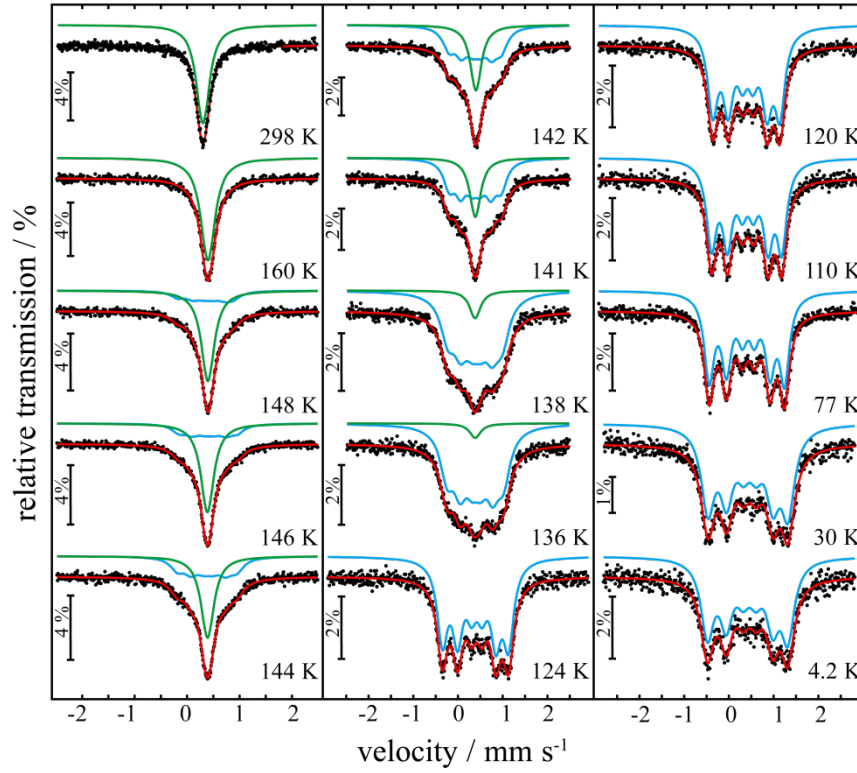


Figure 7.11: ^{57}Fe Mössbauer spectra of $(\text{Ba}_{0.9}\text{K}_{0.1})\text{Fe}_2\text{As}_2$.

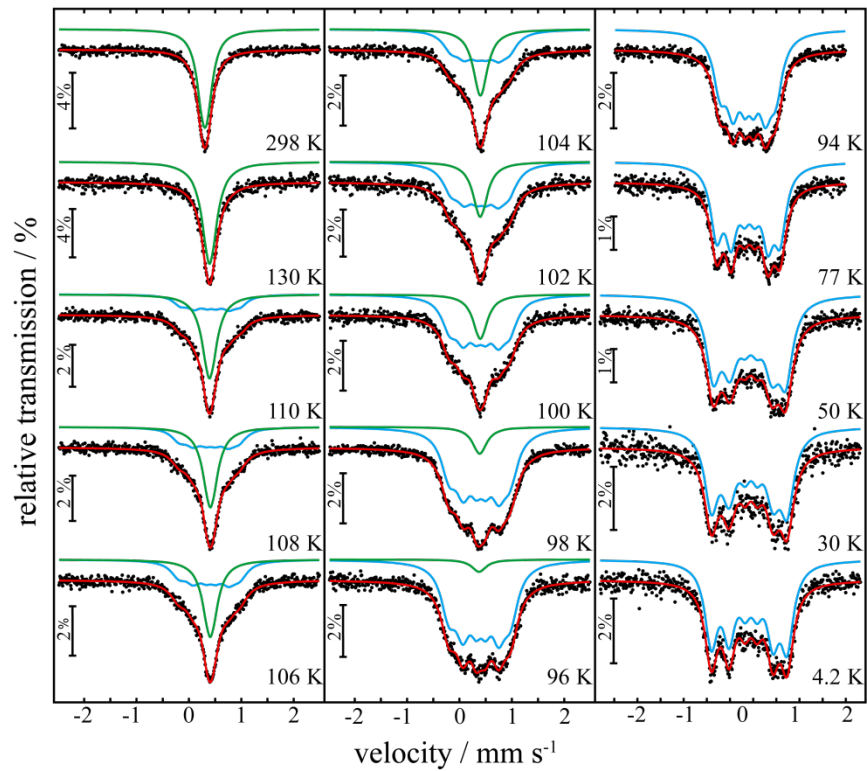


Figure 7.12: ^{57}Fe Mössbauer spectra of $(\text{Ba}_{0.8}\text{K}_{0.2})\text{Fe}_2\text{As}_2$.

Below 136 K and 96 K, respectively, the spectra of $(\text{Ba}_{0.9}\text{K}_{0.1})\text{Fe}_2\text{As}_2$ and $(\text{Ba}_{0.8}\text{K}_{0.2})\text{Fe}_2\text{As}_2$ can be well reproduced by one single magnetically split signal. The magnetic transition temperatures are very close to the structural transition temperatures extracted from the X-ray data. Similar to pure BaFe_2As_2 , the magnetic hyperfine fields increase with decreasing temperatures. BaFe_2As_2 and $(\text{Ba}_{0.9}\text{K}_{0.1})\text{Fe}_2\text{As}_2$ show almost similar hyperfine fields (5.47 T and 5.57 T at 4.2 K), whereas a decrease of B_{hf} to 5.07 T at 4.2 K in $(\text{Ba}_{0.8}\text{K}_{0.2})\text{Fe}_2\text{As}_2$ is observed. Since no non-magnetic fraction exists below ≈ 136 K and ≈ 96 K, respectively, these results strongly suggest the co-existence of superconductivity and antiferromagnetic ordering. A complete list of all fitting parameters of each Mössbauer spectrum is compiled in Table 11.1 in the appendix.

A further increase of doping again radically changes the ^{57}Fe Mössbauer spectra. Figure 7.13 shows the spectra of $(\text{Ba}_{0.7}\text{K}_{0.3})\text{Fe}_2\text{As}_2$ ($T_C = 33$ K) and $(\text{Ba}_{0.6}\text{K}_{0.4})\text{Fe}_2\text{As}_2$ ($T_C = 38$ K) recorded at 4.2 K together with the transmission integral fits. The fitting parameters are also listed in Table 11.2 in the appendix. In both cases only un-split absorption lines, which can be fitted by one component without any magnetic hyperfine field, are observed.

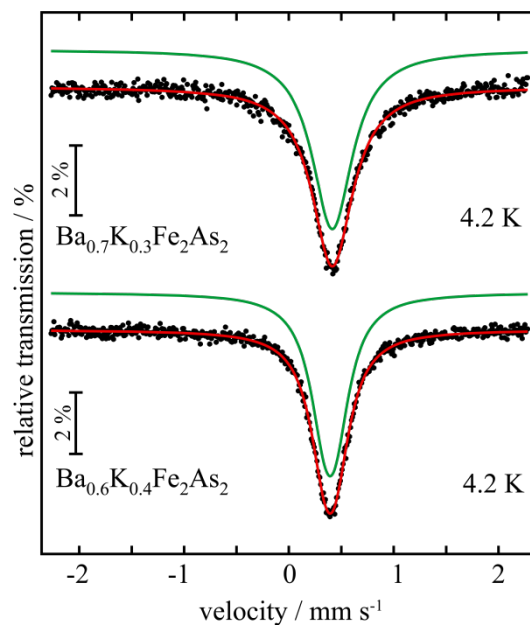


Figure 7.13: ^{57}Fe Mössbauer spectra of $(\text{Ba}_{0.7}\text{K}_{0.3})\text{Fe}_2\text{As}_2$ and $(\text{Ba}_{0.6}\text{K}_{0.4})\text{Fe}_2\text{As}_2$.

The line widths are slightly increased (0.47 mm / s and 0.35 mm / s, respectively) in comparison with undoped BaFe_2As_2 (0.25 mm / s), hinting at a small inhomogeneity of the Ba / K concentrations. Thus, in contrast to the completely magnetic ordered phase detected at $x = 0.2$, the phases with doping levels $x = 0.3$ and 0.4 are found to be completely non-magnetic at low temperatures. This is in line with the absence of lattice distortions, since both compounds keep the tetragonal structure at low temperatures (see Figure 7.2 and chapter 6).

7.6 Summary

The doping dependencies of the physical properties of the solid solution $(\text{Ba}_{1-x}\text{K}_x)\text{Fe}_2\text{As}_2$ in the underdoped region were presented in this section. The studies were based on a concerted approach using a broad spectrum of analytical techniques like X-ray analysis, magnetic investigations, electric resistivity measurements, specific heat and finally Mössbauer spectroscopy. The above results show clearly that the SDW anomaly connected with a structural phase transition is continuously suppressed by increasing doping concentrations and no longer observed in $(\text{Ba}_{0.7}\text{K}_{0.3})\text{Fe}_2\text{As}_2$. Specific heat measurements reveal a smearing of the phase transitions over larger temperature ranges in the underdoped samples, but no SDW anomaly in the optimally doped samples. This is in agreement with the structural data extracted from Rietveld refinements of the powder X-ray diffraction data. Bulk superconductivity was detected in all samples except $(\text{Ba}_{0.9}\text{K}_{0.1})\text{Fe}_2\text{As}_2$. ^{57}Fe Mössbauer spectra of the underdoped compounds $(\text{Ba}_{0.9}\text{K}_{0.1})\text{Fe}_2\text{As}_2$ and $(\text{Ba}_{0.8}\text{K}_{0.2})\text{Fe}_2\text{As}_2$ show only around T_{tr} temperature dependent superpositions of paramagnetic and antiferromagnetically ordered domains, which reflect only small inhomogeneities in the Ba / K distribution. Consequently, each domain shows slightly different Néel

temperatures. At lower temperatures, however, more domains get magnetically ordered until the paramagnetic fractions are completely consumed. Thus, no distinct phase separation is observed, but a certain small distribution of the potassium concentrations. No paramagnetic component is detectable in $(\text{Ba}_{0.8}\text{K}_{0.2})\text{Fe}_2\text{As}_2$ below T_C (24 K), suggesting the microscopic co-existence of superconductivity and antiferromagnetic ordering. Only at higher doping levels ($x \geq 0.3$), the magnetic and structural phase transitions are completely suppressed and superconductivity reaches the highest T_C . These results contradict reports on mesoscopic phase separations in antiferromagnetic ordered and non-magnetic superconducting regions in single crystals of almost optimally doped $(\text{Ba}_{1-x}\text{K}_x)\text{Fe}_2\text{As}_2$ ^[95-97] but coincide with reports on the co-existence of superconductivity and antiferromagnetic ordering in electron doped $\text{Ba}(\text{Fe}_{1-x}\text{Co}_x)_2\text{As}_2$.^[115,116] This co-existence is a very interesting phenomenon as superconductivity and magnetism were always considered as competing phenomena since a magnetic moment induces pair breaking and consequently should destroy superconductivity.

In the polycrystalline material studied in this work, the structural distortion and antiferromagnetic ordering are definitely absent at $x = 0.3$. The origin of magnetically ordered fractions detected in almost optimally doped single crystals of $(\text{Ba}_{0.6}\text{K}_{0.4})\text{Fe}_2\text{As}_2$ with high T_C , may either be attributed to a strongly inhomogeneous potassium distribution or caused by magnetic impurity phases like FeAs with a Néel temperature of 77 K.^[79] The potassium distribution is attributed to an uncontrolled single crystal growth with synthesis conditions, where mostly an excess of potassium is used and its incorporation is hardly controlled. During the single crystals grow, the potassium concentration is varying in the flux which consequently leads to an inhomogeneous potassium concentration in the single crystals.

8 Isoelectronic Doping of BaFe₂As₂

The discovery of superconductivity in the iron arsenide compounds has attracted an enormous interest world wide. Especially in the field of 122 compounds, great efforts were made to raise T_C to temperatures higher than 38 K as detected in (Ba_{0.6}K_{0.4})Fe₂As₂.^[80] Since superconductivity induced by hole doping was discovered in (Ba_{1-x}K_x)Fe₂As₂^[80,117] reports on analogous compounds like for instance (Sr_{1-x}K_x)Fe₂As₂ ($T_C = 37$ K),^[82] (Ca_{1-x}Na_x)Fe₂As₂ ($T_C = 20$ K),^[83] and (Eu_{1-x}K_x)Fe₂As₂ ($T_C = 32$ K)^[84] followed quickly. Apart from that, even electron doping like in Ba(Fe_{1-x}Co_x)₂As₂^[118] or (Sr_{1-x}La_x)Fe₂As₂^[119] lead to T_C 's up to 22 K ($x = 0.06 - 0.08$ or $x = 0.4$, respectively). Thus, superconductivity which emerges during the antiferromagnetic ordering gets suppressed, can be achieved by hole- or electron-doping. Another pathway to suppress the spin density wave is to apply external pressure to the 122 compounds BaFe₂As₂ and SrFe₂As₂.^[120] Also CaFe₂As₂ was reported to show pressure induced superconductivity at first, but these reports were contradicted later^[121] as CaFe₂As₂ gets compressed to a three-dimensional structure with As-As bonds, the so-called "collapsed phase".^[122] This structural phase transition is well known from other ThCr₂Si₂-type compounds such as SrRh₂P₂.^[123] In BaFe₂As₂, however, the FeAs layers remain two-dimensional under pressure and superconductivity appears below 31 K at 5.5 GPa.^[124] The superconducting transition and the change of structural features were intensively studied by Kimber *et al.*^[124] They reported on similarities between the structural distortion under pressure and chemical doping in BaFe₂As₂. Compared to the chemically substituted compounds of (Ba_{1-x}K_x)Fe₂As₂, the high pressure BaFe₂As₂ shows the same behavior concerning the suppression of the tetragonal-to-orthorhombic phase transition, the reduction of the As-Fe-As bond angle and the Fe-Fe distance. As the key

structural features in BaFe₂As₂ under pressure show exactly the same dependence on approaching optimal T_C as reached by chemical substitution with potassium, Kimber *et al.* suggested that the effect of structural distortions caused by a simple volume reduction is more important than charge doping for inducing superconductivity in BaFe₂As₂.^[124] If this is the case, a substitution of the Ba²⁺ for, e.g., the smaller Sr²⁺ cation should lead to a volume reduction as well and consequently induce superconductivity. As both ternary phases are known to exist^[65,125] and both cations provide similar ionic radii (Ba²⁺: 142 pm, Sr²⁺: 125 pm)^[69] the substitution of barium for strontium is a promising approach to apply “chemical pressure” on BaFe₂As₂. Another pathway to shrink the cell volume of BaFe₂As₂ could be the substitution of As for P, as phosphorus doping of the arsenic site was already successful performed in EuFe₂(As_{0.7}P_{0.3})₂.^[126] The following chapter presents those two different approaches of inducing superconductivity by “chemical pressure” realized by isoelectronic doping in BaFe₂As₂.

8.1 (Ba_{1-x}Sr_x)Fe₂As₂

8.1.1 Synthesis

Polycrystalline samples of the composition $EAFe_2As_2$ ($EA = Ba, Sr$ in variable ratios) were synthesized by heating the distilled alkaline earth metals, iron powder and arsenic lump at a ratio of 1.05 : 2 : 2. The element mixtures were transferred in alumina crucibles and enclosed in silica tubes under argon atmosphere. The samples were slowly heated (50 K / h) to 873 K, kept at this temperature for 10 hours and heated again to 1123 K at a rate of 50 K / h. After keeping the samples at this temperature for another 15 hours they were cooled down to room temperature by shutting down the furnace. The reaction products were homogenized in the crucibles in a glove-box and annealed at 1173 K for 25 hours. After cooling down to room temperature the powders were thoroughly

ground in an agate mortar and annealed another two to three times at 1173 K for 15 hours – 30 hours. After each annealing step, powder diffractograms were recorded to control the reaction progress. If the reflections showed still shoulders after the third annealing procedure, pellets were pressed and annealed again. The obtained products were black metallic powders which are air sensitive and therefore handled under argon atmosphere.

8.1.2 Characterization

The crystal structures were determined by X-ray powder diffraction using a Huber G670 Guinier imaging plate diffractometer. Rietveld refinements of all diffractograms were performed with the TOPAS package.^[23] The atom positions of BaFe₂As₂ (see chapter 4) were used as starting parameters for the refinement. As Ba and Sr occupy both the $2a$ (0,0,0) position, the isotropic displacement parameters of both atoms were constraint as well. The occupation parameters of Ba and Sr were constraint to unity.

Figure 8.1 shows exemplary the Rietveld refinement of (Ba_{0.5}Sr_{0.5})Fe₂As₂. The crystallographic data of this refinement are given in Table 8.1.

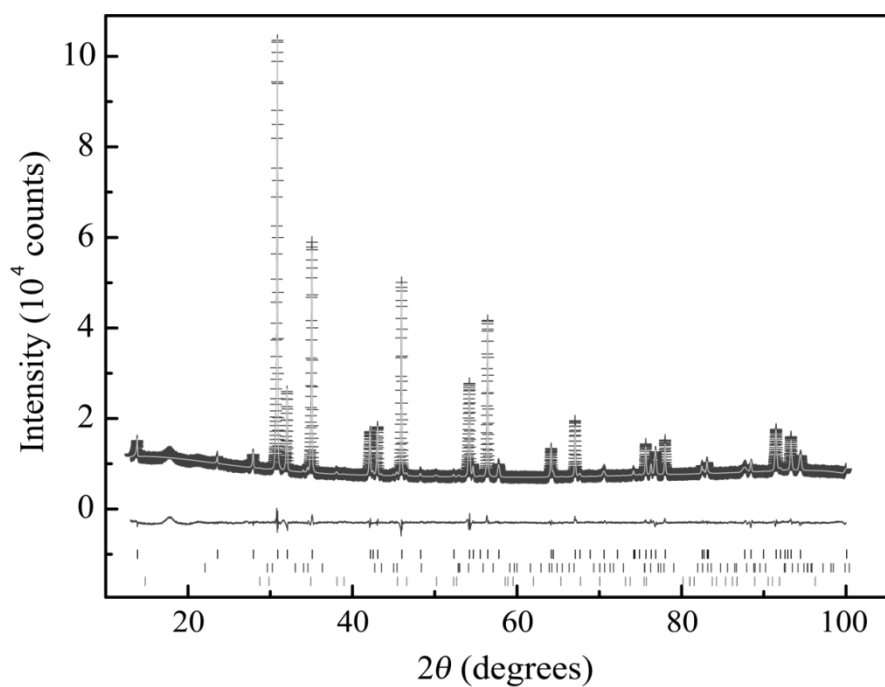


Figure 8.1: Measured (+) and calculated (-) X-ray powder pattern of $(\text{Ba}_{0.5}\text{Sr}_{0.5})\text{Fe}_2\text{As}_2$. Reflection markers are black (upper row) for the nominal composition $(\text{Ba}_{0.5}\text{Sr}_{0.5})\text{Fe}_2\text{As}_2$, dark grey (middle row) for FeAs (7.72 wt %) and grey (lower row) for Fe_2As (8.58 wt %).

Table 8.1: Crystallographic data of the Rietveld refinement of Ba_{0.5}Sr_{0.5}Fe₂As₂.

Diffractometer	Huber G670
Radiation	Cu-K _{α1}
Space group	<i>I4/mmm</i>
<i>a</i> (pm)	394.28(1)
<i>b</i> (pm)	= <i>a</i>
<i>c</i> (pm)	1274.96(1)
<i>V</i> (nm ³)	0.19820(1)
<i>Z</i>	2
Data points	8700
Reflections	45
<i>d</i> range	1.005-6.375
<i>R</i> _P , <i>wR</i> _P	0.0150, 0.0209
<i>R</i> _{bragg} , χ^2	0.018, 1.961
Atomic parameters	
Ba, Sr	2 <i>a</i> (0,0,0) <i>U</i> _{iso} = 148(4)
Fe	4 <i>d</i> (½,0,¼) <i>U</i> _{iso} = 107(4)
As	4 <i>e</i> (0,0, <i>z</i>) <i>z</i> = 0.3569(1) <i>U</i> _{iso} = 135(4)
Ba : Sr ratio	55(1) : 45(1)
Bond lengths (pm)	
Ba–As	333.1(1) x 8
Fe–As	239.7(1) x 4
Fe–Fe	278.8(1) x 4
Bond angles (deg)	
As–Fe–As	110.7(1) x 2 108.9(1) x 4

On the basis of this diffractogram the main issue of preparing mixed crystals of (Ba_{1-x}Sr_x)Fe₂As₂ is obvious: Indeed the synthesis of (Ba_{1-x}Sr_x)Fe₂As₂ ($x = 0 - 1$) is successful under the conditions described above, but with small amounts of impurity phases. Either the FWHM of the reflections were strongly broadened, indicating a highly inhomogeneous Ba / Sr distribution, or impurity phases of FeAs, Fe₂As or FeAs₂ were detected. This work was focused on synthesizing mixed crystals of (Ba_{1-x}Sr_x)Fe₂As₂ of which the distribution of the alkaline earth metals are as homogeneous as possible to obtain the most accurate structural information. Consequently, the samples were repeatedly annealed like described above until the powder diffractogram showed sharp reflections, even if higher contents of impurity phases were detected afterwards. However, elevating the temperature above 1273 K led to a continuous decomposition of the samples into the binary iron arsenides.

In order to verify the composition refined by the Rietveld method EDX measurements were performed. The Ba : Sr ratios determined by the EDX measurements resulted in the refined composition within 5% for the Ba : Sr ratio and therefore confirmed the composition within the experimental error.

(Ba_{0.5}Sr_{0.5})Fe₂As₂ crystallizes isostructural to BaFe₂As₂ in the tetragonal space group *I4/mmm*. The lattice parameter *a* is 394.28 pm and therefore only slightly shorter than 396.25 pm found for BaFe₂As₂. The *c*-lattice parameter shortens from 1301.68 pm to 1274.96 pm. Thus, the unit cell is primarily vertically compressed through the substitution of barium for the smaller strontium. The FeAs₄ tetrahedra, however, get slightly elongated along the *c*-axis and the iron atoms within the layers move together (278.8 pm in comparison to 280.2 pm in BaFe₂As₂). Although less pronounced, the decreasing As–Fe–As bond angles and the shrinking Fe–Fe atomic distances show the same tendency as in the potassium doped compounds of (Ba_{1-x}K_x)Fe₂As₂ (see chapter 6).

While the parent compound BaFe₂As₂ shows a structural and magnetic phase transition below 140 K these phase transitions are suppressed in hole doped

superconducting compounds such as $(\text{Ba}_{0.6}\text{K}_{0.4})\text{Fe}_2\text{As}_2$. Hence, the suppression of the SDW anomaly seems to be a key feature for the occurrence of superconductivity. For investigations concerning the structural transition, temperature dependent X-ray powder patterns of $(\text{Ba}_{0.5}\text{Sr}_{0.5})\text{Fe}_2\text{As}_2$ were recorded using a Huber G670 diffractometer equipped with a closed-cycle He-cryostat. Figure 8.2 shows the (110) reflection of the powder patterns at different temperatures. Below 170 K the reflection broadens and splits clearly at lower temperatures as the tetragonal phase undergoes a distortion to the orthorhombic phase. Thus, one would not expect to detect superconductivity in the strontium-doped compound $(\text{Ba}_{0.5}\text{Sr}_{0.5})\text{Fe}_2\text{As}_2$. To confirm this assumption electric resistance measurements were performed. The results are presented in the next section.

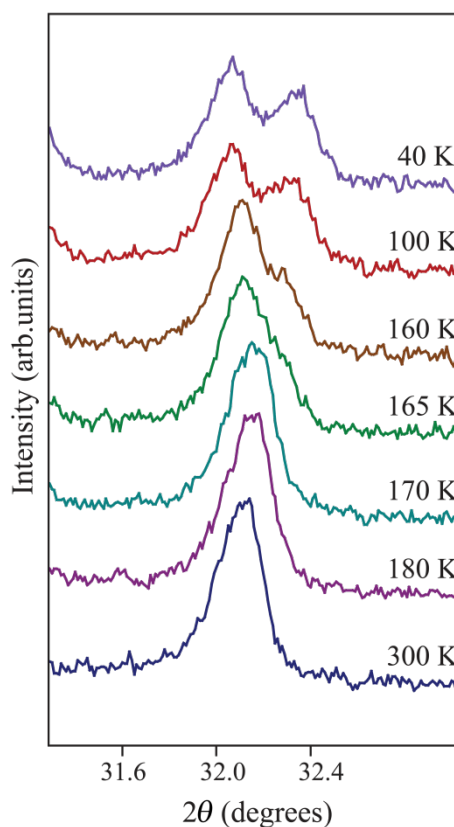


Figure 8.2: Temperature dependency of the (110) reflection of $(\text{Ba}_{0.5}\text{Sr}_{0.5})\text{Fe}_2\text{As}_2$.

8.1.3 Electrical Resistance of $(\text{Ba}_{0.5}\text{Sr}_{0.5})\text{Fe}_2\text{As}_2$

For electrical resistance measurements the samples were cold pressed into pellets ($\text{Ø} = 0.6$ mm, thickness ~ 1 mm) and sintered at 1173 K for 20 hours. The pellets were fixed on a brass sample carrier using an epoxy resin. In order to minimize contact with air while the resin hardened the sample holder was put under an argon shower. Afterwards the copper wires were fixed to the surface of the sample by silver conduction paint under a nitrogen shower. The recorded temperature dependent *dc* resistivity of $(\text{Ba}_{0.5}\text{Sr}_{0.5})\text{Fe}_2\text{As}_2$ between 10 K and 300 K is shown in Figure 8.3.

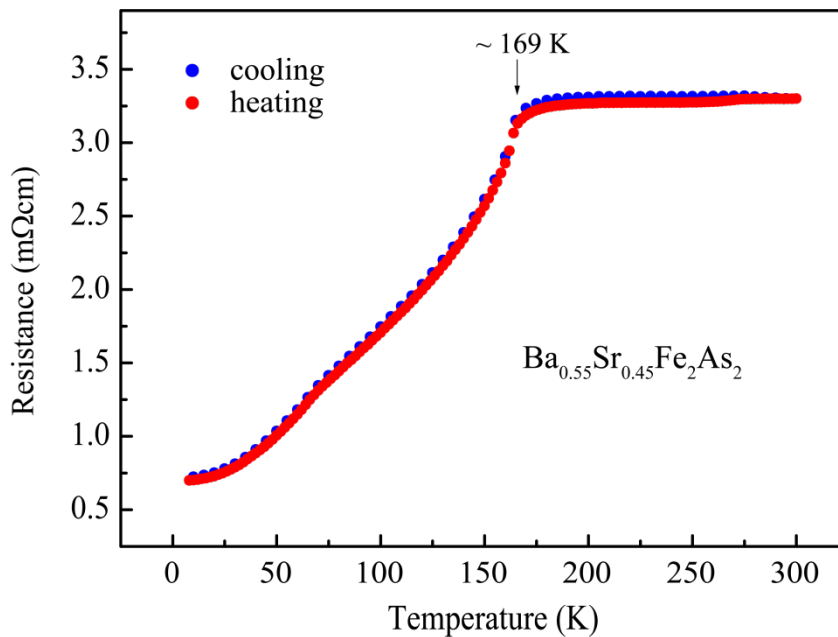


Figure 8.3: *dc* resistivity of $(\text{Ba}_{0.5}\text{Sr}_{0.5})\text{Fe}_2\text{As}_2$.

$(\text{Ba}_{0.5}\text{Sr}_{0.5})\text{Fe}_2\text{As}_2$ is a poor metal with a specific electrical resistance of $3.3 \cdot 10^{-5} \Omega\text{m}$ ($1 \cdot 10^{-5} \Omega\text{m}$ in BaFe_2As_2) and shows an anomaly like BaFe_2As_2 (see chapter 4). Solely the resistivity drop is shifted from 140 K (BaFe_2As_2) to approximately 169 K but the resistance decreases very similar to the undoped 122 compound. At 10 K the electrical resistance amounts to $0.7 \cdot 10^{-5} \Omega\text{m}$

according to a relative resistance ratio (RRR) of 4.7. In contrast to BaFe_2As_2 a small hump at about 70 K to 80 K is visible. This is attributed to the FeAs impurity ($\sim 8\%$) which is reported to order helimagnetically in this temperature range.^[108] The resistivity drop at ~ 169 K is in accordance with the results of the X-ray powder diffraction discussed above.

8.1.4 Properties of $(\text{Ba}_{1-x}\text{Sr}_x)\text{Fe}_2\text{As}_2$ ($x = 0 - 1$)

Powder samples of the solid solution $(\text{Ba}_{1-x}\text{Sr}_x)\text{Fe}_2\text{As}_2$ with $x = 0 - 1$ were treated in the same manner as exemplary shown above for $(\text{Ba}_{0.5}\text{Sr}_{0.5})\text{Fe}_2\text{As}_2$. All data of the Rietveld refinements were collected and afterwards processed with ORIGIN.^[25] Figure 8.4 shows the changes of the structure depending on the Sr-content.

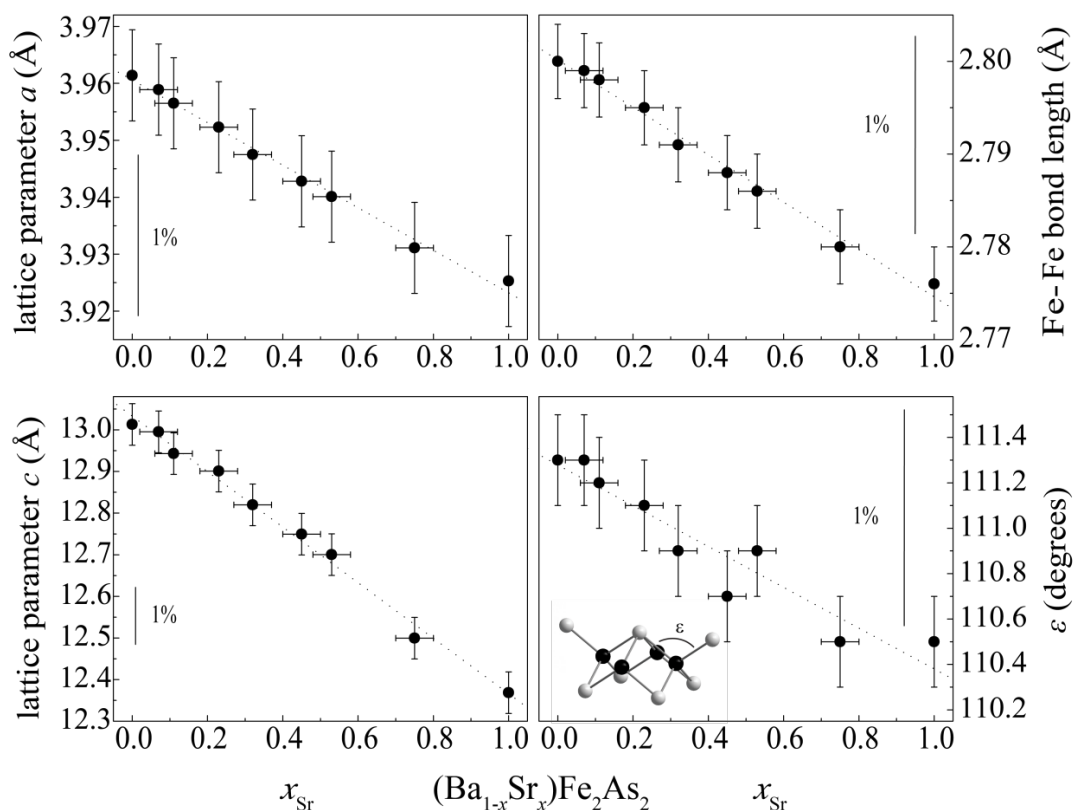


Figure 8.4: Structural parameters in $(\text{Ba}_{1-x}\text{Sr}_x)\text{Fe}_2\text{As}_2$ with $x = 0 - 1$. Dotted lines are guide for the eye.

The lattice parameters a and c decrease linearly with the strontium content over the whole range. Consequently, the unit cell volume shrinks linearly with a total of approximately 6 %. Beside the lattice parameters also the Fe–Fe bond length and the As–Fe–As bond angle ε decrease linearly with increasing strontium content. This means that the FeAs₄ tetrahedra get slightly stretched along the c -axis and the iron atoms within the layers move together. Both phenomena are found for potassium doping as well (see chapter 6) but the change is only $\sim 1\%$ in total and are therefore much less pronounced in (Ba_{1-x}Sr_x)Fe₂As₂ where the change of the Fe–Fe bond length and the bond angle ε is about 4 %. In contrast to the previously described potassium doped samples the ideal tetrahedral angle of 109.5° is not reached with Sr-doping. As the Fe–As bond length remain almost constant ($\Delta_{\text{Fe-As}} \sim 0.6\%$) they are not depicted.

For investigations concerning the effect of Sr-doping in BaFe₂As₂ with respect to its structural phase transition, the electric resistivity of all samples were measured as described above for (Ba_{0.5}Sr_{0.5})Fe₂As₂. SrFe₂As₂ exhibits the same SDW anomaly as BaFe₂As₂, but at 205 K instead of 140 K.^[125] This is evident since the magnetic behavior of the iron arsenide layers strongly depends on the occupation of the Fe $3d_{x^2-y^2}$ -orbitals which depend on the position of arsenic atoms.^[125] Thus, with the smaller strontium atoms, a stronger magnetic character of the iron arsenide layers and consequently a higher ordering temperature is observed. In the mixed crystals, where barium is substituted for strontium, spin density wave transitions are detected for all samples as presented in Figure 8.3 for (Ba_{0.5}Sr_{0.5})Fe₂As₂. Figure 8.5 shows the dependence of the spin density wave transition temperature T_{SDW} in relation to the unit cell volume and it is recognizable that T_{SDW} decreases continuously from SrFe₂As₂ to BaFe₂As₂.

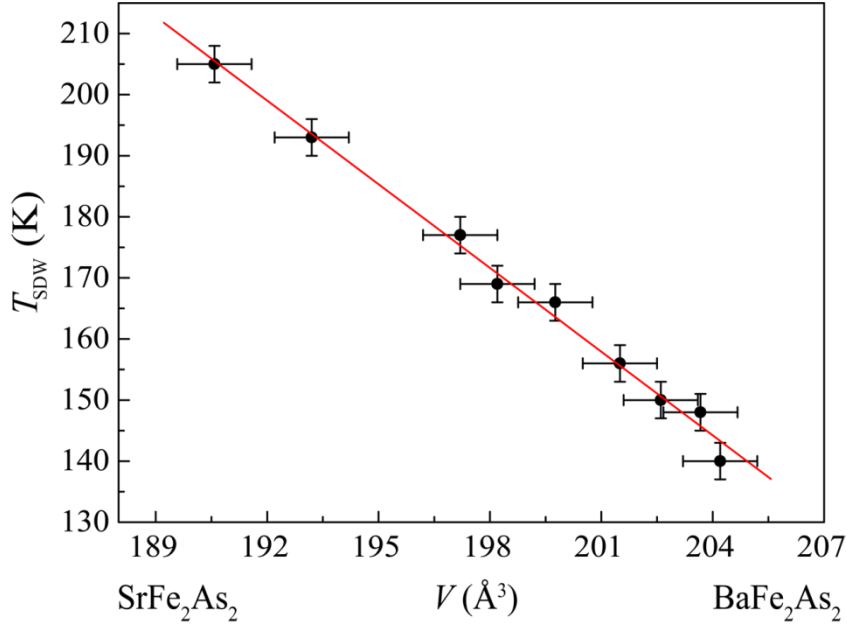


Figure 8.5: SDW-transition temperatures T_{SDW} of $(\text{Ba}_{1-x}\text{Sr}_x)\text{Fe}_2\text{As}_2$.

8.2 BaFe(As_{1-x}P_x)₂

Although “chemical pressure” in $(\text{Ba}_{1-x}\text{Sr}_x)\text{Fe}_2\text{As}_2$ was successful concerning a reduction of the unit cell volume, no superconductivity could be observed. Another approach of applying “chemical pressure”, however, is the substitution of arsenic for phosphorus in a solid solution $\text{BaFe}_2(\text{As}_{1-x}\text{P}_x)_2$ ($x = 0 - 1$). Phosphorus doping of the arsenic site was already successfully performed in $\text{EuFe}_2(\text{As}_{0.7}\text{P}_{0.3})_2$, which becomes superconducting at 26 K.^[126] The following sections will present synthesis and properties of the phosphorus doped BaFe_2As_2 and discuss the influence of isoelectronic doping on the different doping sites.

8.2.1 Synthesis

Samples of $\text{BaFe}_2(\text{As}_{1-x}\text{P}_x)_2$ with $x = 0 - 1$ were synthesized by solid state reactions of the elements. The stoichiometric mixtures were slowly heated to 1123 K (1173 K) for 15 h. After cooling down to room temperature, the products

Isoelectronic Doping of BaFe₂As₂

were ground, if necessary pressed into pellets, and annealed at 1173 K for 25 h (two to three times at 1323 K and 1423 K, respectively). The accurate temperature programs are listed in Table 8.2. In general, the reaction temperatures had to be increased with increasing phosphorus content. The most difficult sample to prepare was BaFe₂(As_{0.5}P_{0.5})₂ which required beside a pre-reaction additional four annealing steps at temperatures as high as 1323 K. The black crystalline powders showed no sensitivity to air and moisture. EDX measurements resulted in the nominal compositions with a variation of about 10 % regarding to the As : P ratios.

Table 8.2: Temperature programs for the synthesis of BaFe₂(As_{1-x}P_x)₂ ($x = 0 - 1$): Heating rate (K/h) → reaction temperature (K) / dwell time (h) → temperature ramp (K/h) → room temperature (rt).

Compound	Reaction step	Temperature program
BaFe ₂ P ₂	Reaction	50 K/h → 1223 K / 20 h → 200 K/h → rt
	1. Annealing step	100 K/h → 1323 K / 15 h → 200 K/h → rt
	2. Annealing step	150 K/h → 1423 K / 20 h → 200 K/h → rt
BaFe ₂ (As _{1-x} P _x) ₂ $x = 0.9 - 0.4$	Reaction	50 K/h → 1173 K / 15 h → 200 K/h → rt
	1. Annealing step	100 K/h → 1273 K / 15 h → 200 K/h → rt
	2. Annealing step	150 K/h → 1323 K / 20 h → 200 K/h → rt
For BaFe ₂ (As _{0.5} P _{0.5}) ₂	3. Annealing step (Powder)	300 K/h → 1323 K / 15 h → 200 K/h → rt
	4. Annealing step (Pellet)	300 K/h → 1323 K / 15 h → 200 K/h → rt
BaFe(As _{1-x} P _x) ₂ $x = 0.3 - 0.1$	1. Reaction	100 K/h → 573 K → 20 K/h → 873 K / 3 h → 50 K/h → 1123 K / 10 h → 200 K/h → rt
	Annealing step	100 K/h → 1173 K / 25 h → 100 K/h → rt

8.2.2 Crystal Structures

A Huber G670 Guinier imaging plate diffractometer was employed to determine the crystal structures by X-ray powder diffraction. Rietveld refinements of all powder patterns were performed with the TOPAS package.^[23] For the mixed crystals the atom positions of BaFe₂As₂ (see chapter 4) or BaFe₂P₂^[127] were used as starting parameters for the Rietveld refinement. The pnictogen ($Pn = \text{As}, \text{P}$) atoms occupy the $4e$ ($00z$) position, where z_{Pn} is the only variable parameter of the tetragonal ThCr₂Si₂-type structure. Their occupation parameters were constraint to unity.

Phase purity was achieved only for the undoped phases BaFe₂As₂ and BaFe₂P₂. All other samples of the mixed crystals BaFe₂(As_{1-x}P_x)₂ contain small impurity phases Fe₂P and / or an unidentified impurity phase with a reflection appearing at $\approx 29^\circ 2\theta$.

Figure 8.6 shows exemplary the Rietveld refinement of BaFe₂(As_{1-x}P_x)₂ ($x = 0.4$) which has been successfully refined in the tetragonal cell with the space group $I4/mmm$. The reflection of the impurity phase at $\approx 29^\circ 2\theta$ is marked with an asterisk as it is barely visible. The crystallographic data of this refinement are given in Table 8.3.

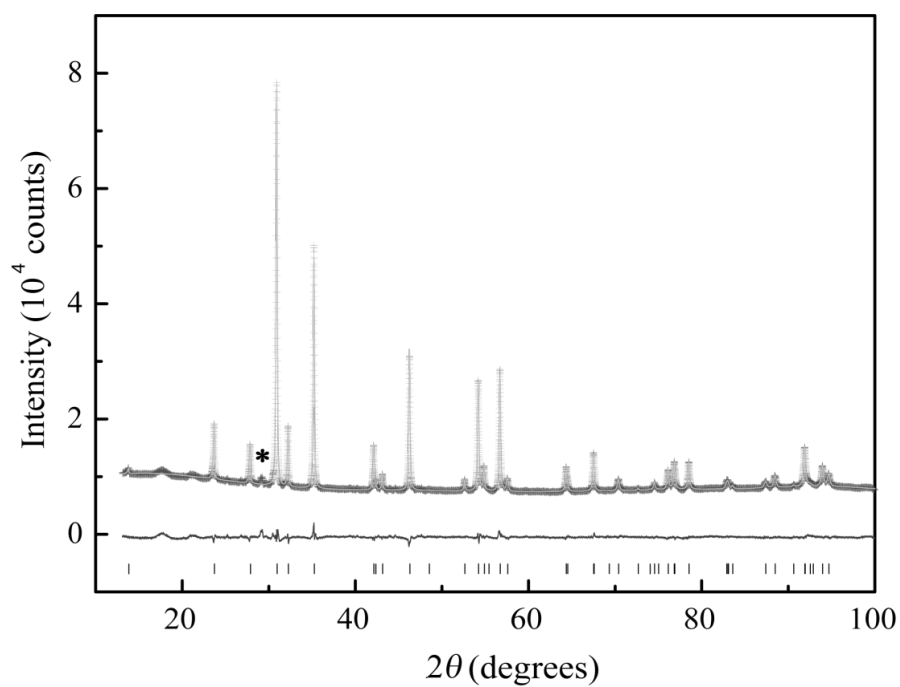


Figure 8.6: Measured (+) and calculated (–) X-ray powder pattern of $\text{BaFe}_2(\text{As}_{0.6}\text{P}_{0.4})_2$. Reflection markers are black for the nominal composition $\text{BaFe}_2(\text{As}_{0.6}\text{P}_{0.4})_2$. The asterisk marks an unindexed reflection attributed to an unidentified impurity phase.

Table 8.3: Crystallographic data of the Rietveld refinement of BaFe₂(As_{1-x}P_x)₂ with $x = 0.4$.

Diffractometer	Huber G670
Radiation	Cu-K _{α1}
Space group	<i>I4/mmm</i>
<i>a</i> (pm)	391.99(1)
<i>b</i> (pm)	= <i>a</i>
<i>c</i> (pm)	1279.24(1)
<i>V</i> (nm ³)	0.19657(1)
<i>Z</i>	2
Data points	8730
Reflections	44
<i>d</i> range	1.047-6.396
<i>R</i> _p , <i>wR</i> _p	0.0128, 0.0184
<i>R</i> _{bragg} , χ^2	0.013, 1.731
Atomic parameters	
Ba	2 <i>a</i> (0,0,0) <i>U</i> _{iso} = 98(3)
Fe	4 <i>d</i> (½,0,¼) <i>U</i> _{iso} = 46(3)
As, P	4 <i>e</i> (0,0, <i>z</i>) <i>z</i> = 0.3519(1) <i>U</i> _{iso} = 58(4)
As : P ratio	61(1) : 39(1)
Bond lengths (pm)	
Ba–As/P	335.8(1) x 8
Fe–As/P	235.3(1) x 4
Fe–Fe	277.2(1) x 4
Bond angles (deg)	
As/P–Fe–As/P	112.8(1) x 2 107.8(1) x 4

Isoelectronic Doping of BaFe₂As₂

Like BaFe₂(As_{0.61}P_{0.39})₂ all other samples of the solid solution BaFe₂(As_{1-x}P_x)₂ with $x = 0 - 1$ crystallize in the tetragonal space group $I4/mmm$, too. The size of the unit cell of BaFe₂P₂ is much smaller than of BaFe₂As₂ due to the smaller ionic radius of phosphorus. The unit cell volume is consequently decreased by 10.4 % and the lattice parameters a and c by 3.2 % and 4.4 %, respectively, shorter than in the arsenic compound. Concerning the atomic distances the Fe– Pn bond length shortens by 6 % from 240.3 pm to 225.8 pm as can be seen from the comparison of selected crystallographic data in Table 8.4. Additionally, the Pn –Fe– Pn bond angle is widened in the phosphorus compound so that the FeP₄ tetrahedra are flattened along the c -axis compared to the FeAs₄ tetrahedra in BaFe₂As₂.

Table 8.4: Selected structural parameters of BaFe₂ Pn ₂ ($Pn = As, P$).

	BaFe ₂ P ₂	BaFe ₂ As ₂ ^[65]
Space group	$I4/mmm$	$I4/mmm$
a (pm)	383.71(1)	396.25(1)
b (pm)	$= a$	$= a$
c (pm)	1243.76(1)	1301.68(3)
V (nm ³)	0.18312(1)	0.20438(1)
Bond lengths (pm)		
Ba– Pn	332.4(1) x 8	338.2(1) x 8
Fe– Pn	225.8(1) x 4	240.3(1) x 4
Fe–Fe	271.3(1) x 4	280.2(1) x 4
Bond angles (deg)		
Pn –Fe– Pn	116.4(1) x 2	111.1(1) x 2
	106.1(1) x 4	108.7(1) x 4

The evaluation of all crystallographic data of BaFe₂(As_{1-x}P_x)₂ ($x = 0 - 1$) are compiled in Figure 8.7.

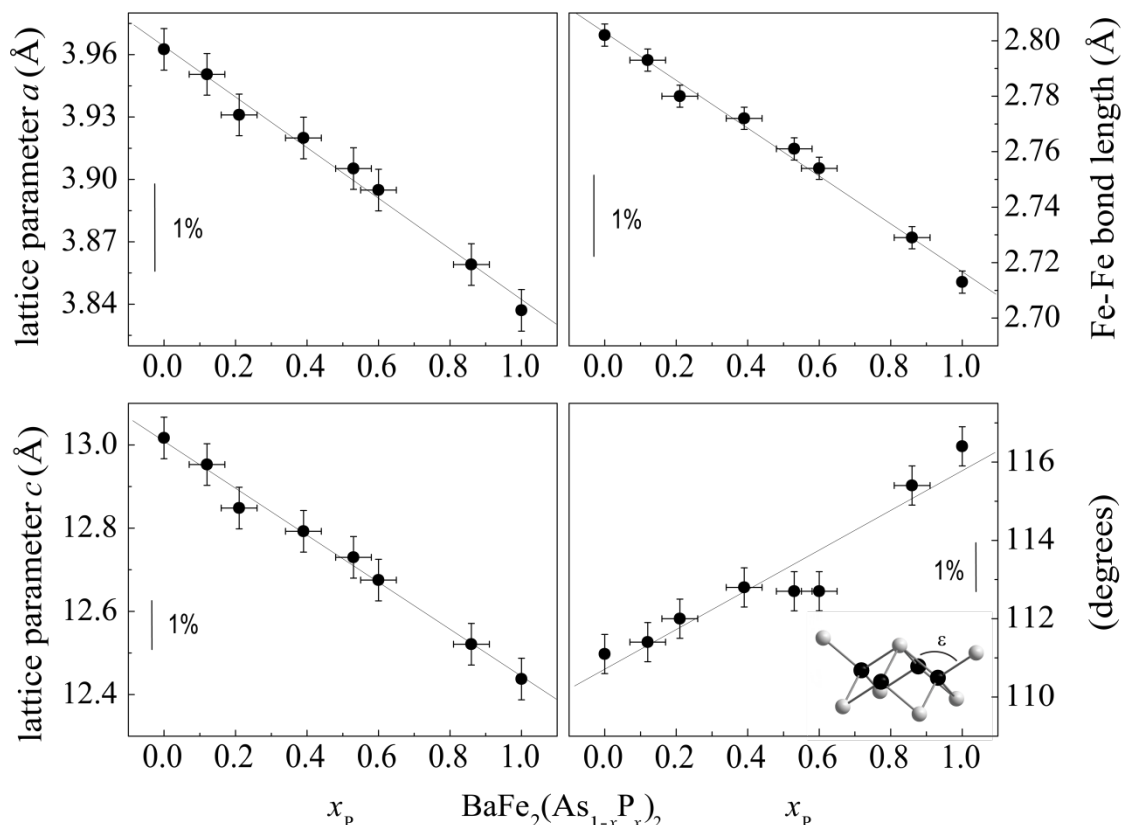


Figure 8.7: Structural parameters of the solid solution $\text{BaFe}_2(\text{As}_{1-x}\text{P}_x)_2$ ($x = 0 - 1$). Lines are guides for the eye.

As it can be clearly seen from Figure 8.7 the lattice parameters of the mixed crystals $\text{BaFe}_2(\text{As}_{1-x}\text{P}_x)_2$ with $x = 0 - 1$ follow Vegard's law and develop linearly with the composition. While the lattice parameters and the Fe–Fe atomic distances shrink, the $Pn\text{--}Fe\text{--}Pn$ bond angle widens. Consequently the FePn_4 tetrahedra get flatter with higher phosphorus content. As it can be seen from the shrinking lattice parameters and therefore the change in structural parameters, the application of “chemical pressure” by substituting arsenic for the smaller phosphorus was successful. But does this lead to superconductivity? To answer this question electrical resistance measurements were performed which will be presented in the following chapter.

8.2.3 Electrical Resistance Measurements

For electrical resistance measurements the samples were pressed into pellets like described in chapter 3 and sintered at 1273 K for 15 h (BaFe_2P_2), 10 h ($\text{BaFe}_2(\text{As}_{1-x}\text{P}_x)_2$ ($x = 0.4 - 0.9$)) or at 1173 K for 15 h ($\text{BaFe}_2(\text{As}_{1-x}\text{P}_x)_2$ ($x = 0.1 - 0.3$)), respectively. As shown in Figure 8.8 the specific resistance of $3 \cdot 10^{-6} \Omega\text{m}$ of BaFe_2P_2 decreases smoothly, as it is typical for normal metals. In contrast to BaFe_2As_2 no SDW anomaly can be seen in BaFe_2P_2 .

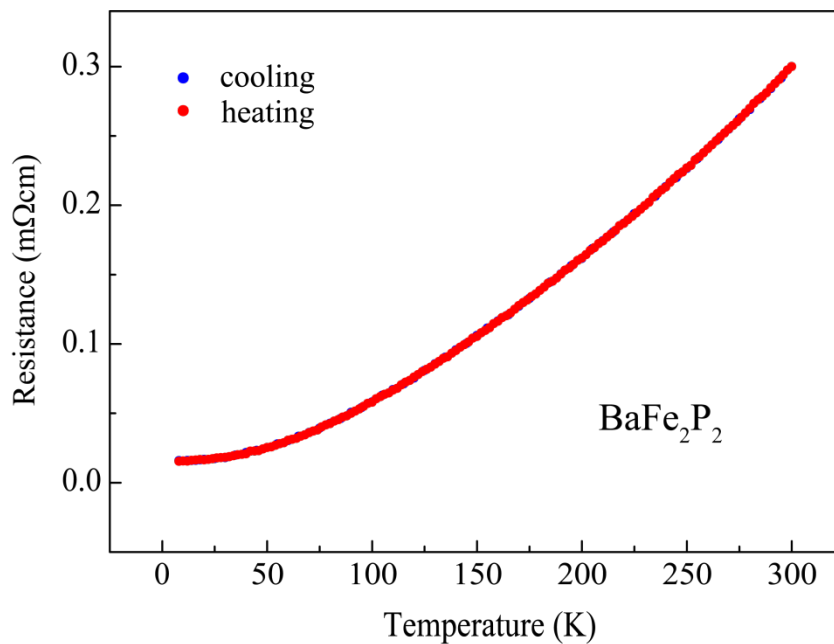


Figure 8.8: *dc* resistivity of BaFe_2P_2 .

In contrast to $(\text{Ba}_{1-x}\text{Sr}_x)\text{Fe}_2\text{As}_2$ where both ternary phases BaFe_2As_2 and SrFe_2As_2 show the same behavior, the ternary phases BaFe_2P_2 and BaFe_2As_2 differ regarding their physical properties. As presented in section 8.1 mixed crystals of $(\text{Ba}_{1-x}\text{Sr}_x)\text{Fe}_2\text{As}_2$ behave in the same manner as the undoped phases. As the pure phases of $\text{BaFe}_2(\text{As}_{1-x}\text{P}_x)_2$ ($x = 0, 1$) show different properties, what will the behavior of the mixed crystals be?

Figure 8.9 shows the dc resistivities of $\text{BaFe}_2(\text{As}_{1-x}\text{P}_x)_2$ with $x = 0.12$, 0.37 and 0.86.

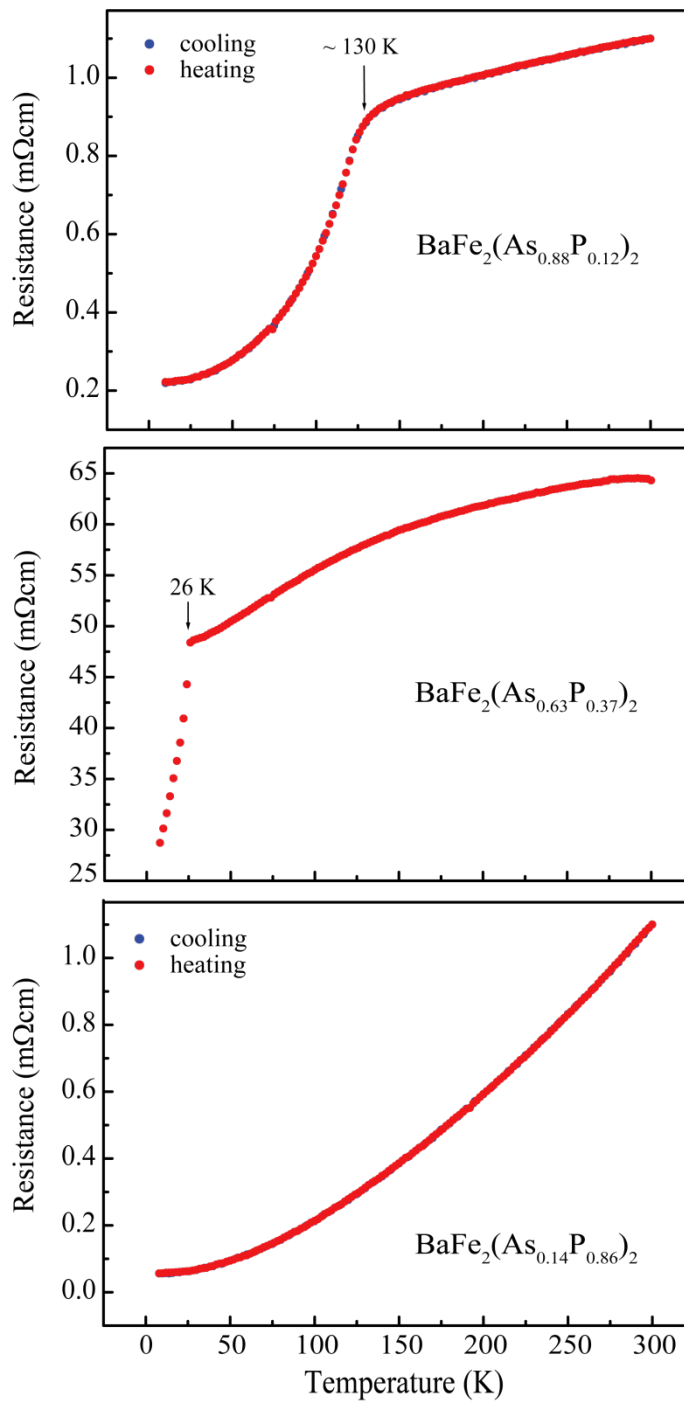


Figure 8.9: dc resistivities of $\text{BaFe}_2(\text{As}_{1-x}\text{P}_x)_2$ with $x = 0.12$ (top), 0.37 (middle) and 0.86 (bottom).

The sample with small phosphorus content of $x = 0.12$ shows the same spin density wave anomaly as the parent compound BaFe₂As₂, but shifted towards lower temperatures of ~ 130 K. At a doping level of $x = 0.37$, the SDW is suppressed and the resistivity drops abruptly at ≈ 26 K associated with a superconducting transition, even though zero resistance could not be reached at 8 K. This could be attributed to grain boundaries and/or impurity phases like Fe₂P rather than sample inhomogeneity since nearly perfect diamagnetism was measured as shown in Figure 8.10.

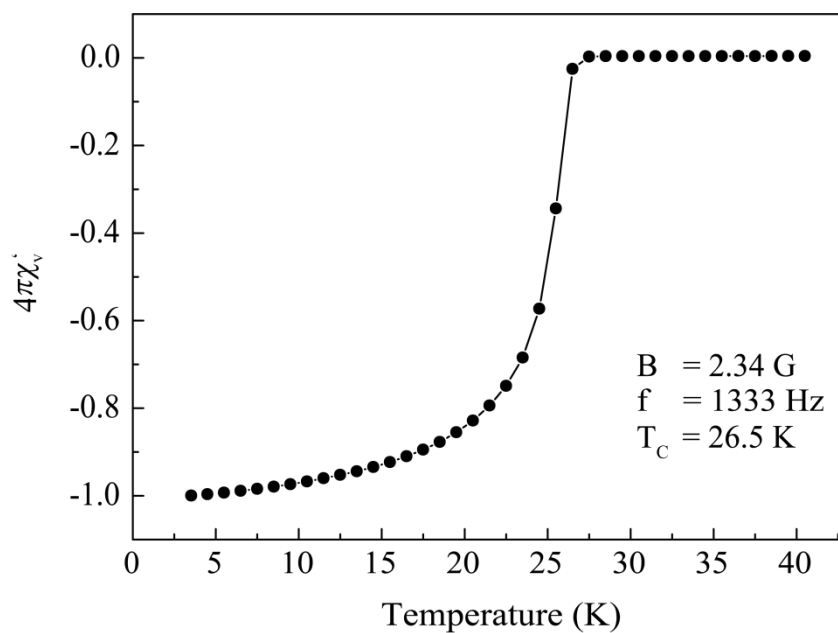


Figure 8.10: *ac* susceptibility of BaFe₂(As_{1-x}P_x)₂ with $x \approx 0.4$.

Increasing the phosphorus content as shown for BaFe₂(As_{0.14}P_{0.86})₂ (Figure 8.9) the curvature of the resistivity is reminiscent to the resistance of the pure BaFe₂P₂ (Figure 8.8) where the compound is a normal metal and does not show a superconducting transition down to 8 K.

In summary, all samples between $x = 0.3$ and 0.6 show superconductivity with critical temperatures up to 29 K, whereas the mixed crystals with a doping level below and above 0.3 and 0.6, respectively, show the behavior of the respective ternary compound BaFe₂As₂ for $x < 0.3$ and BaFe₂P₂ for $x > 0.6$.

8.3 Conclusion

Two different approaches to apply “chemical pressure” on BaFe₂As₂ were carried out and the physical properties of the resulting solid solutions were investigated. A first attempt was the substitution of the Ba²⁺ cation for the smaller Sr²⁺ that led to a compression of the unit cell volume by 6 % which is comparable to the unit cell volume found in high pressure experiments by Kimber *et al.*^[124] The second approach of shrinking the unit cell volume of BaFe₂As₂ was another charge neutral substitution of arsenic for the smaller phosphorus. Again, the volume could be decreased by 10.4 % which is almost twice the value reached by high pressure experiments. Figure 8.11 shows the dependency of the unit cell volume on the doping level together with the values of the undoped BaFe₂As₂ under pressure which were taken from literature.^[124] Superconducting compounds are indicated by circles.

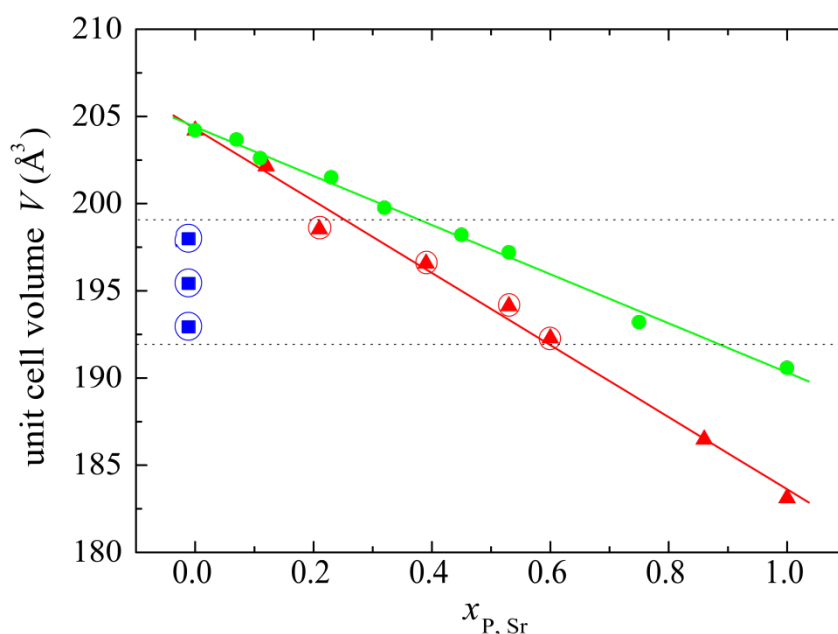


Figure 8.11: Dependency of the unit cell volume on the doping level in mixed crystals of BaFe₂(As_{1-x}P_x)₂ (red) and (Ba_{1-x}Sr_x)Fe₂As₂ (green) ($x = 0 - 1$). Superconducting samples are marked by circles. Values of the undoped BaFe₂As₂ under pressure (blue) are taken from the literature.^[124]

Indeed superconductivity appears by pressure and by P doping within the same volume range between 192 Å³ and 199 Å³, which is marked by the dashed lines. But on the other hand, no superconductivity emerges by Sr-doping in (Ba_{1-x}Sr_x)Fe₂As₂, even though the unit cell volumes are within the same range. Obviously, the simple shrinking of the unit cell as suggested by Kimber *et al.*^[124] is not the decisive condition. Superconductivity is absent in (Ba_{1-x}Sr_x)Fe₂As₂ because strontium doping does not suppress the magnetic and structural transition, as SrFe₂As₂ shows the same SDW anomaly as BaFe₂As₂. Solely the transition temperature becomes shifted to higher temperatures as depicted in Figure 8.5. BaFe₂P₂, however, differs from the properties of BaFe₂As₂ as it is a normal metal without any structural or magnetic transition. Mixed crystals of BaFe₂(As_{1-x}P_x)₂ exhibit a different behavior depending on the As : P ratio. At $x \approx 0.3$ the structural and magnetic phase transition is suppressed and superconductivity emerges whereas the curvature of the resistivity for compounds with doping levels higher than $x \approx 0.6$ show a normal metal. No superconductivity could be observed down to 8 K in these compounds.

The results discussed above were confirmed by reports on both solid solutions (Ba_{1-x}Sr_x)Fe₂As₂^[128] and BaFe₂(As_{1-x}P_x)₂^[129] which were published while this work was completed. At first BaFe₂(As_{1-x}P_x)₂^[129] was published and the authors explain the appearance of superconductivity as a consequence of the shrinking unit cell volume in analogy to the effects of external pressure. On the other hand, no superconductivity appears in the case of (Ba_{1-x}Sr_x)Fe₂As₂^[128] although the unit cell volume shrinks comparably to the phosphorus doped samples. Thus, a pressure-volume effect is obviously an oversimplified view, and cannot explain the different response of isoelectronic doping of BaFe₂As₂ in both cases. In order to shed light on this contradiction, a detailed look at the crystal structures is indispensable. Therefore, detailed single crystal investigations of the phosphorus doped BaFe₂(As_{1-x}P_x)₂ samples are presented in the next section.

8.4 Structural Subtleties

8.4.1 Single Crystal Investigations of BaFe₂(As_{1-x}P_x)₂

For single crystal investigations small platelike crystals of $\approx 50 \times 50 \times 20 \mu\text{m}^3$ were selected from polycrystalline samples of BaFe₂(As_{1-x}P_x)₂ and checked by Laue photographs for suitability. Diffraction intensity data up to $2\theta = 80^\circ$ were collected with an Oxford Xcalibur four circle κ -diffractometer equipped with a charge-coupled-device detector. The intensities were carefully corrected for absorption effects. The atom positions of BaFe₂As₂ (see chapter 4) were used as starting parameters and refined by the least-squares method using the SHELXL program package.^[35,36] Positional and isotropic displacement parameters of As and P were refined independently, while their occupation parameters were constraint to unity.

8.4.2 Crystal Structure Properties

As already shown in the Figure 8.10 the unit cell volumes of (Ba_{1-x}Sr_x)Fe₂As₂ and BaFe₂(As_{1-x}P_x)₂ shrink in a similar fashion, although the volume reduction of BaFe₂(As_{1-x}P_x)₂ is nearly twice that of (Ba_{1-x}Sr_x)Fe₂As₂. The unit cell volumes of both, however, pass the same range from 192 Å³ to 199 Å³. Within this range superconductivity emerges in BaFe₂As₂ under pressure^[124] and also in the phosphorus doped BaFe₂(As_{1-x}P_x)₂ (see chapter 8.2). In contrast no superconductivity is observed in (Ba_{1-x}Sr_x)Fe₂As₂. Thus, a simple pressure-volume effect cannot be the crucial parameter for the induction of superconductivity. Another structural parameter which will be discussed here in this context is the Fe–Pn atomic distance. The doping dependencies of the normalized Fe–Pn (Pn = As, P) bond lengths determined from Rietveld refinements of the powder patterns are plotted in Figure 8.12. Strontium and

phosphorus doped BaFe_2As_2 show very different behavior, respectively. While the Fe–As bond lengths in $(\text{Ba}_{1-x}\text{Sr}_x)\text{Fe}_2\text{As}_2$ remain almost constant across the whole doping range despite the shrinking unit cell, the Fe–Pn distances decrease strongly with increasing P content in $\text{BaFe}_2(\text{As}_{1-x}\text{P}_x)_2$. This strongly suggests that a shortening of the Fe–Pn bonds is necessary to suppress the SDW transition. The latter is plausible, since it is well known that the Fe–As bond length dramatically influences the magnetism in iron arsenides.^[130,131]

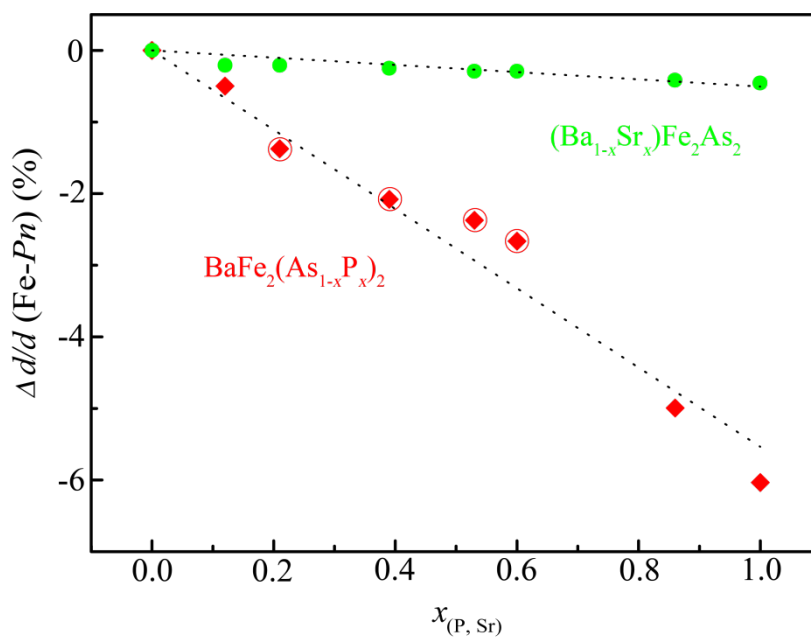


Figure 8.12: Normalized Fe–Pn distances ($Pn = \text{As}, \text{P}$) of $(\text{Ba}_{1-x}\text{Sr}_x)\text{Fe}_2\text{As}_2$ (green) and $\text{BaFe}_2(\text{As}_{1-x}\text{P}_x)_2$ (red) obtained from Rietveld refinements. Superconducting samples are marked by circles.

From crystal chemical considerations, the Fe–As distances in $(\text{Ba}_{1-x}\text{Sr}_x)\text{Fe}_2\text{As}_2$ are reasonable due to only one arsenic position. The values for the Fe–Pn bond lengths of $\text{BaFe}_2(\text{As}_{1-x}\text{P}_x)_2$ obtained from Rietveld refinements, however, are not reasonable for chemical reasons. They indicate, that a Fe–As bond in a highly doped compound like $\text{BaFe}_2(\text{As}_{0.14}\text{P}_{0.86})_2$ shortens by $\approx 5\%$ from 240 pm to 228.3 pm, much too small for a Fe–As bond. Conversely this means, that the

Fe–P atomic distance increases from 225.8 pm in the pure phosphide BaFe₂P₂ to 239.1 pm in BaFe₂(As_{0.88}P_{0.12})₂ which is much too long for a Fe–P bond. In order to shed light on this situation, high-resolution single crystal X-ray structure determinations were conducted using small crystals of BaFe₂(As_{1-x}P_x)₂ with $x \approx 0.3, 0.5$ and 0.7 . Main results of the refinements together with selected bond lengths and angles are summarized in Table 8.5. As expected for chemical reasons, the P- and As atoms are found at significantly different z -coordinates, resulting in different lengths of the Fe–As and Fe–P bonds.

Isoelectronic Doping of BaFe₂As₂

Table 8.5: Crystallographic data of BaFe₂(As_{1-x}P_x)₂ ($x = 0, 0.29, 0.47, 0.76, 1$) at $T = 173$ K. Standard deviations are given in parentheses.

		BaFe ₂ (As _{1-x} P _x) ₂				
P content x	$x = 0$	$x = 0.29$	$x = 0.47$	$x = 0.76$	$x = 1$	
Molar Mass (g/mol)	398.88	372.95	357.63	331.86	319.77	
Crystal system	Tetragonal					
Space group	$I4/mmm$					
Diffractometer	Oxford Xcalibur					
Radiation	Mo-K α_1 radiation ($\lambda = 71.073$ pm)					
a (pm)	396.22(4)	391.78(1)	390.65(1)	386.60(3)	384.35(4)	
c (pm)	1300.1(1)	1276.10(7)	1273.55(6)	1259.2(1)	1242.2(2)	
V (nm ³)	0.2041(1)	0.1959(1)	0.1944(2)	0.1892(4)	0.1835(2)	
Z	2	2	2	2	2	
Abs. coeff. (mm ⁻¹)	32.4	29.1	27.1	22.5	20.7	
$R_{\text{int}}, R_{\sigma}$	0.044, 0.029	0.030, 0.013	0.035, 0.016	0.050, 0.021	0.093, 0.042	
Refined Parameters	9	10	10	10	8	
R_1 (all data)	0.028	0.023	0.020	0.033	0.031	
wR_2 (all data)	0.061	0.049	0.035	0.082	0.060	
Goodness-of-fit (F^2)	1.09	1.19	1.06	1.15	0.997	
As z position	0.35393(8)	0.3544(1)	0.3542(1)	0.3571(4)	–	
P z position	–	0.3402(1)	0.3438(4)	0.3430(4)	0.3459(1)	
Bond Lengths (pm)						
Ba–As	338.47(7)	333.58(7)	332.2(1)	327.3(2)	–	
Ba–P	–	344.0(2)	339.6(3)	337.4(2)	332.4(1)	
Fe–As	239.80(6)	236.89(7)	236.1(1)	235.7(3)	–	
Fe–P	–	227.2(4)	228.9(3)	226.2(2)	226.14(9)	
Bond Angles (deg)						
As–Fe–As	111.4(1)	111.57(5)	111.6(2)	110.2(2)	–	
As–Fe–P	–	115.4(3)	114.4(1)	113.9(1)	–	
P–Fe–P	–	119.1(3)	117.1(2)	117.6(1)	116.39(7)	

The initial Fe–As distance is 240 pm and decreases rapidly up to ≈ 25 % P-doping, but then converges to an almost constant value around 236 pm (-1.7 %). At the same time, the Fe–P distances remain about 1–2 pm longer than in BaFe₂P₂ at least up to 75 % P-doping. This leads to a distortion of the FePn₄

tetrahedra, which are not longer regular tetrahedra with four equal Fe–As bonds, but with statistically distributed, varying Fe– P_n bond lengths. Consequently the iron pnictide layers get slightly undulated. Figure 8.13 summarizes this reorganization of the crystal structures of $\text{BaFe}_2(\text{As}_{1-x}\text{P}_x)_2$ in comparison with $(\text{Ba}_{1-x}\text{Sr}_x)\text{Fe}_2\text{As}_2$.

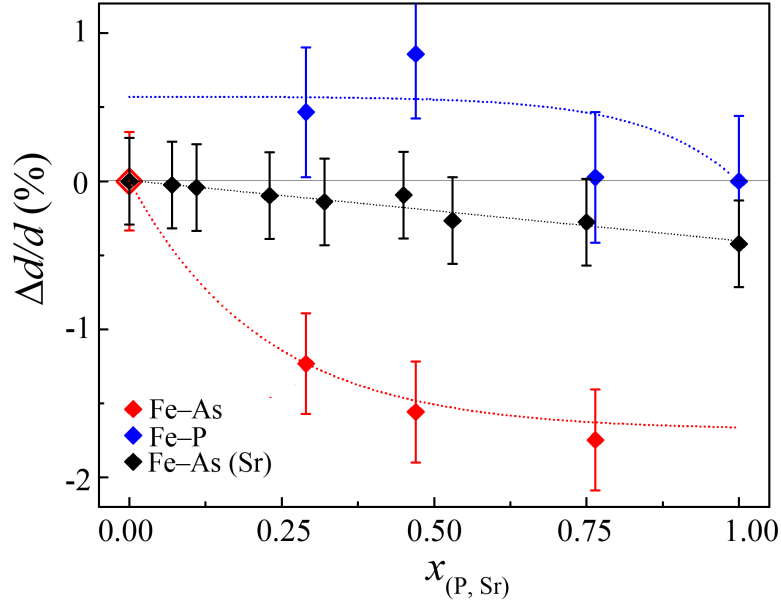


Figure 8.13: Changes in the normalized Fe–As and Fe–P bond lengths in $\text{BaFe}_2(\text{As}_{1-x}\text{P}_x)_2$ values from single crystal data and in $(\text{Ba}_{1-x}\text{Sr}_x)\text{Fe}_2\text{As}_2$ values from powder diffraction. Error bars represent four times the estimated standard deviations. Dotted lines are guide for the eye.

A small contraction of the Fe–As bonds by $\approx -1.5\%$ (2–3 pm) is associated with the suppression of the SDW state, which is in turn the precondition to superconductivity. This happens by P-, but not by Sr-doping, where the Fe–As bonds shrink by less than 0.5%.

These results were also almost quantitatively reproduced by DFT calculations^[132] which were performed using ordered model structures of $\text{BaFe}_2(\text{As}_{1-x}\text{P}_x)_2$ and calculated structural parameters of the doping levels $x = 0.25, 0.5$ and 0.75 without changing symmetry. From these calculations it is evident that the z_{P_n} coordinates of arsenic and phosphorus become significantly different, which

leads to longer Fe–As and shorter Fe–P bonds, as it is expected from atom-size considerations. At a doping level between $x = 0$ and 0.25 the Fe–As bonds shrink significantly accompanied by the loss of the magnetic moment. The contraction is about -1.4% , which is sufficient to suppress the SDW order. Higher doping levels do not further contract the Fe–As bonds. At the same time, the Fe–P bonds remain close to the values of the pure phosphide BaFe₂P₂. These findings match very well with the experimental data extracted from the single-crystal investigations.

8.4.3 Conclusion

The last section strongly emphasizes that even subtle details of the crystal structures are crucial to magnetism and superconductivity in the iron arsenides. Such structural subtleties of mixed crystals of BaFe₂(As_{1-x}P_x)₂ with $x = 0, 0.29, 0.47, 0.76$ and 1 were extracted from single-crystal X-ray data. Here, arsenic and phosphorus are statistically distributed, but at different coordinates z_{As} and z_{P} , which is necessary to obtain reasonable Fe–P and Fe–As bond lengths. The latter contract strongly at low doping levels during magnetism is suppressed ($0 \leq x \leq 0.25$). At higher doping levels the Fe–As atomic distance converges to ≈ 236 pm while the Fe–P bond lengths remain close to the values of the pure BaFe₂P₂. Interestingly, a comparable shortening of the Fe–As bond length was recently observed in undoped BaFe₂As₂ under pressure,^[133] and might explain the occurrence of superconductivity induced by external pressure even better than for the reason of a simple pressure-volume effect.

9 ARPES Measurements

9.1 Theoretical Aspects

Among all efforts to synthesize and characterize new high- T_C superconductors, scientists still desire to disclose the secret of the mechanism of high- T_C superconductivity. More than 500 theoretical papers beside more than four times the number of experimental papers on the Fe-based superconductors have been published, all trying to elucidate the mystery of superconductivity. A general consensus in this context is that the formation of Cooper pairs is of an unconventional nature in these compounds, where pairing is not mediated by electron-phonon coupling. The iron arsenides represent the first example of multigap superconductivity with a discontinuous sign change of the order parameter phase between bands, which was not observed in any other compound before.^[134] The superconducting order parameter (also superconducting wave function) is a quantum mechanical description for the pairing of electrons in the superconducting state. This pairing could be of a spatial isotropic nature, which would be designated as *s*-wave superconductivity, or anisotropic like for example in the cuprates, where physicists refer to *d*-wave superconductivity.^[135]

Generally, in all superconductors the repulsive force between two electrons must be overcome by pairing that superconductivity emerges. In the conventional superconductors, which are well described by the BCS theory,^[136,137] pairing arises from a normal metallic state, where electrons at the Fermi level move freely and hardly sense changes in their vicinity, but by a small attractive interaction, which is generated by a phonon, these electrons pair despite the strong coulomb repulsion. As the phonon mediated pairing is typically isotropic, physicists refer to *s*-wave superconductivity.

In unconventional superconductors, namely the cuprates, however, superconductivity is supposed to be mediated by spin fluctuations, but this kind of pairing mechanism is only possible if their wavefunctions have opposite signs. ARPES measurements revealed four directions of electron momentum in which the pairing amplitude is zero (which is called “nodes” in the superconducting order parameter), and the pairing symmetry was therefore assumed to have d -wave symmetry^[135] in the cuprates (see Figure 9.1, left hand side). This means, that the Cooper pairs orbit each other with a particular angular momentum to avoid close contact to each other, and thus reducing their mutual Coulomb repulsion.

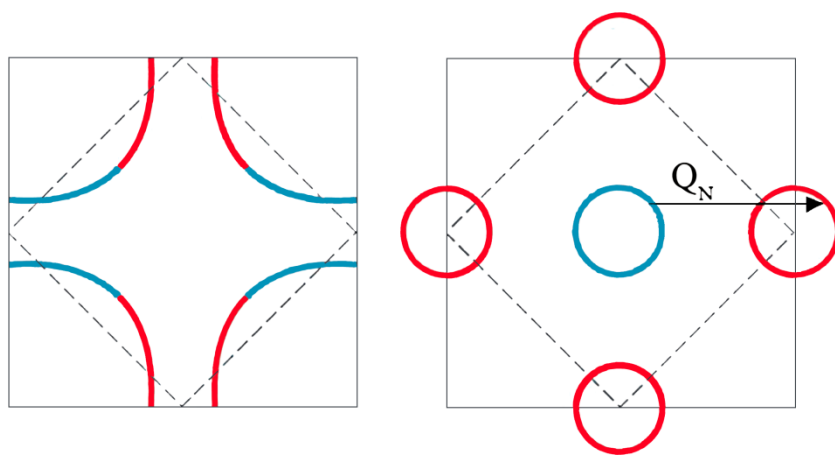


Figure 9.1: Scheme of Fermi surfaces as a function of electrons momentum illustrates pairing symmetries. Solid gray lines show the Brillouin zones. The Fermi surfaces are marked in blue (positive signs) and red (negative signs). Left: d -wave symmetry. The nodes occur where the blue and the red arcs touch. Right: s^\pm -wave symmetry ($Q_N =$ nesting vector).^[138]

In the iron arsenides, there are no nodes in the superconducting order parameter on any Fermi surface sheet, thus physicists speak of s -wave superconductivity (see Figure 9.1, right). As superconductivity in this class of high- T_C superconductors is also thought to be mediated by spin fluctuations this requires a sign change in the order parameter. Calculations of Mazin *et al.*^[134] showed that the different Fermi surface sheets have thoroughly the same shape, but are offset

from each other by a momentum vector Q , called the nesting vector, which corresponds to the q -value, where antiferromagnetic spin fluctuations have been detected by inelastic neutron scattering. They conclude that a spin-mediated inter-orbital pairing mechanism between hole and electron pockets is energetically favorable, when the order parameter changes sign between the nested surfaces. Fermi surface nesting means that large segments of a Fermi surface can be connected to another large segment of another Fermi surface via the same reciprocal lattice vector. Here, nesting occurs between the Fermi surface hole pockets at the center of the Brillouin zone (Γ point, see Figure 9.2) and the electron pockets at the zone corner (X points). The Brillouin zone of tetragonal BaFe_2As_2 is illustrated in Figure 9.2.^[40]

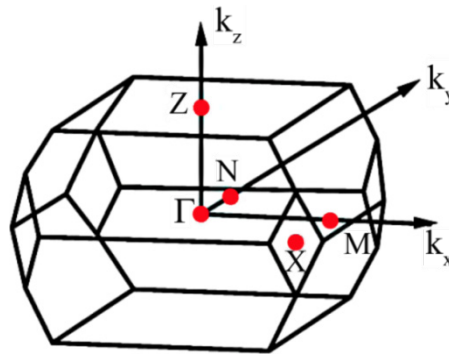


Figure 9.2: Brillouin zone of BaFe_2As_2 in the tetragonal phase. The presented ARPES data are focused around the Γ and around the X point.^[40]

One key to understanding the superconducting mechanism in the Fe-based superconductors, however, is to understand their normal-state properties, since the superconducting state arises from it and the microscopic interactions of the normal-state are considered to be responsible for the superconducting state.

One of the most direct methods to study the electronic structure of solids is the Angle Resolved Photoemission Spectroscopy (ARPES). Recent improvement of energy and angular resolution has made ARPES a highly advanced spectroscopic

method that allows the direct experimental study of the momentum-dependent electronic band structure of solids.

The very idea of this technique is based on the application of the photoelectric effect. When monochromatic light of known energy is incident on a sample surface an electron can absorb a photon and escape from the material with a maximum kinetic energy

$$E_B = h\nu - E_{\text{kin}} - \Phi \quad (9.1)$$

where ν is the photon frequency and Φ the material work function. Such an electron is called a *photoelectron*. By analyzing the kinetic energies of the emitted electrons one can gather information about the energy distribution of the electronic states in the studied material. Additionally, measurements of such distributions for the various emission angles provide information on the electron's momentum. As the parallel component of the electron's momentum is conserved during the photoemission process, ARPES is especially attractive in application to quasi-2D materials since in this case direct and complete experimental determination of the band structure becomes possible.

9.2 ARPES Experiment

For ARPES studies crystals of BaFe_2As_2 grown out of a Sn flux were sent to Prof. Dr. J. Fink and his group at the Helmholtz-Zentrum Berlin/ IFW Dresden. They performed high resolution angle-resolved photoemission spectroscopy at the BESSY synchrotron radiation facility. For information concerning the experimental details refer to the literature^[39,40] and references therein. Many other groups performed ARPES measurements before in order to study the electronic structure of the iron arsenide parent compounds and their related superconductors.^[139-143] The large number of ARPES measurements of the same

compound is not surprising, considering that for such experiments the thin platelike crystals have to be cleaved *in situ* in an ultrahigh-vacuum and the atoms bound to the resulting surface measured afterwards are not necessarily the same for different experiments. Consequently, the results from ARPES measurements often vary between different experiments. The focus of the study performed by Fink *et al.* was on possible differences between the electronic structure in the paramagnetic tetragonal state and in the antiferromagnetic orthorhombic state of BaFe_2As_2 by performing temperature dependent measurements. This is an interesting issue since the sudden decrease in the resistivity below the Néel temperature seen in transport data may indicate that a change occurs in the electronic structure. A change in the band structure is also predicted from DFT calculations.^[144-147]

Beside different temperatures, Fink and coworkers used different polarizations of the photons in order to obtain information about the orbital character of the bands close to the Fermi level. Additionally, using variable photon energies available from the synchrotron radiation source provides information relevant to the k_z values sampled in the measurements, and also facilitates an initial examination of the dispersion of the bands perpendicular to the FeAs planes. The experimental results were finally compared with previously performed DFT band structure calculations.

Figure 9.3 shows a comparison of the momentum distribution maps at the Fermi energy of BaFe_2As_2 at 300 K and 20 K in comparison with the calculated energy contours.

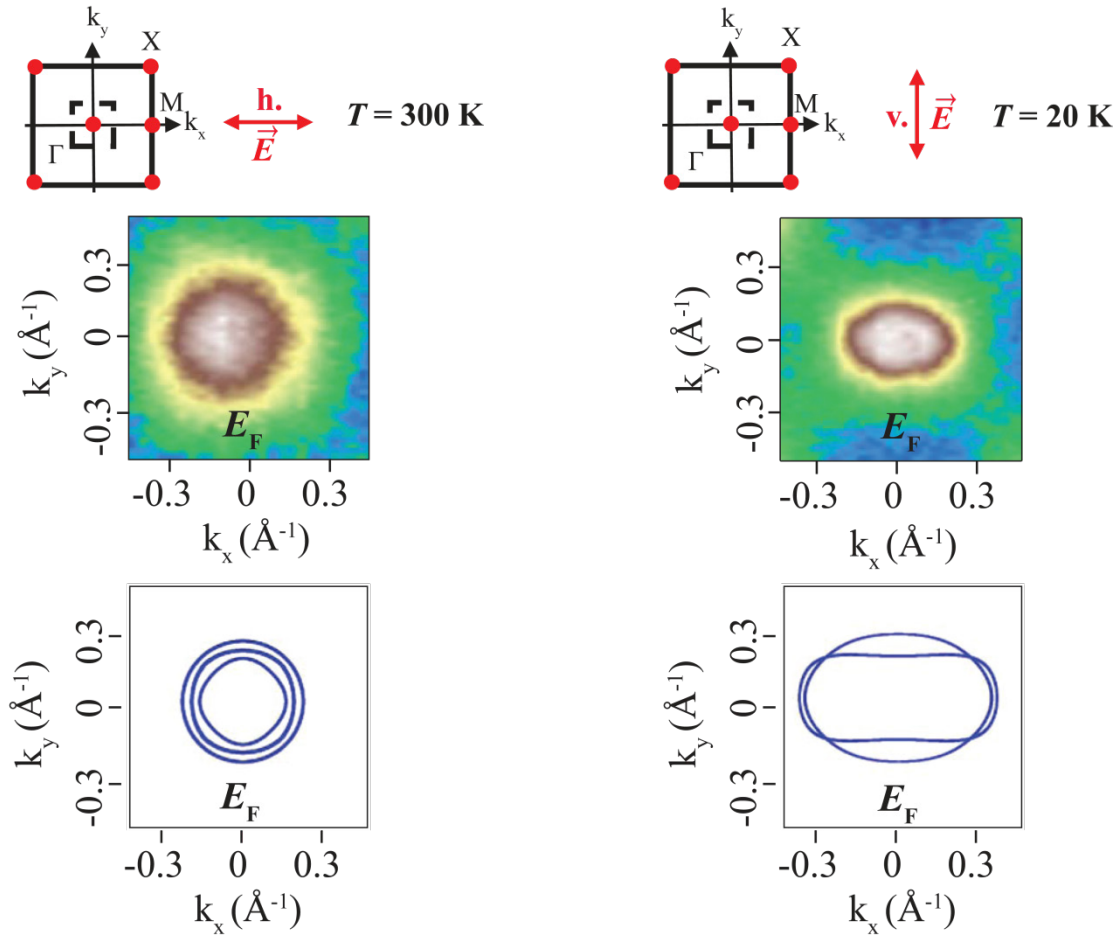


Figure 9.3: Experimental (middle row) and theoretical (lower row) momentum distribution around the center of the Brillouin zone (Γ point) of BaFe_2As_2 at the Fermi energy at 300 K and 20 K. The top line shows the two-dimensional Brillouin zone together with the scanning range (dashed line). It also gives the polarization of the photons (vertical v . (right)) and (horizontal h . (left)) and the temperature.^[40]

In both momentum distribution maps an almost circular Fermi surface is realized. With increasing binding energy the diameter of the Fermi surface increases as well, which indicates that this Fermi surface is caused by a hole pocket centered at the Γ point.

No significant changes could be resolved between the two phases, indicating that the real difference between the paramagnetic tetragonal state and the antiferromagnetic orthorhombic state is probably much smaller than predicted by

spin-dependent DFT band calculations. This is a fact that supports a more itinerant character for the Fe 3d conduction electrons. In general, reasonable qualitative agreement between the band structure calculations for the paramagnetic state and the ARPES data has been observed, although in a number of points a direct assignment of the experimental photoemission intensity distributions to individual bands/ Fermi surfaces is not without a residual level of ambiguity. Nevertheless, with these measurements a new piece of the puzzle falls into the place that probably helps to disclose the secret of the mechanism of high- T_C superconductivity in these systems.

10 Summary and Outlook

This thesis provides a detailed look on the synthesis, structural features and physical properties of iron arsenides. Especially the properties of BaFe_2As_2 and the solid solutions $(\text{Ba}_{1-x}\text{K}_x)\text{Fe}_2\text{As}_2$, $(\text{Ba}_{1-x}\text{Sr}_x)\text{Fe}_2\text{As}_2$ and $\text{BaFe}_2(\text{As}_{1-x}\text{P}_x)_2$ which were all synthesized by solid state reactions by heating mixtures of the elements, were intensively investigated. A brief summary of the key results presented in this work is given below.

BaFe₂As₂

The ternary iron arsenide crystallizes in the tetragonal ThCr_2Si_2 -type structure with two formula units per unit cell (space group $I4/mmm$, $a = 396.25(1)$ pm, $c = 1301.68(3)$ pm). In this compound iron atoms are coordinated tetrahedrally by four arsenic atoms and form two-dimensional layers of edge-shared $\text{FeAs}_{4/4}$ tetrahedra that are perpendicular to $[001]$ and separated by barium atoms. Investigations of the physical properties reveal that BaFe_2As_2 is a poor metal at the verge of a magnetic instability which manifests itself in anomalies like in the electrical resistivity, specific heat and magnetic susceptibility. These anomalies are evoked by an instability of a spin density wave, which leads to a distortion of the tetragonal crystal structure to an orthorhombic structure ($I4/mmm \rightarrow Fmmm$) below 140 K. ^{57}Fe Mössbauer data of BaFe_2As_2 show hyperfine field splitting below 140 K, which hints at antiferromagnetic ordering. This magnetic structure was confirmed by neutron diffraction experiments. The experiments clearly show that BaFe_2As_2 exhibits the same SDW anomaly such as the parent compound LaFeAsO . As the SDW instability is an important prerequisite for high- T_C superconductivity in iron arsenides, BaFe_2As_2 was suggested being a parent

compound for another, oxygen-free class of iron arsenide superconductors with ThCr₂Si₂-type structure.

(Ba_{1-x}K_x)Fe₂As₂

By the substitution of Ba²⁺ for K⁺ the iron arsenide layers are partially oxidized (hole doping) which leads to the suppression of the structural and magnetic transitions in the parent compound BaFe₂As₂ and induces superconductivity. (Ba_{0.6}K_{0.4})Fe₂As₂ shows bulk superconductivity at $T_C = 38$ K and has been the very first member of oxygen-free iron arsenide superconductors. The T_C of 38 K is the highest critical temperature observed in hole doped iron arsenide superconductors so far. These results reveal that hole doping is definitely a possible pathway to induce superconductivity.

In the solid solution (Ba_{1-x}K_x)Fe₂As₂, the main effect of doping on the crystal structure at room temperature is a linear decrease of As–Fe–As bond angles ε and Fe–Fe distances. This is equivalent to an elongation of the FeAs₄ tetrahedra along [001]. The structural changes are intimately coupled to the electronic states at the Fermi level, because the relevant Fe 3d_{x²-y²}-orbitals are strongly affected by the bond angle ε . The tetragonal-to-orthorhombic phase transition ($I4/mmm \rightarrow Fmmm$) of BaFe₂As₂ occurs with decreasing transition temperatures up to a doping level of $x = 0.2$ and is completely suppressed at $x = 0.3$. Superconductivity emerges nearly over the whole doping range in (Ba_{1-x}K_x)Fe₂As₂ (starting at $x \geq 0.1$) with a maximum T_C of 38 K at $x \approx 0.4$. Solely the parent compound BaFe₂As₂ is non-superconducting above 1.8 K. The superconducting transitions in the orthorhombic compounds (Ba_{0.9}K_{0.1})Fe₂As₂ ($T_C \approx 3$ K) and (Ba_{0.8}K_{0.2})Fe₂As₂ ($T_C \approx 25$ K) give strong evidence for the co-existence of superconductivity with the structurally distorted and magnetically ordered state in the BaFe₂As₂ family of iron arsenide superconductors. This underdoped region was therefore intensively investigated by a concerted

approach using a broad spectrum of analytical techniques like X-ray analysis, magnetic investigations, electric resistivity measurements, specific heat and Mössbauer spectroscopy. The ^{57}Fe Mössbauer spectra show temperature dependent superpositions of paramagnetic and antiferromagnetically ordered domains, which reflect small inhomogeneities in the Ba/K distribution. Nevertheless, no distinct phase separation is observed, but a continuous distribution of the potassium concentrations. The Mössbauer spectra of $(\text{Ba}_{0.8}\text{K}_{0.2})\text{Fe}_2\text{As}_2$ shows only one magnetically split Mössbauer signal below T_C (24 K), which supports that superconductivity and magnetism co-exist in these compounds until the optimal doping concentration of $x \geq 0.3$ is achieved. Then, the magnetic and structural phase transitions are completely suppressed and the highest T_C 's are detected.

$(\text{Ba}_{1-x}\text{Sr}_x)\text{Fe}_2\text{As}_2$ and $\text{BaFe}_2(\text{As}_{1-x}\text{P}_x)_2$

As high pressure experiments on BaFe_2As_2 suggest that the effect of structural distortions caused by a simple volume reduction is more important than charge doping for inducing superconductivity, two different approaches to apply “chemical pressure” on BaFe_2As_2 were carried out. A first attempt was the substitution of the Ba^{2+} cation for the smaller Sr^{2+} that led to a compression of the unit cell volume by 6 % which is comparable to the unit cell volume found in high pressure experiments.^[124] The second approach of shrinking the unit cell volume of BaFe_2As_2 was the charge neutral substitution of arsenic for the smaller phosphorus. The volume in $\text{BaFe}_2(\text{As}_{1-x}\text{P}_x)_2$ could be decreased by 10.4 % in total which is almost twice the value reached by high pressure experiments.

Indeed, superconductivity appears by pressure and by P doping within the same volume range as in the high pressure experiments but no superconductivity emerges by Sr doping in $(\text{Ba}_{1-x}\text{Sr}_x)\text{Fe}_2\text{As}_2$, even though the unit cell volumes are within the same range. Superconductivity is absent in $(\text{Ba}_{1-x}\text{Sr}_x)\text{Fe}_2\text{As}_2$ because strontium doping does not suppress the magnetic and structural transition as

SrFe_2As_2 shows the same SDW anomaly as BaFe_2As_2 . Solely the transition temperatures are shifted to higher values. BaFe_2P_2 , however, differs from the properties of BaFe_2As_2 as it is a normal metal and does not show any structural or magnetic transition. Mixed crystals of $\text{BaFe}_2(\text{As}_{1-x}\text{P}_x)_2$ exhibit a different behavior depending on the As : P ratio. At $x \approx 0.3$ the structural and magnetic phase transition is suppressed and superconductivity emerges whereas the curvature of the resistivity for compounds with doping levels higher than $x \approx 0.6$ show a normal metal. No superconductivity could be observed down to 8 K in these compounds. Detailed single crystal investigations of the phosphorus doped $\text{BaFe}_2(\text{As}_{1-x}\text{P}_x)_2$ revealed that subtle details of the crystal structures are crucial to magnetism and superconductivity in the iron arsenides. While in the Sr-doped compounds $(\text{Ba}_{1-x}\text{Sr}_x)\text{Fe}_2\text{As}_2$ arsenic occupies the only possible $(0,0,z_{\text{As}})$ position, the pnictides, arsenic and phosphorus in $\text{BaFe}_2(\text{As}_{1-x}\text{P}_x)_2$ are statistically distributed but located at different coordinates z_{As} and z_{P} . This is necessary to obtain reasonable Fe–P and Fe–As bond lengths. The latter contract strongly at low doping during magnetism is suppressed ($0 \leq x \leq 0.25$). At higher doping levels the Fe–As atomic distance converges to 236 pm (cf. 240.3 pm in BaFe_2As_2) while the Fe–P bond lengths remain close to the values of the pure BaFe_2P_2 (≈ 226 pm).

Interestingly, a comparable shortening of the Fe–As bond length was recently observed in undoped BaFe_2As_2 under pressure,^[133] and might explain the occurrence of superconductivity induced by external pressure even better than for the reason of a simple pressure-volume effect. Thus, these results show clearly that “chemical pressure” is an oversimplified view, which is unsuitable to explain the different behavior of charge neutrally doped $(\text{Ba}_{1-x}\text{Sr}_x)\text{Fe}_2\text{As}_2$ and $\text{BaFe}_2(\text{As}_{1-x}\text{P}_x)_2$.

One of the most remarkable facts regarding the 122 compounds is the ability of growing large single crystals out of a flux. At first a tin flux was used, but according to further single crystal investigations a few percent tin were incorporated into BaFe_2As_2 according to $(\text{Ba}_{1-x}\text{Sn}_x)\text{Fe}_2\text{As}_2$ ($x \approx 0.05$) which slightly effects physical properties. Therefore the flux material was changed from tin to FeAs ^[57] (self-flux method) which is currently the best method to obtain single crystals of the iron arsenide compounds. The relatively easy access to large single crystals caused the shifting of attention from the 1111 to the 122 compounds, as this allows a more definitive characterization of the properties. One of the methods requiring large high quality single crystals is the Angle Resolved Photoemission Spectroscopy (ARPES) which was also performed on BaFe_2As_2 . The temperature dependent ARPES measurements were carried out to examine the electronic structure of the tetragonal and the orthorhombic phase. For the paramagnetic state a reasonable qualitative agreement between the band structure calculations and the ARPES data has been observed. Compared to the orthorhombic phase, however, ARPES measurements showed that no significant changes could be resolved between the tetragonal and orthorhombic phases. This indicates that the real difference between the paramagnetic tetragonal state and the antiferromagnetic orthorhombic state are probably much smaller than those predicted by spin dependent DFT band calculations.

With the results described in the present thesis, a new family of superconducting iron arsenides was established, where BaFe_2As_2 is the most investigated compound so far. The discovery of superconductivity especially in the 122 compounds led scientists to perform hundreds of experiments to raise T_C in the ternary iron arsenides $E\text{Fe}_2\text{As}_2$ ($E\text{A} = \text{Ba}, \text{Sr}, \text{Ca}$) or EuFe_2As_2 . In this regard, all possibilities were exhausted in the form of hole doping,^[80,82-84,89] electron doping,^[118,148,149] isoelectronic doping^[126,128,129,150,151] and also by applying

Summary and Outlook

external pressure,^[120,124] which resulted in dozens of new, superconducting compounds. As no higher T_C 's were detected at first, researchers started to search thereon for new materials that consist of the two-dimensional iron arsenide layers. Only recently a T_C higher than 38 K was reported for the 122 compounds by Guo *et al.*^[152] which is 48.3 K in $\text{EuFe}_2(\text{As}_{0.7}\text{P}_{0.3})$ at ≈ 9 GPa.

In these days the iron arsenides include other, partially, well-known but reinvented, structural families such as the “111” (e.g. LiFeAs , $T_C = 18$ K)^[153] and the “11” compounds (e.g. FeSe , $T_C = 8$ K)^[154,155] which are depicted in Figure 10.1. Each of these structures have tetragonal symmetry at room temperature and are based on a square lattice of iron atoms, which are tetrahedrally coordinated either by arsenic, phosphorus, selenium or tellurium anions. These tetrahedra form two-dimensional layers of edge-shared tetrahedra that are either simply stacked together as in e.g. FeSe ^[154] or separated by layers of alkali (e.g. NaFeAs),^[156] alkaline earth (e.g. BaFe_2As_2),^[16] rare earth oxide (e.g. LaFeAsO)^[12] or rare earth fluoride (e.g. SrFeAsF).^[112] Besides these structural relatively simple compounds a few other structure classes were discovered (e.g. “32522”^[157,158] or the “21311”^[159,160] phases) which structures and properties are more complicated and not further described in this thesis.

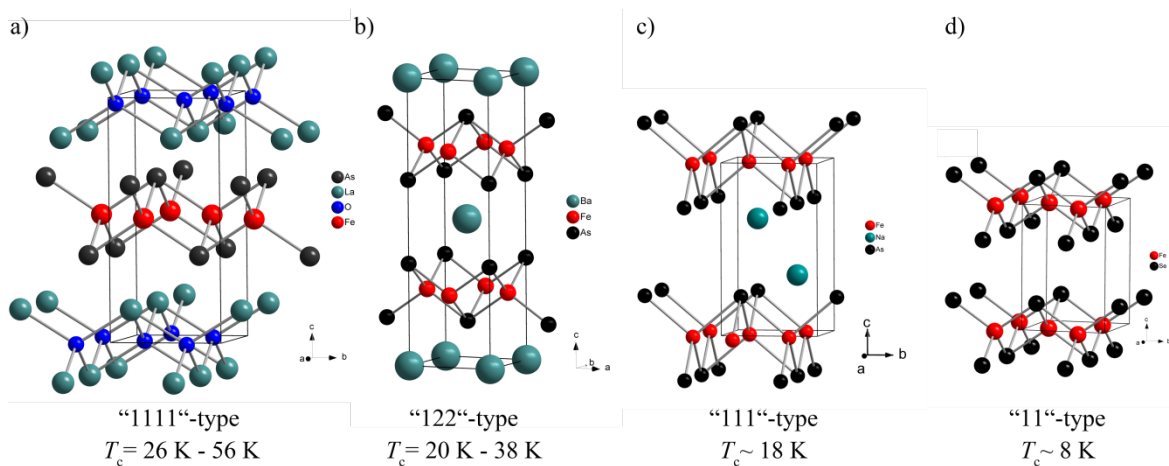


Figure 10.1: Comparison of the crystal structures of a) LaFeAsO (“1111”), b) BaFe_2As_2 (“122”), c) NaFeAs (“111”) and d) FeSe (“11”).

Outlook

The discovery of high-temperature superconductivity in the iron arsenides has led to a new “gold rush” in superconductivity research. This is clearly reflected in the huge number of papers submitted to the arXiv-server, the pre-print server of the Cornell University Library, since the spring of 2008. The enormous interest and expectations that scientist have regarding these compounds manifests itself additionally in the appearance of dozens of review articles and the organization of many conferences worldwide. More than 20 years after the first class of high- T_C superconductors was discovered, many questions remain unanswered on the high-temperature superconducting mechanism. Here, scientists hope that these new high- T_C compounds might provide responses to finally solve the mystery of high temperature superconductivity. But there is still a lot to be done. One of the most interesting facts among these compounds is the ability to obtain large single crystals that allow a better characterization of the physical properties. Such single crystals are currently grown out of the FeAs flux which is up to now the best method since other flux materials such as tin are incorporated or cannot be removed without affecting the single crystals. But also this method holds difficulties with a potential contamination of the crystals by inclusions of the binary iron arsenide. Additionally, for the single crystal growth of the alkaline doped compounds such as $(\text{Ba}_{1-x}\text{K}_x)\text{Fe}_2\text{As}_2$ the potassium concentration is hardly controlled and the widely used “high quality” crystals have a certain inhomogeneous rather than a homogeneous potassium distribution. Thus, the growth of homogeneous high quality single crystals of $(\text{Ba}_{1-x}\text{K}_x)\text{Fe}_2\text{As}_2$ requires further experimental efforts in the near future. Further, also the synthesis of phase pure powder samples form a challenge. Even if the compounds can easily be synthesized, nearly all samples show certain contents of impurity phases such as FeAs, FeAs_2 or Fe_2P . Additionally, the very high vapor pressure of the used potassium leads always to some loss of the alkaline metal. As this loss is difficult to quantify and to control in particular, the synthesis of the

K-doped compounds is usually carried out using a small excess of the alkaline metal and results in approximately the composition desired. For a more precise synthesis additional experiments have to be carried out to further optimize the synthesis conditions. One important approach could be a further reduction of the gas volume, for instance, by synthesizing these compounds in a closed container to minimize the loss of the alkaline metal by evaporation.

Another important issue among these materials is the co-existence of superconductivity and magnetism in the underdoped region. Nandi *et al.*^[161] reported a “reentrant” tetragonal structure in underdoped $\text{Ba}(\text{Fe}_{1-x}\text{Co}_x)_2\text{As}_2$ when superconductivity emerges and propose that this phenomenon is a consequence of a strong competition between itinerant magnetism and superconductivity for the same electrons. The suppression of the orthorhombicity below T_C in $(\text{Ba}_{1-x}\text{K}_x)\text{Fe}_2\text{As}_2$ is currently investigated by Erwin Wiesenmayer^[162] and all signs are that this phenomenon exists also in these compounds. However, the degree of suppression seems to be smaller and saturates at a certain level. The final consequence of this phenomenon for the underlying physics is still not clear and is currently discussed.

Although there are still many questions among these materials, scientists have already begun to start research on possible applications of the iron arsenides. Especially the occurrence of nearly isotropic superconductivity in $(\text{Ba}_{1-x}\text{K}_x)\text{Fe}_2\text{As}_2$ and the huge upper critical fields up to 60 T^[163] make this compound very promising for future applications in high magnetic fields. To apply them to superconductor devices such as Josephson device and SQUIDS, the growth of high-quality epitaxial films is essential. To date, the first films were already fabricated by molecular beam epitaxy method or pulsed laser deposition technique^[164,165] and although there are some difficulties to overcome such as the problems with the high volatility of potassium, the first steps are done to get these materials ready for future applications.

11 Appendix

Table 11.1: Fitting parameters of the ^{57}Fe Mössbauer-spectroscopic measurements of BaFe_2As_2 , $(\text{Ba}_{0.9}\text{K}_{0.1})\text{Fe}_2\text{As}_2$, $(\text{Ba}_{0.8}\text{K}_{0.2})\text{Fe}_2\text{As}_2$ and KFe_2As_2 at different temperatures. Numbers in parantheses are the statistical errors in the last digit. Values without standard deviations were kept fixed during the fitting procedure. (δ), isomer shift; (Γ), experimental line width; (ΔE_Q), quadrupole splitting parameter, (B_{hf}), magnetic hyperfine field. A_1/A_2 is the ratio of the signals.

BaFe₂As₂				
T (K)	δ (mm s ⁻¹)	ΔE_{Q1} (mm s ⁻¹)	Γ_1 (mm s ⁻¹)	B_{hf} (T)
298	0.31(1)	0.00(1)	0.32(1)	-
155	0.40(1)	0.06(22)	0.46(1)	0.37(58)
145	0.41(1)	-0.02(1)	0.30	1.79(9)
140	0.40(1)	-0.02(1)	0.39(4)	3.80(7)
138	0.40(1)	-0.02(1)	0.33(3)	3.93(4)
136	0.40(1)	-0.03(1)	0.32(2)	4.12(3)
134	0.40(1)	-0.02(1)	0.40(4)	4.16(3)
132	0.41(1)	-0.03(1)	0.38(3)	4.31(3)
130	0.41(1)	-0.02(1)	0.46(6)	4.37(2)
125	0.41(1)	-0.03(1)	0.48(6)	4.62(2)
110	0.42(1)	-0.02(1)	0.47(7)	5.16(1)
77	0.43(1)	-0.03(1)	0.33(2)	5.23(1)
4.2	0.44(1)	-0.04(1)	0.25(1)	5.47(1)

Appendix

(Ba_{0.9}K_{0.1})Fe₂As₂

T (K)	δ_1 (mm s ⁻¹)	ΔE_{Q1} (mm s ⁻¹)	Γ_1 (mm s ⁻¹)	B_{hf} (T)	δ_2	ΔE_{Q2} (mm s ⁻¹)	Γ_2 (mm s ⁻¹)	A_1/A_2 (mm s ⁻¹)
298					0.30(1)	-0.06(1)	0.28(1)	
160					0.40(1)	-0.04(2)	0.32(1)	
148	0.38(1)	-0.06(2)	0.32	3.32(8)	0.40(1)	-	0.30	28:72
146	0.41(1)	-0.02(1)	0.32	3.46(3)	0.39(1)	-	0.30	34:66
144	0.39(1)	-0.02(1)	0.32(1)	3.52(5)	0.39(1)	-	0.30	46:54
142	0.40(1)	-0.03(1)	0.33(1)	3.64(2)	0.40(1)	-	0.30	66:34
141	0.39(1)	-0.01(1)	0.30(1)	3.61(2)	0.39(1)	-	0.30	71:29
138	0.39(1)	-0.03(1)	0.39(1)	3.78(2)	0.38(1)	-	0.30	91:9
136	0.40(1)	-0.02(1)	0.37(1)	3.91(3)	0.38(1)	-	0.30	96:4
124	0.40(1)	-0.03(1)	0.29(1)	4.58(1)				
120	0.40(1)	-0.03(1)	0.28(1)	4.65(1)				
118	0.41(1)	-0.03(1)	0.29(1)	4.72(1)				
116	0.41(1)	-0.03(1)	0.28(1)	4.77(1)				
114	0.41(1)	-0.03(1)	0.28(1)	4.79(1)				
112	0.41(1)	-0.02(1)	0.28(1)	4.81(1)				
110	0.41(1)	-0.02(1)	0.27(1)	4.86(1)				
77	0.42(1)	-0.03(1)	0.27(1)	5.22(1)				
50	0.44(1)	-0.03(1)	0.31(1)	5.46(2)				
30	0.45(1)	-0.04(1)	0.36(1)	5.55(2)				
4.2	0.44(1)	-0.04(1)	0.36(1)	5.57(2)				

(Ba_{0.8}K_{0.2})Fe₂As₂								
T (K)	δ_1 (mm s ⁻¹)	ΔE_{Q1} (mm s ⁻¹)	Γ_1 (mm s ⁻¹)	B_{hf} (T)	δ_2	ΔE_{Q2} (mm s ⁻¹)	Γ_2 (mm s ⁻¹)	A_1/A_2 (mm s ⁻¹)
298					0.30(1)	-0.09(1)	0.28(1)	
130					0.39(1)	0.00(1)	0.34(1)	
110	0.42(1)	-0.02(1)	0.26(2)	3.54(7)	0.39(1)	-	0.33	37:63
108	0.40(1)	-0.03(1)	0.28(2)	3.54(6)	0.41(1)	-	0.33	45:55
106	0.40(1)	-0.03(1)	0.29(2)	3.61(6)	0.41(1)	-	0.33	52:48
104	0.40(1)	-0.02(1)	0.30(2)	3.46(5)	0.40(1)	-	0.33	61:39
102	0.40(1)	-0.02(1)	0.30(2)	3.46(4)	0.40(1)	-	0.33	72:28
100	0.39(1)	-0.02(1)	0.29(1)	3.57(3)	0.40(1)	-	0.33	79:21
98	0.40(1)	-0.02(1)	0.29(1)	3.61(1)	0.39(1)	-	0.33	90:10
96	0.40(1)	-0.02(1)	0.28(1)	3.65(2)	0.37(1)	-	0.33	96:4
94	0.40(1)	-0.02(1)	0.27(3)	3.72(4)				
77	0.41(1)	-0.02(1)	0.29(3)	4.25(2)				
50	0.43(1)	-0.03(1)	0.33(4)	4.85(1)				
30	0.43(1)	-0.04(1)	0.30	5.07(3)				
4.2	0.43(1)	-0.04(1)	0.31(3)	5.07(2)				

KFe₂As₂								
T (K)	δ_1 (mm s ⁻¹)	ΔE_{Q1} (mm s ⁻¹)	Γ_1 (mm s ⁻¹)	B_{hf} (T)	δ_2	ΔE_{Q2} (mm s ⁻¹)	Γ_2 (mm s ⁻¹)	A_1/A_2 (mm s ⁻¹)
298	0.21(1)	-0.03(11)	0.39(1)					
77	0.33(1)	-0.08(1)	0.33					
4.2	0.34(1)	-0.09(4)	0.40(2)					

Table 11.2: Fitting parameters of the ⁵⁷Mössbauer spectroscopic measurements of (Ba_{0.8}K_{0.2})Fe₂As₂ and (Ba_{0.7}K_{0.3})Fe₂As₂ at 4.2 K

	T (K)	δ_1 (mm s ⁻¹)	ΔE_{Q1} (mm s ⁻¹)	Γ_1 (mm s ⁻¹)
(Ba _{0.7} K _{0.3})Fe ₂ As ₂	4.2	0.41(1)	-0.02	0.47(1)
(Ba _{0.8} K _{0.2})Fe ₂ As ₂	4.2	0.39(1)	-0.10(1)	0.35(1)

Abbreviations

Abbreviation	Expression/Word
\emptyset	Diameter
\AA	Ångström
<i>A</i>	Alkaline
λ	Wave Length
μ_B	Effective Bohr Magneton
δ	Isomer Shift
Γ	Experimental Line Width
Θ_D	Debye Temperature
γ	Sommerfeld Coefficient
χ	Susceptibility
°	Degree
a.u.	Arbitrary Units
<i>ac</i>	“Alternating Current”
B_{hf}	Magnetic Hyperfine Field
cf.	Confer
C_p	Specific Heat
deg	Degree
DFT	Density Functional Theory
<i>dc</i>	“Direct Current”
<i>EA</i>	Alkaline Earth
ΔE_Q	Quadrupole Splitting Parameter
EDX	Energy Dispersive X-Ray Analysis
et al.	Et alii
FWHM	Full Width at Half Maximum
FC	Field Cooled
GPa	Giga Pascal
h	Hour

ICP-AAS	Inductively Coupled Plasma – Atomic Absorption Spectrometry
IPDS	Imaging Plate Diffraction System
K	Kelvin
mg	Milligram
<i>M</i>	Magnetization
MPMS	“Magnetic Property Measurement System”
Oe	Ørsted
pm	Picometer
<i>Pn</i>	Pnictide
PPMS	“Physical Property Measurement System”
q	Magnetic wave vector
<i>RE</i>	Rare Earth
<i>RRR</i>	Relative Resistance Ratio
rt	Room Temperature
s	Second
SDW	Spin Density Wave
SEM	Scanning Electron Microscope
SOF	Site Occupation Factor
SQUID	“Superconducting Quantum Interference Device”
μSR	Muon Spin Resonance
T	Tesla
<i>T_C</i>	Critical Temperature
<i>T_N</i>	Néel Temperature
<i>T_o</i>	Temperature when orthorhombic distortion occurs
<i>T_{ons}</i>	Onset Temperature
<i>T_{SDW}</i>	Temperature when Spin Density Wave Anomaly occurs
V	Volume
Wt%	Weight Percent
Z	Formula Units
ZFC	Zero Field Cooled

Full List of Publications

Major results of this thesis were published in scientific journals. In the following list publications which deal with the results discussed above are marked with an asterisk.

1.* Spin density wave anomaly at 140 K in the ternary iron arsenide BaFe_2As_2

M. Rotter, M. Tegel and D. Johrendt, *Phys. Rev. B: Cond. Matter Mater.* **2008**, 78, 020503.

2.* Superconductivity at 38 K in the iron arsenide $(\text{Ba}_{1-x}\text{K}_x)\text{Fe}_2\text{As}_2$

M. Rotter, M. Tegel, D. Johrendt, *Phys. Rev. Lett.* **2008**, 101, 107006.

3. Structural and magnetic phase transitions in the ternary iron arsenides SrFe_2As_2 and EuFe_2As_2

M. Tegel, M. Rotter, V. Weiss, F. M. Schappacher, R. Pöttgen, D. Johrendt, *J. Phys.: Cond Mat.* **2008**, 20, 452201.

4. Inelastic neutron scattering and lattice dynamical calculations in BaFe_2As_2

R. Mittal, Y. Su, S. Rols, T. Chatterji, S. L. Chaplot, H. Schober, M. Rotter, D. Johrendt, Th. Brückel, *Phys. Rev. B: Cond. Matter Mater.* **2008**, 78, 104514.

5.* Superconductivity and Crystal Structures of $(\text{Ba}_{1-x}\text{K}_x)\text{Fe}_2\text{As}_2$ ($x = 0 - 1$)

M. Rotter, M. Pangerl, M. Tegel, D. Johrendt, *Angew. Chem.* **2008**, *120*, 8067;
Angew. Chem. Int. Ed. **2008**, *47*, 7949.

6.* Competition of magnetism and superconductivity in underdoped

$(\text{Ba}_{1-x}\text{K}_x)\text{Fe}_2\text{As}_2$

M. Rotter, M. Tegel, I. Schellenberg, F. M. Schappacher, R. Pöttgen, J. Deisenhofer, A. Günther, F. Schrettle, A. Loidl, D. Johrendt, *New J. Phys.* **2009**, *11*, 025014.

7. Ab initio lattice dynamics simulations and inelastic neutron scattering spectra for studying phonons in BaFe_2As_2 : Effect of structural phase transition, structural relaxation and magnetic ordering

M. Zbiri, H. Schober, M. R. Johnson, S. Rols, R. Mittal, Y. Su, M. Rotter, D. Johrendt, *Phys. Rev. B: Cond. Matter Mater.* **2009**, *79*, 064511.

8.* Antiferromagnetic ordering and structural phase transition in BaFe_2As_2 with Sn incorporated from the growth flux

Y. Su, P. Link, A. Schneidewind, Th. Wolf, Y. Xiao, R. Mittal, M. Rotter, D. Johrendt, Th. Brückel, M. Loewenhaupt, *Phys. Rev. B: Cond. Matter Mater.* **2009**, *79*, 064504.

9.* Electronic structure studies of BaFe₂As₂ by angle-resolved photoemission spectroscopy

J. Fink, S. Thirupathaiyah, R. Ovsyannikov, H. A. Dürr, R. Follath, Y. Huang, S. de Jong, M. S. Golden, Y.-Z. Zhang, H. O. Jeschke, R. Valenti, C. Felser, S. D. Farahani, M. Rotter, and D. Johrendt. *Phys. Rev. B: Cond. Matter Mater.* **2009**, 79, 15518.

10.* Magnetic and superconducting transitions in (Ba_{1-x}K_x)Fe₂As₂ studied by specific heat

Ch. Kant, J. Deisenhofer, A. Guenther, F. Schrettle, A. Loidl, M. Rotter, D. Johrendt. *Phys. Rev. B: Cond. Matter Mater.* **2010**, 81, 014529.

11.* Different response of the crystal structure to isoelectronic doping in BaFe₂(As_{1-x}P_x)₂ and (Ba_{1-x}Sr_x)Fe₂As₂

M. Rotter, C. Hieke and D. Johrendt, *Phys. Rev. B: Cond. Matter Mater.* **2010**, 82, 014513.

12. The Structure of δ-PdCl₂ and γ-PdCl₂: Phases with Negative Thermal Expansion in One Direction

J. Evers, W. Beck, M. Göbel, S. Jakob, P. Mayer, G. Oehlinger, M. Rotter, T. M. Klapötke, *Angew. Chem.* **2010**, 122, 5812; *Angew. Chem. Int. Ed.* **2010**, 49, 5677.

Conference contributions

M. Rotter, D. Johrendt

Substitutionen in BaFe_2As_2 (talk)

Festkörper-Seminar Hirschegg, Hirschegg (Austria), 11/06 – 14/06/09.

M. Rotter, M. Tegel, I. Schellenberg, F. M. Schappacher, R. Pöttgen, D. Johrendt

Competition of magnetism in superconductivity in underdoped $(\text{Ba}_{1-x}\text{K}_x)\text{Fe}_2\text{As}_2$ (Poster)

Workshop "Properties of high temperature superconductors",

Munich, 13/04 – 16/04/10.

12 Curriculum vitae

Personal Details

16/02/1982 Born in Fort Sill / Oklahoma (USA)

Citizenship: German, U.S.

Marital status: married

Education

since 03/2008 PhD thesis in inorganic solid-state chemistry in the group of Prof. Dr. D. Johrendt. Department of Chemistry at the Ludwig-Maximilians-Universität München; PhD thesis entiteled: “*High-Temperature Superconductivity in Doped BaFe₂As₂*”

12/2008 Römer-Award (Dr. Klaus Römer-Foundation)

11/2007 Master’s thesis in the group of Prof. Dr. D. Johrendt, Ludwig-Maximilians-Universität München:
“*Untersuchungen zur Darstellung von Oxidgermaniden und Oxidchalkogeniden der Seltenerdelemente*“

10/2001 –11/2007 Bachelor/Master studies at the Ludwig-Maximilians-Universität München

06/2001 Abitur at the Gymnasium Puchheim

1992 – 2001 Secondary education: Gymnasium Puchheim

1988 – 1992 Primary school education: Grundschule am Gernerplatz, Puchheim

13 Bibliography

- [1] B. T. Matthias, T. H. Geballe, R. H. Willens, E. Corenzwit, G. W. Hull, Jr., *Phys. Rev. A: At., Mol., Opt. Phys.* **1965**, 139, 1501.
- [2] J. G. Bednorz, K. A. Müller, *Z. Phys. B: Condens. Matter* **1986**, 64, 189.
- [3] M. K. Wu, J. R. Ashburn, C. J. Torng, P. H. Hor, R. L. Meng, L. Gao, Z. J. Huang, Y. Q. Wang, C. W. Chu, *Phys. Rev. Lett.* **1987**, 58, 908.
- [4] A. Schilling, M. Cantoni, J. D. Guo, H. R. Ott, *Nature (London, U. K.)* **1993**, 363, 56.
- [5] R. Chevrel, M. Hirrien, M. Sergent, *Polyhedron* **1986**, 5, 87.
- [6] R. J. Cava, H. Takagi, B. Batlogg, H. W. Zandbergen, J. J. Krajewski, W. F. Peck, Jr., R. B. van Dover, R. J. Felder, T. Siegrist, et al., *Nature (London, U. K.)* **1994**, 367, 146.
- [7] J. Nagamatsu, N. Nakagawa, T. Muranaka, Y. Zenitani, J. Akimitsu, *Nature (London, U. K.)* **2001**, 410, 63.
- [8] A. Y. Liu, I. I. Mazin, J. Kortus, *Phys. Rev. Lett.* **2001**, 87, 087005.
- [9] Y. Kamihara, T. Watanabe, M. Hirano, H. Hosono, *J. Am. Chem. Soc.* **2008**, 130, 3296.
- [10] Z.-A. Ren, W. Lu, J. Yang, W. Yi, X.-L. Shen, Z.-C. Li, G.-C. Che, X.-L. Dong, L.-L. Sun, F. Zhou, Z.-X. Zhao, *Chin. Phys. Lett.* **2008**, 25, 2215.
- [11] C. Wang, L. Li, S. Chi, Z. Zhu, Z. Ren, Y. Li, Y. Wang, X. Lin, Y. Luo, S. Jiang, X. Xu, G. Cao, Z. Xu, *Europhys. Lett.* **2008**, 83, 67006.
- [12] V. Johnson, W. Jeitschko, *J. Solid State Chem.* **1974**, 11, 161.
- [13] W. Lu, X.-L. Shen, J. Yang, Z.-C. Li, W. Yi, Z.-A. Ren, X.-L. Dong, G.-C. Che, L.-L. Sun, F. Zhou, Z.-X. Zhao, *Solid State Commun.* **2008**, 148, 168.
- [14] H.-H. Wen, G. Mu, L. Fang, H. Yang, X. Zhu, *Europhys. Lett.* **2008**, 82, 17009.
- [15] G. Just, P. Paufler, *J. Alloys Compd.* **1996**, 232, 1.
- [16] M. Pfisterer, G. Nagorsen, *Z. Naturforsch. B: J. Chem. Sci.* **1980**, 35, 703.
- [17] M. Pfisterer, G. Nagorsen, *Z. Naturforsch. B: J. Chem. Sci.* **1983**, 38, 811.
- [18] WINXPOW, 2.12; STOE & Cie GmbH Darmstadt, **2005**.
- [19] M. Tegel, *Dissertation*, Ludwig-Maximilians-Universität **2010**.
- [20] STOE WINXPOW THEO, 2.04; STOE & Cie GmbH **2004**.

- [21] JCPDS, International Center for Diffraction Data, Swathmore, USA **1992**.
- [22] A. C. Larson, R. B. Von Dreele, General Structure Analysis System (GSAS), **2004**.
- [23] A. Coelho, TOPAS-Academic, 4.1; Coelho Software, Brisbane, **2007**.
- [24] A. L. Bail, A. Jouanneaux, *J. Appl. Crystallogr.* **1997**, 30, 265.
- [25] ORIGIN 6.1, 6.1052 (B232), OriginLab Corporation, Northampton, USA, **2000**.
- [26] Y. Amemiya, J. Miyahara, *Nature (London, U. K.)* **1988**, 336, 89.
- [27] BASREADER, Raytest Isotopenmessgeräte GmbH, Straubenhardt.
- [28] TINA, 2.10g; Raytest Isotopenmessgeräte GmbH, Straubenhardt **1993**.
- [29] G. M. Sheldrick, XPREP, *Data Preparation & Reciprocal Space Exploration*, 6.12, Siemens Analytical X-ray instruments,; **1996**.
- [30] STOE X-RED, *STOE Data Reduction Program*; 1.19, STOE & Cie GmbH, Darmstadt, **1999**.
- [31] STOE X-SHAPE, *Crystal Optimization for Numerical Absorption Correction* 1.05, Stoe & Cie GmbH, Darmstadt, **1999**.
- [32] J. Karle, *Angew. Chem.* **1986**, 98, 611; *Angew. Chem. Int. Ed.* **1986**, 25, 614.
- [33] H. Hauptmann, *Angew. Chem.* **1986**, 98, 600; *Angew. Chem. Int. Ed.* **1986**, 25, 603.
- [34] G. M. Sheldrick, SHELXS-97, University of Göttingen, **1997**.
- [35] G. M. Sheldrick, SHELXL-97, University of Göttingen, **1997**.
- [36] G. M. Sheldrick, *Acta Crystallogr., Sect. A: Found. Crystallogr.* **2008**, 64, 112.
- [37] K. Brandenburg, DIAMOND, *Crystal and Molecular Structure Visualization*, 3.1b; Crystal Impact GbR, Bonn, **2005**.
- [38] INCA, Oxford Instruments Analytical Ltd., 4.02, **1998-2002**.
- [39] D. S. Inosov et al., *Phys. Rev. B* **2008**, 77, 212504.
- [40] J. Fink et al., *Phys. Rev. B* **2009**, 79, 155118.
- [41] C. Kranenberg, LEITMESS, 2.5, Heinrich-Heine-Universität, Düsseldorf, **1998**.
- [42] Y. Kamihara, H. Hiramatsu, M. Hirano, R. Kawamura, H. Yanagi, T. Kamiya, H. Hosono, *J. Am. Chem. Soc.* **2006**, 128, 10012.

Bibliography

- [43] T. Watanabe, H. Yanagi, T. Kamiya, Y. Kamihara, H. Hiramatsu, M. Hirano, H. Hosono, *Inorg. Chem.* **2007**, *46*, 7719.
- [44] M. Tegel, D. Bichler, D. Johrendt, *Solid State Sci.* **2008**, *10*, 193.
- [45] Z.-A. Ren, G.-C. Che, X.-L. Dong, J. Yang, W. Lu, W. Yi, X.-L. Shen, Z.-C. Li, L.-L. Sun, F. Zhou, Z.-X. Zhao, *Europhys. Lett.* **2008**, *83*, 17002.
- [46] J. Dong, H. J. Zhang, G. Xu, Z. Li, G. Li, W. Z. Hu, D. Wu, G. F. Chen, X. Dai, J. L. Luo, Z. Fang, N. L. Wang, *Europhys. Lett.* **2008**, *83*, 27006.
- [47] G. F. Chen, Z. Li, D. Wu, G. Li, W. Z. Hu, J. Dong, P. Zheng, J. L. Luo, N. L. Wang, *Phys. Rev. Lett.* **2008**, *100*, 247002.
- [48] E. Fawcett, *Rev. Mod. Phys.* **1988**, *60*, 209.
- [49] R. N. Shelton, H. F. Braun, E. Musick, *Solid State Commun.* **1984**, *52*, 797.
- [50] M. Francois, G. Venturini, J. F. Mareche, B. Malaman, B. Roques, *J. Less-Common Met.* **1985**, *113*, 231.
- [51] W. Jeitschko, R. Glaum, L. Boonk, *J. Solid State Chem.* **1987**, *69*, 93.
- [52] M. Hirjak, P. Lejay, B. Chevalier, J. Etourneau, P. Hagenmuller, *J. Less-Common Met.* **1985**, *105*, 139.
- [53] T. Mine, H. Yanagi, T. Kamiya, Y. Kamihara, M. Hirano, H. Hosono, *Solid State Commun.* **2008**, *147*, 111.
- [54] C. Enss, S. Hunklinger, *Low-Temperature Physics*, Springer-Verlag Berlin Heidelberg, **2005**.
- [55] S. D. Wilson, Z. Yamani, C. R. Rotundu, B. Freelon, E. Bourret-Courchesne, R. J. Birgeneau, *Phys. Rev. B: Condens. Matter Mater. Phys.* **2009**, *79*, 184519.
- [56] F. J. Blatt, *Physics of Electronic Conduction in Solids*, (McGraw-Hill, New York, 1968).
- [57] X. F. Wang, T. Wu, G. Wu, H. Chen, Y. L. Xie, J. J. Ying, Y. J. Yan, R. H. Liu, X. H. Chen, *Phys. Rev. Lett.* **2009**, *102*, 117005.
- [58] S. Kitao, Y. Kobayashi, S. Higashitaniguchi, M. Saito, Y. Kamihara, M. Hirano, T. Mitsui, H. Hosono, M. Seto, *J. Phys. Soc. Jpn.* **2008**, *77*, 103706.
- [59] H. H. Klauss, H. Luetkens, R. Klingeler, C. Hess, F. J. Litterst, M. Kraken, M. M. Korshunov, I. Eremin, S. L. Drechsler, R. Khasanov, A. Amato, J. Hamann-Borrero, N. Leps, A. Kondrat, G. Behr, J. Werner, B. Büchner, *Phys. Rev. Lett.* **2008**, *101*, 077005.
- [60] I. Nowik, I. Felner, V. P. S. Awana, A. Vajpayee, H. Kishan, *J. Phys.: Condens Matter* **2008**, *20*, 292201.

- [61] M. A. McGuire, A. D. Christianson, A. S. Sefat, B. C. Sales, M. D. Lumsden, R. Jin, E. A. Payzant, D. Mandrus, Y. Luan, V. Keppens, V. Varadarajan, J. W. Brill, R. P. Hermann, M. T. Sougrati, F. Grandjean, G. J. Long, *Phys. Rev. B: Condens. Matter Mater. Phys.* **2008**, 78, 094517.
- [62] Q. Huang, Y. Qiu, W. Bao, M. A. Green, J. W. Lynn, Y. C. Gasparovic, T. Wu, G. Wu, X. H. Chen, *Phys. Rev. Lett.* **2008**, 101, 257003.
- [63] Y. Su, P. Link, A. Schneidewind, T. Wolf, P. Adelman, Y. Xiao, M. Meven, R. Mittal, M. Rotter, D. Johrendt, T. Brueckel, M. Loewenhaupt, *Phys. Rev. B: Condens. Matter Mater. Phys.* **2009**, 79, 064504.
- [64] M. Kofu, Y. Qiu, W. Bao, S. H. Lee, S. Chang, T. Wu, G. Wu, X. H. Chen, *New J. Phys.* **2009**, 11, 055001.
- [65] M. Rotter, M. Tegel, I. Schellenberg, W. Hermes, R. Pöttgen, D. Johrendt, *Phys. Rev. B: Condens. Matter Mater. Phys.* **2008**, 78, 020503(R).
- [66] B. Eisenmann, H. Jordan, H. Schafer, *Z. Anorg. Allg. Chem.* **1985**, 530, 74.
- [67] R. Lam, A. Mar, *Solid State Sci.* **2001**, 3, 503.
- [68] P. Eckerlin, W. Kischio, *Z. Anorg. Allg. Chem.* **1968**, 363, 1.
- [69] R. D. Shannon, C. T. Prewitt, *Acta Crystallogr., Sect. B: Struct. Sci.* **1969**, 25, 925.
- [70] N. Ni, S. L. Bud'ko, A. Kreyssig, S. Nandi, G. E. Rustan, A. I. Goldman, S. Gupta, J. D. Corbett, A. Kracher, P. C. Canfield, *Phys. Rev. B: Condens. Matter Mater. Phys.* **2008**, 78, 014507.
- [71] S. H. Baek, T. Klimczuk, F. Ronning, E. D. Bauer, J. D. Thompson, N. J. Curro, *Phys. Rev. B: Condens. Matter Mater. Phys.* **2008**, 78, 212509.
- [72] R. Morinaga, K. Matan, H. S. Suzuki, T. J. Sato, *Jpn. J. Appl. Phys.* **2009**, 48, 013004.
- [73] C. de la Cruz, Q. Huang, J. W. Lynn, J. Li, W. Ratcliff II, J. L. Zarestky, H. A. Mook, G. F. Chen, J. L. Luo, N. L. Wang, P. Dai, *Nature (London, U. K.)* **2008**, 453, 899.
- [74] T. Nomura, S. W. Kim, Y. Kamihara, M. Hirano, P. V. Sushko, K. Kato, M. Takata, A. L. Shluger, H. Hosono, *Supercond. Sci. Technol.* **2008**, 21, 125028.
- [75] Y. Qiu, W. Bao, Q. Huang, T. Yildirim, J. M. Simmons, M. A. Green, J. W. Lynn, Y. C. Gasparovic, J. Li, T. Wu, G. Wu, X. H. Chen, *Phys. Rev. Lett.* **2008**, 101, 257002.
- [76] S. Rosza, H. U. Schuster, *Z. Naturforsch. B: J. Chem. Sci.* **1981**, 36, 1668.
- [77] S. Margadonna, Y. Takabayashi, M. T. McDonald, M. Brunelli, G. Wu, R. H. Liu, X. H. Chen, K. Prassides, *Phys. Rev. B: Condens. Matter Mater. Phys.* **2009**, 79, 014503.

Bibliography

- [78] L. W. Finger, D. E. Cox, A. P. Jephcoat, *J. Appl. Crystallogr.* **1992**, *27*, 79.
- [79] K. Selte, A. Kjekshus, A. F. Andresen, *Acta Chem. Scand.* **1972**, *26*, 3101.
- [80] M. Rotter, M. Tegel, D. Johrendt, *Phys. Rev. Lett.* **2008**, *101*, 107006.
- [81] G. F. Chen, Z. Li, G. Li, W. Z. Hu, J. Dong, X. D. Zhang, P. Zheng, N. L. Wang, J. L. Luo, *Chin. Phys. Lett.* **2008**, *25*, 3403.
- [82] K. Sasmal, B. Lv, B. Lorenz, A. Guloy, F. Chen, Y. Xue, C. W. Chu, *Phys. Rev. Lett.* **2008**, *101*, 107007.
- [83] G. Wu, H. Chen, T. Wu, Y. L. Xie, Y. J. Yan, R. H. Liu, X. F. Wang, J. J. Ying, X. H. Chen, *J. Phys.: Condens. Matter* **2008**, *20*, 422201.
- [84] H. S. Jeevan, Z. Hossain, C. Geibel, P. Gegenwart, *Phys. Rev. B: Condens. Matter Mater. Phys.* **2008**, *78*, 092406.
- [85] H. H. Wen, G. Mu, X. Y. Zhu, P. Cheng, L. Fang, F. Han, B. Zeng, B. Shen, *Phys. C (Amsterdam, Neth.)* **2009**, *469*, 894.
- [86] C. Zheng, R. Hoffmann, *J. Solid State Chem.* **1988**, *72*, 58; *J. Phys. Chem.* **1985**, *89*, 4175.
- [87] D. Johrendt, C. Felser, O. Jepsen, O. K. Andersen, A. Mewis, J. Rouxel, *J. Solid State Chem.* **1997**, *130*, 254.
- [88] H. Luetkens, H. H. Klauss, M. Kraken, F. J. Litterst, T. Dellmann, R. Klingeler, C. Hess, R. Khasanov, A. Amato, C. Baines, M. Kosmala, O. J. Schumann, M. Braden, J. Hamann-Borrero, N. Leps, A. Kondrat, G. Behr, J. Werner, B. Büchner, *Nat. Mater.* **2009**, *8*, 305.
- [89] R. Cortes-Gil, D. R. Parker, M. J. Pitcher, J. Hadermann, S. J. Clarke, *Chem. Mater.* **2010**, *22*, 4304.
- [90] Q. Huang, J. Zhao, J. W. Lynn, G. F. Chen, J. L. Luo, N. L. Wang, P. Dai, *Phys. Rev. B: Condens. Matter Mater. Phys.* **2008**, *78*, 054529.
- [91] J. Zhao, Q. Huang, C. de la Cruz, S. L. Li, J. W. Lynn, Y. Chen, M. A. Green, G. F. Chen, G. Li, Z. Li, J. L. Luo, N. L. Wang, P. C. Dai, *Nature Mater.* **2008**, *7*, 953.
- [92] A. J. Drew, C. Niedermayer, P. J. Baker, F. L. Pratt, S. J. Blundell, T. Lancaster, R. H. Liu, G. Wu, X. H. Chen, I. Watanabe, V. K. Malik, A. Dubroka, M. Rossle, K. W. Kim, C. Baines, C. Bernhard, *Nature Mater.* **2009**, *8*, 310.
- [93] B. Keimer, N. Belk, R. J. Birgeneau, A. Cassanho, C. Y. Chen, M. Greven, M. A. Kastner, A. Aharony, Y. Endoh, R. W. Erwin, G. Shirane, *Phys. Rev. B: Condens. Matter Mater. Phys.* **1992**, *46*, 14034.
- [94] H. Chen, Y. Ren, Y. Qiu, W. Bao, R. H. Liu, G. Wu, T. Wu, Y. L. Xie, X. F. Wang, Q. Huang, X. H. Chen, *Europhys. Lett.* **2009**, *85*, 17006.

- [95] A. A. Aczel, E. Baggio-Saitovitch, S. L. Budko, P.C. Canfield, J. P. Carlo, G. F. Chen, P. Dai, T. Goko, W. Z. Hu, G. M. Luke, J. L. Luo, N. Ni, D. R. Sanchez-Candela, F. F. Tafti, N. L. Wang, T. J. Williams, W. Yu, Y. J. Uemura, *Phys. Rev. B: Condens. Matter Mater. Phys.* **2008**, 78, 214503.
- [96] T. Goko, A. A. Aczel, E. Baggio-Saitovitch, S. L. Bud'ko, P. C. Canfield, J. P. Carlo, G. F. Chen, P. Dai, A. C. Hamann, W. Z. Hu, H. Kageyama, G. M. Luke, J. L. Luo, B. Nachumi, N. Ni, D. Reznik, D. R. Sanchez-Candela, A. T. Savici, K. J. Sikes, N. L. Wang, C. R. Wiebe, T. J. Williams, T. Yamamoto, W. Yu, Y. J. Uemura, *Phys. Rev. B: Condens. Matter Mater. Phys.* **2009**, 80, 024508.
- [97] J. T. Park, D. S. Inosov, Ch. Niedermayer, G. L. Sun, D. Haug, N. B. Christensen, R. Dinnebier, A. V. Boris, A. J. Drew, L. Schulz, T. Shapoval, U. Wolff, V. Neu, X. Yang, C. T. Lin, B. Keimer, V. Hinkov, *Phys. Rev. Lett.* **2009**, 102, 117006.
- [98] E. Bonjour, R. Calemczuk, J. Y. Henry, A. F. Khoder, *Phys. Rev. B: Condens. Matter Mater. Phys.* **1991**, 43, 106.
- [99] U. Welp, R. Xie, A. E. Koshelev, W. K. Kwok, P. Cheng, L. Fang, H. H. Wen, *Phys. Rev. B: Condens. Matter Mater. Phys.* **2008**, 78, 140510.
- [100] U. Welp, R. Xie, A. E. Koshelev, W. K. Kwok, H. Q. Luo, Z. S. Wang, G. Mu, H. H. Wen, *Phys. Rev. B: Condens. Matter Mater. Phys.* **2009**, 79, 094505.
- [101] G. Mu, H. Q. Luo, Z. Wang, L. Shan, C. Ren, H.-H. Wen, *Phys. Rev. B: Condens. Matter Mater. Phys.* **2009**, 79, 174501.
- [102] Z.-S. Wang, H.-Q. Luo, C. Ren, H.-H. Wen, *Phys. Rev. B: Condens. Matter Mater. Phys.* **2008**, 78, 140501.
- [103] H. Q. Yuan, J. Singleton, F. F. Balakirev, S. A. Baily, G. F. Chen, J. L. Luo, N. L. Wang, *Nature* **2009**, 457, 565.
- [104] J. K. Dong, L. Ding, H. Wang, X. F. Wang, T. Wu, G. Wu, X. H. Chen, S. Y. Li, *New J. Phys.* **2008**, 10, 123031.
- [105] M. Rotter, M. Tegel, I. Schellenberg, F. M. Schappacher, R. Pöttgen, J. Deisenhofer, A. Günther, F. Schrettle, A. Loidl, D. Johrendt, *New J. Phys.* **2009**, 11, 025014.
- [106] S. L. Bud'ko, N. Ni, P. C. Canfield, *Phys. Rev. B: Condens. Matter Mater. Phys.* **2009**, 79, 220516.
- [107] C. Kant, J. Deisenhofer, A. Günther, F. Schrettle, A. Loidl, M. Rotter, D. Johrendt, *Phys. Rev. B: Condens. Matter Mater. Phys.* **2010**, 81, 014529.
- [108] D. Gonzalez-Alvarez, F. Grønvold, B. Falk, E. F. Westrum, R. Blachnik, G. Kudermann, *J. Chem. Thermodyn.* **1989**, 21, 363.

Bibliography

- [109] M. Tegel, I. Schellenberg, R. Pöttgen, D. Johrendt, *Z. Naturforsch., B: J. Chem. Sci.* **2008**, *63*, 1057.
- [110] I. Nowik, I. Felner, *J. Supercond. Novel Magn.* **2008**, *21*, 297.
- [111] M. A. McGuire, R. P. Hermann, A. S. Sefat, B. C. Sales, R. Jin, D. Mandrus, F. Grandjean, G J. Long, *New J. Phys.* **2009**, *11*, 025011.
- [112] M. Tegel, S. Johansson, V. Weiss, I. Schellenberg, W. Hermes, R. Pöttgen, D. Johrendt, *Europhys. Lett.* **2008**, *84*, 67007.
- [113] M. Tegel, M. Rotter, V. Weiss, F. Schappacher, R. Pöttgen, D. Johrendt, *J. Phys.: Condens. Matter* **2008**, *20*, 452201.
- [114] H. Raffius, E. Mörsen, B. D. Mosel, W. Müller-Warmuth, W. Jeitschko, L. Terbüchte, T. Vomhof, *J. Phys. Chem. Solids* **1993**, *54*, 135.
- [115] J.-H. Chu, J. G. Analytis, C. Kucharczyk, I. R. Fisher, *Phys. Rev. B: Condens. Matter Mater. Phys.* **2009**, *79*, 014506.
- [116] D. K. Pratt, A. Kreyssig, S. Nandi, N. Ni, A. Thaler, M. D. Lumsden, W. Tian, J. L. Zarestky, S. L. Bud'ko, P. C. Canfield, A. I. Goldman, R. J. McQueeney, *Phys. Rev. B: Condens. Matter Mater. Phys.* **2010**, *81*, 140510.
- [117] M. Rotter, M. Pangerl, M. Tegel, D. Johrendt, *Angew. Chem.* **2008**, *120*, 8067; *Angew. Chem. Int. Ed.*, **2008**, *47*, 7949.
- [118] A. S. Sefat, R. Y. Jin, M. A. McGuire, B. C. Sales, D. J. Singh, D. Mandrus, *Phys. Rev. Lett.* **2008**, *101*, 117004.
- [119] Y. Muraba, S. Matsuishi, S.-W. Kim, T. Atou, O. Fukunaga, H. Hosono, *arXiv:1005.0528v2* **2010**.
- [120] P. L. Alireza, J. Gillett, Y. T. C. Ko, S. E. Sebastian, G. G. Lonzarich, *J. Phys.: Condens. Matter* **2009**, *21*, 012208.
- [121] W. Yu, A. A. Aczel, T. J. Williams, S. L. Bud'ko, N. Ni, P. C. Canfield, G. M. Luke, *Phys. Rev. B: Condens. Matter Mater. Phys.* **2009**, *79*, 020511.
- [122] A. Kreyssig, M. A. Green, Y. Lee, G. D. Samolyuk, P. Zajdel, J. W. Lynn, S. L. Bud'ko, M. S. Torikachvili, N. Ni, S. Nandi, J. B. Leao, S. J. Poulton, D. N. Argyriou, B. N. Harmon, R. J. McQueeney, P. C. Canfield, A. I. Goldman, *Phys. Rev. B: Condens. Matter Mater. Phys.* **2008**, *78*, 184517.
- [123] C. Huhnt, G. Michels, M. Roepke, W. Schlabit, A. Wurth, D. Johrendt, A. Mewis, *Physica B: Condens. Matter* **1997**, *240*, 26.
- [124] S. A. J. Kimber, A. Kreyssig, Y.-Z. Zhang, H. O. Jeschke, R. Valentí, F. Yokaichiya, E. Colombier, J. Yan, T. C. Hansen, T. Chatterji, R. J. McQueeney, P. C. Canfield, A. I. Goldman, D. N. Argyriou, *Nature Mater.* **2009**, *8*, 471.

-
- [125] C. Krellner, N. Caroca-Canales, A. Jesche, H. Rosner, A. Ormeci, C. Geibel, *Phys. Rev. B: Condens. Matter Mater. Phys.* **2008**, 78, 100504.
- [126] Z.-A. Ren, Q. Tao, S. Jiang, C. Feng, C. Wang, J. Dai, G. Cao, Z. Xu, *Phys. Rev. Lett.* **2009**, 102, 137002.
- [127] A. Mewis, *Z. Naturforsch. B: J. Chem. Sci.* **1980**, 35, 141.
- [128] Z. Wang, H. Yang, C. Ma, H. Tian, H. Shi, J. Lu, L. Zeng, J. Li, *J. Phys.: Condens Matter* **2009**, 21, 495701.
- [129] S. Jiang, H. Xing, G. Xuan, C. Wang, Z. Ren, C. Feng, J. Dai, Z. Xu, G. Cao, *J. Phys.: Condens Matter* **2009**, 21, 382203.
- [130] T. Egami, B. V. Fine, D. Parshall, A. Subedi, D. J. Singh, *Adv. Condens. Matter Phys.* **2010**, 164916.
- [131] M. D. Johannes, I. I. Mazin, D. S. Parker, *arXiv:1004.2160* **2010**.
- [132] M. Rotter, C. Hieke, D. Johrendt, *Phys. Rev. B: Condens. Matter Mater. Phys.* **2010**, 82, 014513.
- [133] R. Mittal, S. K. Mishra, S. L. Chaplot, S. V. Ovsyannikov, E. Greenberg, D. M. Trots, L. Dubrovinsky, Y. Su, Th. Brueckel, S. Matsuishi, H. Hosono, G. Garbarino, *arXiv:1007.2320v2* **2010**.
- [134] I. I. Mazin, D. J. Singh, M. D. Johannes, M. H. Du, *Phys. Rev. Lett.* **2008**, 101, 057003.
- [135] C. C. Tsuei, J. R. Kirtley, *Rev. Mod. Phys.* **2000**, 72, 969.
- [136] J. Bardeen, L. N. Cooper, J. R. Schrieffer, *Phys. Rev. B: Condens. Matter Mater. Phys.* **1957**, 108, 1175.
- [137] W. L. McMillan, J. M. Rowell, *Phys. Rev. Lett.* **1965**, 14, 108.
- [138] J. E. Hoffman, *Science* **2010**, 328, 441.
- [139] L. X. Yang, Y. Zhang, H. W. Ou, J. F. Zhao, D. W. Shen, B. Zhou, J. Wei, F. Chen, M. Xu, C. He, Y. Chen, Z. D. Wang, X. F. Wang, T. Wu, G. Wu, X. H. Chen, M. Arita, K. Shimada, M. Taniguchi, Z. Y. Lu, T. Xiang, D. L. Feng, *Phys. Rev. Lett.* **2009**, 102, 107002.
- [140] C. Liu, G. D. Samolyuk, Y. Lee, N. Ni, T. Kondo, A. F. Santander-Syro, S. L. Bud'ko, J. L. McChesney, E. Rotenberg, T. Valla, A. V. Fedorov, P. C. Canfield, B. N. Harmon, A. Kaminski, *Phys. Rev. Lett.* **2008**, 101, 177005.
- [141] P. Richard, T. Sato, K. Nakayama, S. Souma, T. Takahashi, Y. M. Xu, G. F. Chen, J. L. Luo, N. L. Wang, H. Ding, *Phys. Rev. Lett.* **2009**, 102, 047003.

Bibliography

- [142] L. Wray, D. Qian, D. Hsieh, Y. Xia, L. Li, J. G. Checkelsky, A. Pasupathy, K. K. Gomes, C. V. Parker, A. V. Fedorov, G. F. Chen, J. L. Luo, A. Yazdani, N. P. Ong, N. L. Wang, M. Z. Hasan, *Phys. Rev. B: Condens. Matter Mater. Phys.* **2008**, 78, 184508.
- [143] M. Yi, D. H. Lu, J. G. Analytis, J. H. Chu, S. K. Mo, R. H. He, R. G. Moore, X. J. Zhou, G. F. Chen, J. L. Luo, N. L. Wang, Z. Hussain, D. J. Singh, I. R. Fisher, Z. X. Shen, *Phys. Rev. B: Condens. Matter Mater. Phys.* **2009**, 80, 024515.
- [144] D. J. Singh, *Phys. Rev. B: Condens. Matter Mater. Phys.* **2008**, 78, 094511.
- [145] I. R. Shein, A. L. Ivanovskii, *JETP Lett.* **2008**, 88, 107.
- [146] I. A. Nekrasov, Z. V. Pchelkina, M. V. Sadovskii, *JETP Lett.* **2008**, 88, 144.
- [147] J. H. Shim, K. Haule, G. Kotliar, *Phys. Rev. B: Condens. Matter Mater. Phys.* **2009**, 79, 060501.
- [148] F. Han, X. Zhu, P. Cheng, G. Mu, Y. Jia, L. Fang, Y. Wang, H. Q. Luo, B. Zeng, B. Shen, L. Shan, C. Ren, H.-H. Wen, *Phys. Rev. B: Condens. Matter Mater. Phys.* **2009**, 80, 024506.
- [149] Y. Muraba, S. Matsuishi, S.-W. Kim, T. Atou, O. Fukunaga, H. Hosono, *arXiv:1005.0528v2* **2010**.
- [150] W. Schnelle, A. Leithe-Jasper, R. Gumeniuk, U. Burkhardt, D. Kasinathan, H. Rosner, *Phys. Rev. B: Condens. Matter Mater. Phys.* **2009**, 79, (21), 214516.
- [151] S. Sharma, A. Bharathi, S. Chandra, R. Reddy, S. Paulraj, A. T. Satya, V. S. Sastry, A. Gupta, C. S. Sundar, *Phys. Rev. B: Condens. Matter Mater. Phys.* **2010**, 81, 174512.
- [152] J. Guo, L. Sun, C. Zhang, G. Chen, J. He, X. Dong, W. Yi, Y. Li, X. Li, J. Liu, Z. Jiang, X. Wei, Y. Huang, Q. Wu, X. Dai, Z. Zhao, *arXiv:1008.2086v1* **2010**.
- [153] X. C. Wang, Q. Q. Liu, Y. X. Lv, W. B. Gao, L. X. Yang, R. C. Yu, F. Y. Li, C. Q. Jin, *Solid State Commun.* **2008**, 148, 538.
- [154] G. Hägg, A. L. Kindström, *Z. Phys. Chem. B* **1933**, 22, 453.
- [155] F. C. Hsu, J. Y. Luo, K. W. Yeh, T. K. Chen, T. W. Huang, P. M. Wu, Y. C. Lee, Y. L. Huang, Y. Y. Chu, D. C. Yan, M. K. Wu, *Proc. Natl. Acad. Sci. U.S.A.* **2008**, 105, 14262.
- [156] D. R. Parker, M. J. Pitcher, P. J. Baker, I. Franke, T. Lancaster, S. J. Blundell, S. J. Clarke, *Chem. Commun. (Cambridge, U. K.)* **2009**, 2189.

-
- [157] X. Zhu, F. Han, G. Mu, B. Zeng, P. Cheng, B. Shen, H.-H. Wen, *Phys. Rev. B: Condens. Matter Mater. Phys.* **2009**, 79, 024516.
- [158] M. Tegel, I. Schellenberg, F. Hummel, R. Pöttgen, D. Johrendt, *Z. Naturforsch. B: J. Chem. Sci.* **2009**, 64, 815.
- [159] H. Ogino, Y. Matsumura, Y. Katsura, K. Ushiyama, S. Horii, K. Kishio, J.-J. Shimoyama, *Supercond. Sci. Technol.* **2009**, 22, 075008.
- [160] M. Tegel, F. Hummel, S. Lackner, I. Schellenberg, D. Johrendt, *Z. Anorg. Allg. Chem.* **2009**, 635, 2242.
- [161] S. Nandi, M. G. Kim, A. Kreyssig, R. M. Fernandes, D. K. Pratt, A. Thaler, N. Ni, S. L. Bud'ko, P. C. Canfield, J. Schmalian, R. J. McQueeney, A. I. Goldman, *Phys. Rev. Lett.* **104**, 057006.
- [162] E. Wiesenmayer, *Master's thesis*, Ludwig-Maximilians-Universität, **2010**.
- [163] H. Q. Yuan, J. Singleton, F. F. Balakirev, S. A. Baily, G. F. Chen, J. L. Luo, N. L. Wang, *Nature* **2009**, 457, 565.
- [164] S. Takeda, S. Ueda, T. Yamagishi, S. Agatsuma, S. Takano, A. Mitsuda, M. Naito, *Appl. Phys. Express* **2010**, 3, 093101.
- [165] N. H. Lee, S.-G. Jung, D. H. Kim, W. N. Kang, *Appl. Phys. Lett.* **2010**, 96, 202505.